Investigation of Hollow and Dense Droplet Impact on Solid Surfaces

Mohammad Mahdi Nasiri

A Thesis

in

The Department

of

Mechanical, Industrial, and Aerospace Engineering

Presented in Partial Fulfillment of the Requirements

for the Degree of

Doctor of Philosophy (Mechanical Engineering) at

Concordia University

Montreal, Quebec, Canada

July 2022

CONCORDIA UNIVERSITY

School of Graduate Studies

This is to certify that the thesis prepared,

By: **Mohammad Mahdi Nasiri**

Entitled: **Investigation of Hollow and Dense Droplet Impact on Solid Surfaces**

And submitted in partial fulfillment of the requirements of the degree of

Doctor of Philosophy (Mechanical Engineering)

Complies with the regulations of this University and meets the accepted standards with respect to originality and quality.

Signed by the Final Examining Committee:

Dr. Nabil Esmail	Chair
Dr. Alidad Amirfazli	External Examiner
Dr. Samuel Lee	External to the Program
Dr. Marius Paraschivoiu	Examiner
Dr. Hoi Dick Ng	Examiner
Dr. Ali Dolatabadi	Thesis Supervisor(s)
Dr. Christian Moreau	

Approved by

Martin D. Pugh, Chair
Department of Mechanical, Industrial and Aerospace Engineering

April 12th, 2022
Date of Defense

Mourad Debbabi, Dean
Gina Cody School of Engineering and Computer Science

Abstract

Investigation of Hollow and Dense Droplet Impact on Solid Surfaces

Mohammad Mahdi Nasiri, Ph.D.

Concordia University, 2022.

Droplet impact and its flattening on a surface play an essential role in many industrial applications such as inkjet printing, agriculture, and plasma spraying. Understanding the physics of droplet spreading is the key to maintaining the mass transfer process in all relevant applications. Two different problems are investigated in this study. In the first parts, the behavior of a hollow droplet after impact on a surface is considered, while in the last chapter, the effect of gas desorption on the flattening and solidification of a molten particle in investigated.

Most of the droplets observed in nature are dense droplets. Nevertheless, special droplets have been observed in several industrial applications such as aerosol transfer from the sea, oxygen dissolution, controllable biomedicine, and thermal spray coating which are called hollow droplets. In plasma spraying process, the accumulation of these flatten droplets (splats) on top of each other forms a coated layer. Due to their embedded medium, the cavity-containing droplets (hollow droplets) trigger cavitation when they reach the target and influence the splat properties by releasing the inner substance. However, it is difficult to study the impact and flattening of hollow droplets in thermal spraying, regarding the harsh environments, and phenomena small size and high velocity.

To better understand the flattening process of a hollow droplet, in this work, a comprehensive experimental, numerical, and theoretical study is performed on water and glycerol droplets impacting on a rigid surface. The experiments are repeated on different surfaces, including aluminum, sand-blasted steel, and superhydrophobic. The results show that the mechanisms of the post-impact process of hollow droplets are different from those of dense droplets in several aspects. We study the role of surface wettability, liquid properties, impact velocity, surface angle, and bubble size and location on the droplet flattening process. In the numerical part, compressible Navier-Stokes equations are solved using the volume of fluid (VOF) method. A theoretical model is developed to analyze the maximum spreading diameter of the hollow droplet impact analytically. Its prediction is in good agreement with the experimental and numerical results.

The comparison of simulation results with the experimental photographs shows that the numerical solver can correctly predict the hollow droplet shape evolution. It is demonstrated that flattening a hollow droplet has two significant distinctions compared to a dense droplet flattening. The first distinction is the formation of a counter-jet following the collision of a hollow droplet impact perpendicular to the surface. It is proven that the formation of the counter-jet is an inherent phenomenon of hollow droplet flattening and is unaffected by impact velocity or substrate angle. Nevertheless, it is revealed that the counter-jet length depends on droplet velocity or liquid viscosity. The second distinction is the ultimate shape of the flattened droplet. After contact on a hydrophobic surface, the dense droplet partially recoils toward the center and produces a dome shape. However, upon impact on a hydrophobic surface, the hollow droplet takes the form of a donut. This is owing to the perturbations caused by bubble rupture on the spreading droplet surface. As a result of these perturbations, the spreading liquid sheet is fragmented and, the droplet is unable to recoil toward the center, forming a donut shape. The results show that the spreading diameter and the counter-jet height formed after the hollow droplet impact grows with impact velocity increasing. Investigating the size and location of the entrapped bubble shows an optimum bubble size that facilitates the hollow droplet flattening. It is also demonstrated that the ripples on splats produced by the hollow droplets with a larger bubble size are higher than those of small bubbles.

In the end, the effects of surface gas desorption on the splat formation are studied. In plasma spray, the splats resulting from the impact, spreading, and solidification of molten particles are the building blocks of the spray coatings. Fragmented splats are formed on substrates held at room temperature and atmospheric pressure. Although the formation of a fragmented splat is attributed to adsorbates on the substrate surface, its dynamics have not been adequately addressed. In this study, a numerical model is developed to investigate the formation of fragmented splats during droplet flattening and solidification in plasma spraying conditions. Compressible Navier–Stokes equations are solved, and the volume of fluid (VOF) method is used to capture the liquid and gas interface. In addition, the source term method is used to capture the solidification process during droplet flattening.

Moreover, a new boundary condition is defined to consider the effect of gas desorption on the substrate surface after droplet impact. The numerical results show that gas desorption from the surface produces a barrier layer between the droplet and the substrate. This high-pressure region detaches the edge of the spreading droplet from the surface and forms a liquid sheet. The liquid sheet rises above the substrate and spreads up to 2 times more than droplets

impacting surfaces without gas desorption. The fragmentation of the liquid film follows the overspreading of the droplet. As a result, only a portion of the initial droplet remains at the location of the impact, which forms a small solidified splat.

Acknowledgments

I want to express my sincere gratitude to my supervisors, Prof. Ali Dolatabadi and Prof. Christian Moreau, for their continuous support of my Ph.D. study. Without their motivation, knowledge, insightful comments, encouragement, and challenging questions that triggered several innovative solutions during researching and writing the thesis, this accomplishment would not have occurred.

Some particular words of gratitude go to my friends who have been a significant source of support in this project: Dr. Ghobad Amini and Dr. Hasan Shetabivash.

I am also grateful to my fellow lab-mates for the stimulating discussions and the laughter moments, which decreased the pressure of hard work. I want to thank my friends for expecting nothing less than triumph during my Ph.D. program.

We gratefully acknowledge funding support from the Fonds de recherche du Québec – Nature et technologies (FRQNT), Natural Sciences and Engineering Research Council of Canada (NSERC), and the Canada Research Chair program.

Dedication

To my wonderful family, for their measureless support and unconditional love.

Contribution of the authors

This thesis is prepared in manuscript-based format. Chapters 1 and 6 are the introduction and conclusion of the thesis, respectively. The rest of the chapters are reprinted from published papers or submitted to scientific journals. The first author of all manuscripts is Mr. Nasiri, the author of this thesis and the manuscripts. He has implemented and developed numerical simulations and post-processed the results. He was also responsible for designing, conducting, and post-processing the experimental results. The paper titles, journal names, volume numbers, page numbers, and the contribution of the co-authors will be given in detail as follows.

Chapter 2, entitled “Hollow droplet impact on a solid surface, " is published in the International Journal of Multiphase Flow, Volume 143, pages 103740, 2021 (https://doi.org/10.1016/j.ijmultiphaseflow.2021.103740). This work has been co-authored by Dr. Ghobad Amini, Prof. Christian Moreau, and Prof. Ali Dolatabadi. Dr. Amini helped the first author during the investigation and writing. Prof. Moreau and Prof. Dolatabadi are the supervisors of the project.

Chapter 3, entitled “Spreading and bouncing of a hollow droplet impacting a solid surface” is a submitted paper in the Journal of Fluid Mechanics. This work has been co-authored by Dr. Ghobad Amini, Prof. Christian Moreau, and Prof. Ali Dolatabadi. Dr. Amini helped the first author during the investigation and writing. Prof. Moreau and Prof. Dolatabadi are the supervisors of the project.

Chapter 4, entitled “Experimental and numerical simulation of a hollow droplet impacting a solid surface held at different angles,” is a paper ready to be submitted to the Physics of Fluids journal. This work has been co-authored by Prof. Christian Moreau and Prof. Ali Dolatabadi. Prof. Moreau and Prof. Dolatabadi are the supervisors of the project.

Chapter 5, entitled “Modeling of liquid detachment and fragmentation during the impact of plasma spray particles on a cold substrate” is a paper accepted for publication in the International Journal of Heat and Mass Transfer on February 18, 2022. This work has been co-authored by Prof. Ali Dolatabadi and Prof. Christian Moreau. Prof. Moreau and Prof. Dolatabadi are the supervisors of the project.

Contents

Table of figures

Nomenclature

U_0	Velocity, $(\mathrm{m/s})$.
D_{eq}	Droplet Diameter (m).
D_h	Hollow Droplet Diameter (m).
D_b	Bubble Diameter (m).
D	Diameter (m).
k	Thermal conductivity $(\mathrm{W/m.K})$.
C_p	Specific Heat, $(\mathrm{J/kg.K})$.
P	Pressure, (atm).
T	Temperature, (K).
$\vec{U}$	Velocity vector, $(\mathrm{m/s})$.
t	Time, (s).
V	Volume, $(\mathrm{m^3})$.
KE	Kinetic energy, (J).
SE	Surface energy, (J).
W	Viscosity work.
ϕ	Viscous dissipation function.
$\overrightarrow{S_v}$	Solidification source term of momentum equation.
H	Total Enthalpy.
S_h	Solidification source term of energy equation.
L	Latent heat of fusion,

Latin Symbols

ρ	Density, $(\mathrm{kg/m^3})$.
σ	Surface tension, $(\mathrm{N/m})$.
μ	viscosity, $(\mathrm{kg/m.s})$.

α	The ratio of hollow droplet diameter to dense droplet diameter, ($\frac{D_h}{D_{eq}}$).
β	The ratio of hollow droplet diameter to dense droplet diameter, ($\frac{D_b}{D_{eq}}$).
γ	VOF liquid-gas.
δ	Bubble location ratio.
η	Contact angle.
Ω	The volume of viscous fluid.
θ	VOF liquid-Solid.

Subscriptions

eq	equivalent
b	bubble
h	hollow
cj	Counter-jet
l	liquid
g	gas
s	solid
sp	spreading

1 Chapter One: Introduction

Since Worthington's studies in 1877 [1], the effective parameters during droplet impact have been studied intensively through experimental [2-7], analytical [8-10], and numerical modeling [11-13] investigations. There are many applications for droplet impact and solidification on solid surfaces in various industries, including power generation, ink-jet printing, aerospace, and thermal spraying [14]. Depending on the application, different parameters can affect the droplet flattening after the impact on a surface.

1.1 Thermal spraying

Thermal spraying is a process that produces coated layers with a thickness that ranges from tens of micrometers to several millimeters. Thermal barrier coating (TBC) is one of the thermal spraying products in which a plasma torch melts the micrometer-sized particles and sprays them toward a substrate at high velocities [15]. During this process, molten particles spread on the substrate surface, solidify, and produce layers with a thickness of several micrometers (Figure 1-1). These layers resist corrosion, wear, oxidation, and heat transfer.

Different types of materials can be used as the feedstock for TBC regarding its applications. Generally, feedstock powders of TBC are in the shape of dense particles or hollow particles. Dense particles are the prevalent powder type in plasma spraying due to their simple production. Nevertheless, dense particles are not always the best option since they can be semi-molten when passing through the plasma jet [16]. TBC feedstock powders usually have low thermal conductivity. Therefore, some of them are not melted entirely and remain semi-molten during passing through the plasma. Hollow particles are a solution to this problem.

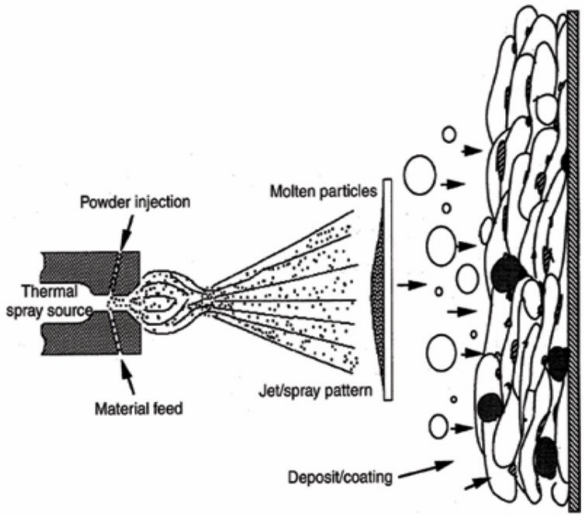

Figure 1-1. Schematic of the plasma spraying process and layers buildup [17].

Hollow particles (Figure 1-2), first produced by Longo et al. [18], are widely used in TBC. Using hollow particles favorites complete melting of their shell in the plasma jet [19]. Improved characteristics of the generated coatings have been proven in several studies [20-22]. Moreover, using these particles can increase coating porosity producing materials with different thermal resistances and enhanced thermal insulation properties [21].

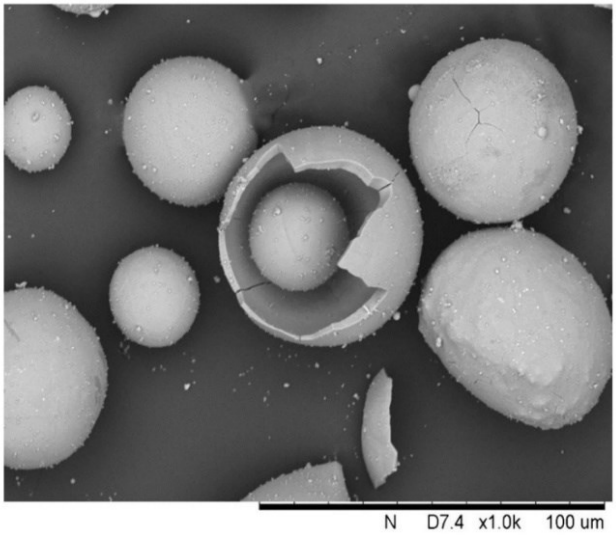

Figure 1-2. SEM image of hollow sphere ZrO_2 $8Y_2O_3$ powder (Oerlikon Metco 204 NS) [17].

Coating quality depends on the droplet impact process, during which the droplet is flattened and solidified on a substrate. Since such a process occurs in only a few microseconds [23], it is difficult to capture molten particle flattening after impact on a substrate in plasma spraying, regarding the harsh environments, and phenomena small size and high velocity. Therefore, analytical calculations and numerical simulations are used to bring more information about the process. However, in order to use numerical simulation results for the droplet flattening, the numerical code has to be validated with the experimental data. As a result, some experiments should be done to study the droplet flattening in conditions which are easier to handle than thermal spraying conditions. Even though the main objective of this study is to investigated the behavior of a hollow droplet after impact on a surface, nevertheless, it is essential to investigate the flattening of a dense droplet because most of the phenomena that occur for dense droplets, such as splashing [24], can happen for hollow droplets. Hence, knowing the behavior of a dense droplet after impact on a surface also provides valuable information about hollow droplet impact.

1.2 Dense droplet Impact

Droplet impact has been a topic of interest for a long time due to its countless applications, such as inkjet technology [25], fuel injection, spray coating, and cooling systems [26]. Different scenarios may occur when a droplet impinges the surface, as shown in Figure 1-3 [26]. These other behaviors mainly depend on the liquid and surface properties and their initial conditions, such as droplet size and impact velocity.

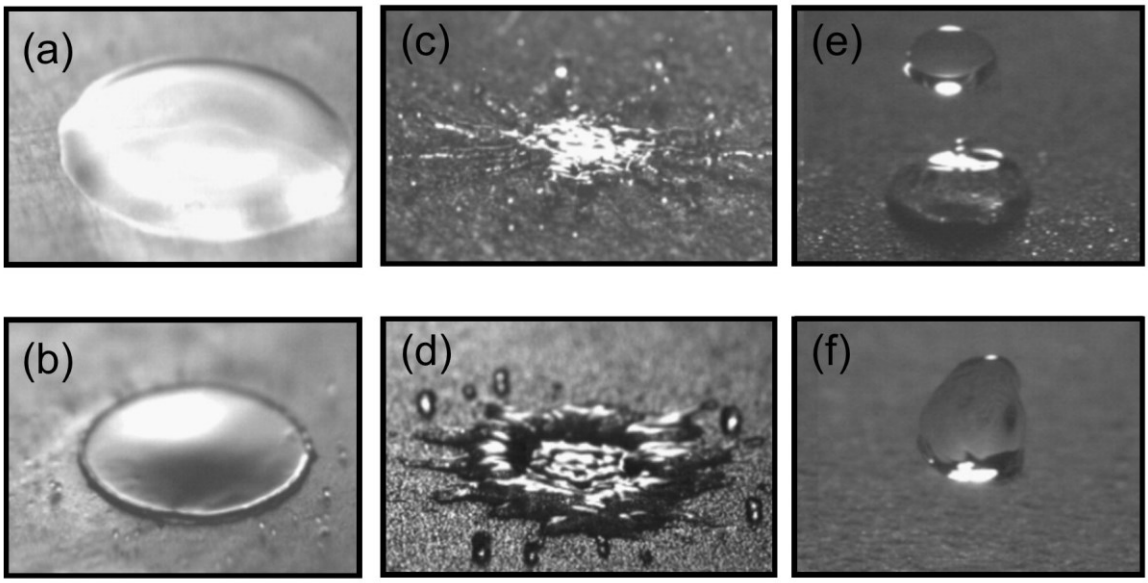

Figure 1-3. Dense droplet impact outcome on a solid surface.
(a) deposition, (b) corona plash, (c) prompt splash, (d) receding break-up, (e) partial rebound, (f) complete rebound [26].

In the deposition, dense droplet spreads and remains on a solid surface without any breakup, which mostly happens when the surface has no asperities that might affect the deposition process. In the corona splash, small droplets generate around the rim after droplet collision, mainly when the droplet impacts with high velocity on a smooth surface. When the droplet impact velocity is high and the surface has a roughness, prompt splash might occur, generating many small droplets. The receding breakup occurs when the receding contact angle decreases while the liquid retracts from the maximum spreading. Thus, some small droplets are left behind during the receding stage. Partial and complete rebound is mainly attributed to the impact on a superhydrophobic substrate due to surface roughness patterns, which results in air entrapment and exhibits high contact angles. If the droplet impact velocity reaches a high value, the air traps might collapse, and the droplet can penetrate within the asperities, and partial rebound can occur.

Dimensionless numbers such as, $We = \frac{\rho\, D\, U^2}{\sigma}$, $Re = \frac{\rho\, U\, D}{\mu}$, $Oh = \frac{\mu}{\sqrt{D\rho\sigma}}$, and $Ca = \frac{\mu\, U}{\sigma}$ are usually employed to address the dense droplet impact and spreading dynamics. These are Weber, Reynolds, Ohnesorge, and Capillary numbers, respectively [27]. The parameters ρ,D,U,σ and μ represent the droplet density, diameter, velocity, surface tension and viscosity, respectively.

Additionally, Peclet number ($Pe = \frac{\rho\, D\, U\, C_p}{k}$) and Stefan number ($Ste = \frac{C_p(T_m - T)}{L}$) have been found to be essential in determining droplet solidification [27], where C_p, k, and T_m and L are specific heat, thermal conductivity, melting temperature and latent heat, respectively.

As discussed in the next section, there are many studies in the literature on dense droplets' impact onto a surface. In these researches, different aspects of the impact process such as splats shapes [23, 28], droplet solidification [23, 29], and droplet spreading on a surface are studied [30, 31]. Nevertheless, only limited studies are dedicated to hollow droplet impact on a surface that needs more investigation.

1.3 Hollow droplet impact

The majority of research on droplet impingement assumes that the droplet is dense and has a spherical shape. However, there are many natural phenomena and industrial applications in which droplets contain a bubble inside, i.e., hollow droplets. For instance, hollow droplets exist in aerosol transfer from the sea [32], raindrops reaching earth [33], oxygen dissolution in lakes, foams, spray painting and coating, ink jet printing [4], bubble bursting [34, 35], catalytic processes, microfabrication, bioprinting, cooling processes [36], etc. When these hollow droplets impinge on a solid surface, understanding the solid-liquid-gas interactions is crucial in applications such as controllable biomedicine [37], spray coatings [19, 23, 38], the printing of foam materials [39], and sonoporation [40]. Specifically, for biological precision medicine, the droplets commonly serve as supports to transport a gene or drug in which reaching the required target, cavitation is triggered to release the inner substance [41-43], and in plasma spray coatings, in order to produce functional coatings, heterogeneous hollow droplets embedded with a cavity are used to control the porosity and thermal properties [44]. For instance, it has been reported that the coating produced with yttria-stabilized zirconia hollow sphere particles has lower thermal conductivity compared to coating produced with dense

yttria-stabilized zirconia powders [38]. Nevertheless, the reason behind the difference in the quality of coatings produced by hollow droplets is not fully understood.

Although there are many studies on the behavior of dense droplets during the droplet impact on a surface [23, 28-31, 45, 46], information about hollow droplets is scarce, and there are few publications about this type of droplets. Solonenko et al. [19] studied the behavior of yttria-stabilized zirconia (YSZ) hollow droplets. Imaging the impact of a micrometer-sized hollow droplet on a surface showed that droplets are explosively splashed. In another research [21], they showed that shapes of splats are discontinuous at high impact velocities. They studied different scenarios for the droplet post-impact qualitatively. To the best of the authors' knowledge, the only experimental study on hollow droplet flattening is performed by Gulyaev et al. using glycerol droplets [47]. Gulyaev et al. [47, 48] identified the formation of a counter jet during the impact of a millimeter-sized hollow glycerin droplet on a surface.

Kumar et al. introduced a numerical model capable of simulating the impact of a hollow droplet and its solidification [49]. This model was used for low impact velocities. In their subsequent studies [50, 51], they investigated ZrO_2 droplet impact on a surface under actual thermal spray conditions. In these studies, they assumed that the fluid was incompressible. However, due to the high impact velocity, the compressibility of the trapped gas may become highly important [17]. Safaei et al. [17] used the model of Kumar et al. [49-51] and added the effect of the compressibility of gas to their simulation. In addition, the effect of trapped gas and the internal recirculation thereof on the dynamic behavior of a hollow droplet was investigated. The other studies of hollow droplet flattening have focused on the numerical simulation of this phenomenon [52-54]. They have studied counter-jet formation, heat transfer rate, maximum spreading diameter prediction, and multiple hollow droplets impact. Nevertheless, the results of simulations for micrometer-sized droplets could not be validated due to the lack of experimental data.

1.4 Splat fragmentation

In prevalent plasma thermal spray conditions, the droplet spreads smoothly on the substrate and forms a uniform solidified layer (disk splat; Figure 1-4.a). The accumulation of these solidified layers on top of each other produces a coated layer. However, there are conditions in which the droplet disintegrates after impact on the substrate and only a small core solidifies. This small central core is surrounded by debris (Fragmented splat; Figure 1-4.b). The

characteristics of the final coated layer are different in the last case, and the rate of feedstock waste is higher compared to prevalent cases. It is thus necessary to study the parameters that may lead to these conditions.

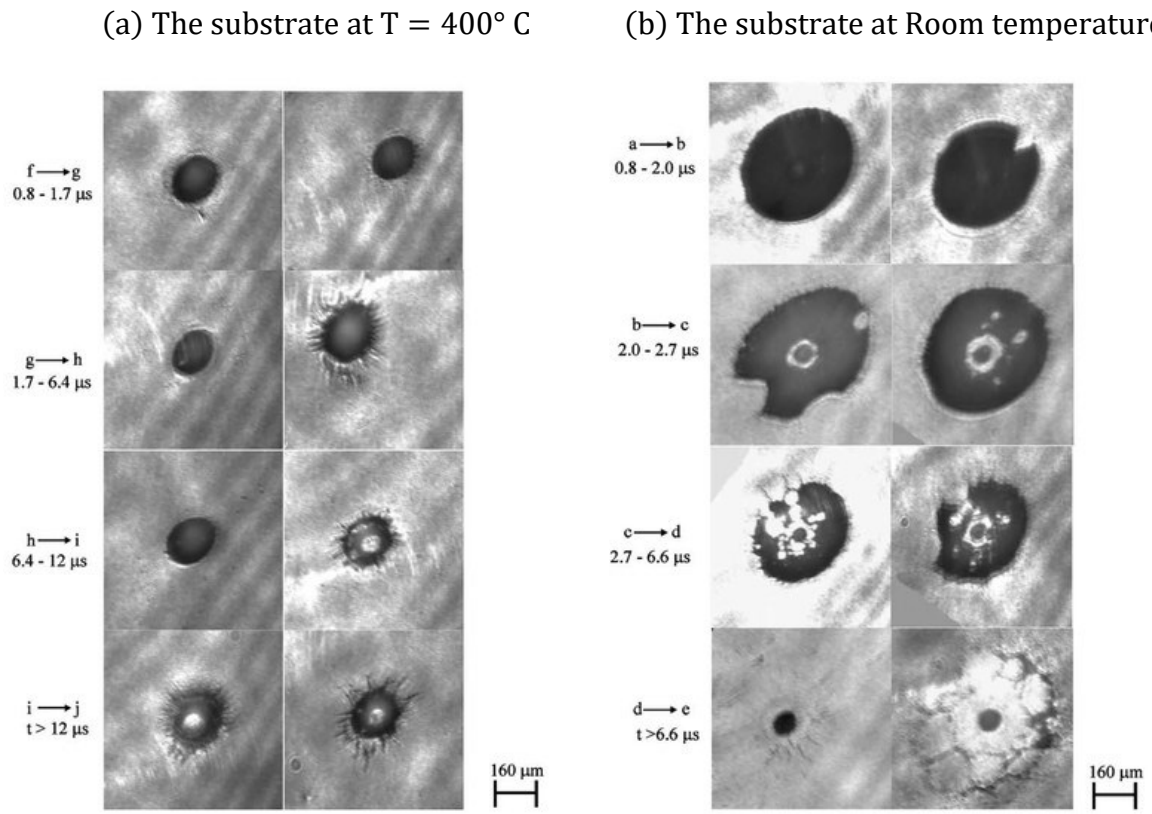

Figure 1-4. Over-spreading and solidified core of droplets on the substrate at different temperatures. (a) substrate at 400° C, (b) substrate at room temperature [23].

Experimental investigations have indicated four variations between “disk splats” and “fragmented splats” characteristics. In general, fragmented splats have smaller solidified cores surrounded by lots of debris [23, 28, 55-61] (Figure 1-4). The droplet spreads up to three times wider in “fragmented splats” cases before it solidifies compared to other cases (Figure 1-4)[23]. The solidified core of the “fragmented splat” contains more grains [28, 57] and, it doesn’t contain waves on the surface edge of its solidified core [57]. While the “fragmented splat” is an unusual case in plasma thermal spray, it has been reported that this splat becomes the dominant type of splat at specific substrate temperatures and ambient pressures [23, 28, 55-61]. The effects of these special conditions are discussed in the following sections.

1.4.1 Effects of the substrate temperature

Most droplet splats are “fragmented splats" on the substrates held at room temperature. The ratio of “fragmented splats” to “disk splats” decreases with substrate temperature increment,

and at a specific temperature, “disk splats” become the majority on the substrate [23, 28, 55-61] (Figure 1-5.a). A specific substrate temperature has been defined as the “transition temperature” (T_t) [55, 62], and at higher temperatures, “disk splats” dominate, while at lower temperatures, “fragmented splats” are more common (Figure 1-5.a).

Many experiments have been performed to study the effects of substrate temperature by examining the parameters related to the substrate temperature, which include the droplet-surface contact angle [55], substrate roughness [28, 60, 63-66], and thermal contact resistance [23, 59, 61, 67, 68]. Bonding mechanisms can justify the effects of these parameters on the formation of “disk splats”. Three different bonding mechanisms were reported in the thermally sprayed coating, namely, chemical, physical, and mechanical bonding. Since there is no significant diffusion or chemical reaction on the interface of the coating and the substrate at different temperatures, mechanical bonding is the primary bonding mechanism [64]. More intimate contact and improved wetting on the hot substrate have been suggested to improve mechanical bonding; hence, the adhesion strength of the coating on the hot substrate is enhanced and leads to the formation of disk splats [61, 64].

1.4.2 Effect of ambient pressure

The other condition that affects the formation of fragmented splats is ambient pressure. Yang et al. [55] observed that only around 10% of the splats deposited at atmospheric pressure at room temperature are “disk splats”. The splat shape on the flat substrate tends to change from a “fragmented splat” to a “disk splat” with decreasing the ambient pressure [55], and other researchers have confirmed this behavior for different substrates and feedstock [56, 69]. Nevertheless, it has been reported that the influence of substrate temperature on the cooling rate, splat porosity, and adhesion strength appears much stronger than the effect of ambient pressure [61].

Figure 1-5.b shows the fraction change of the disk splat on the substrate surface as ambient pressure changes, showing the tendency of droplet splats to change at different ambient pressures. Similar to substrate temperature, a transition pressure has been defined (P_t) that describes a critical pressure at which the fraction of “disk splats” exceeds 50% with reducing ambient pressure [55].

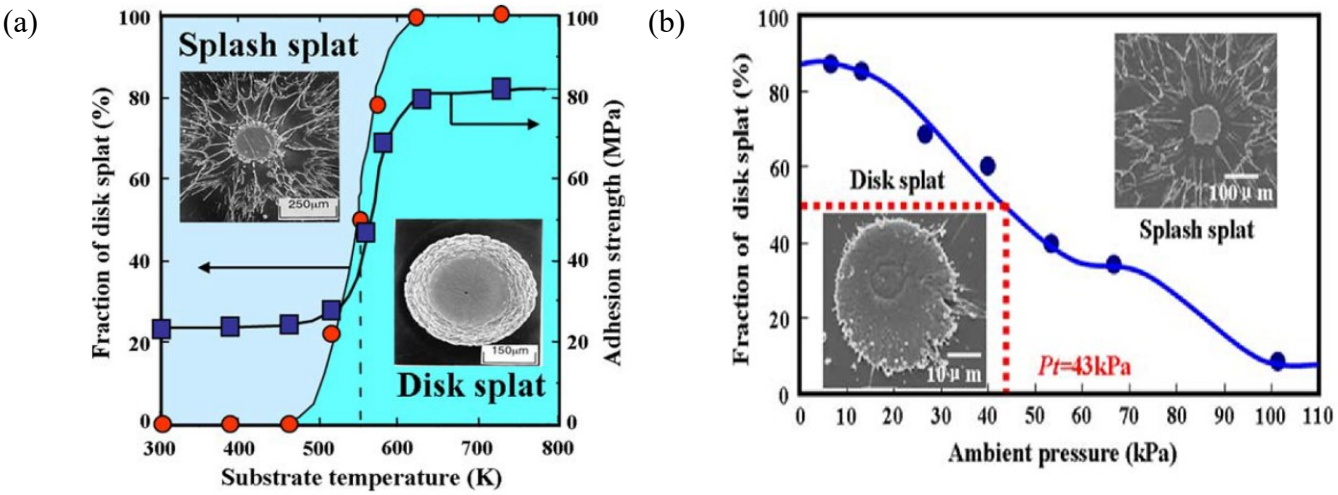

Figure 1-5. Fraction change of disk splat with substrate temperature and ambient pressure reduction [55].
(a) Fraction change of disk splat with substrate temperature, (b) Fraction change of disk splat with ambient pressure.

Fukumoto et al. proposed a temperature-pressure transient table to predict droplet fragmentation [56]. Based on their research, "fragmented splats" are more frequent than "disk splats" when the substrate temperature is lower than the "transient temperature" and when ambient pressure is higher than "transient pressure". This fraction decreases with higher substrate temperature and lower ambient pressure.

Even though the effect of substrate temperature and ambient pressure on "fragmented splat" is evident, the factors causing this phenomenon are not fully understood. Li et al. [70] performed a study on substrate surface adsorbents. They noted that water is the main component at the surface. Although substrate temperature and ambient pressure influence on the formation of the fragmented splats is well established, the reasons behind this phenomenon are not fully understood. Li et al. [70] studied the substrate surface adsorbents; they noted that water is the main component at the surface. This water is adsorbed in several monolayers of the substrate surface and can have a thickness between 2 and 10 nm [65]. It has been proposed that the desorption of the water from the surface in the form of water vapor during droplet impact prevents the droplet from establishing good contact with the surface. This desorbed gas makes an isolation layer between the spreading liquid and the substrate surface, leading to overspreading of the droplet and the formation of the fragmented splat. In addition, this isolation layer increases thermal resistance between the droplet and the substrate [23, 28, 55-61, 63-66]. Furthermore, there is poor contact between the fragmented splat and substrate surface held at room temperature [28, 57].

1.5 Numerical simulation of droplet impact and solidification

Generally, Navier-stokes equations, including mass, momentum, and energy, are the governing equations to simulate droplet flattening.

The conservation of mass equation is as follows;

$$\frac{\partial \rho}{\partial t} + \vec{\nabla}.(\rho \vec{U}) = 0 \tag{1-1}$$

where ρ and $\vec{U}$ are mixture density and velocity field [71].

The momentum equation is as follows [40];

$$\frac{\partial(\rho \vec{U})}{\partial t} + \nabla.(\rho \vec{U}\vec{U}) = -\vec{\nabla}p + \rho\vec{g} + \vec{\nabla}.\left\{\mu\left[\nabla\vec{U} + (\nabla\vec{U})^T\right]\right\} + \overrightarrow{F_{Vol}} - \overrightarrow{S_v} \tag{1-2}$$

where p is pressure, $\vec{g}$ is gravity, and $\overrightarrow{S_v}$ is the solidification source term. Surface tension is considered as a source term ($\overrightarrow{F_{Vol}}$) and can be calculated using the Brackbill method [72].

To solve momentum equations properly, the pressure equation must be calculated. The pressure field can be calculated from the following equation [71];

$$\left(\gamma\frac{\Psi_l}{\rho_l} + (1-\gamma)\frac{\Psi_g}{\rho_g}\right)\left[\frac{\partial p}{\partial t} + \vec{U}.\vec{\nabla}p\right] + \vec{\nabla}.\vec{U} = 0 \tag{1-3}$$

where Ψ_l, Ψ_g, ρ_l, and ρ_g are the liquid compressibility, the gas compressibility, and the liquid and gas density, respectively.

To model heat transfer and solidification effects, it is necessary to solve the energy equation. Neglecting viscous dissipation effects, the energy equation for compressible flow has been derived as follows [73];

$$\frac{\partial(\rho H)}{\partial t} + \vec{\nabla}.(\rho \vec{U}H) = \nabla.(k_{eff}\nabla T) + \frac{\partial p}{\partial t} - \left(\frac{\partial \rho K_E}{\partial t} + \vec{\nabla}.(\rho \vec{U}K_E)\right) \tag{1-4}$$

where K_E and H are the kinetic energy of fluid and the total enthalpy, respectively.

1.5.1 The volume of fluid equation

To track the interface of two fluids, the VOF equation for compressible flow must be used [71];

$$\frac{\partial(\gamma)}{\partial t} + \vec{\nabla}.(\gamma \vec{U}) = \frac{-\gamma\,\Psi_l}{\rho_l}\frac{Dp}{Dt} = \gamma(1-\gamma)\zeta + \gamma\vec{\nabla}.(\vec{U}), \tag{1-5}$$

$$\zeta = \left(\frac{\Psi_l}{\rho_l} + \frac{\Psi_g}{\rho_g}\right)\frac{Dp}{Dt}$$

By solving the above equation, the value of α can be obtained for each computational cell. A unity value of α indicates that the cell is occupied by the liquid, whereas a value of $\alpha = 0$ represents a cell occupied by the gas. Any value between $0 < \alpha < 1$ indicates that the cell contains a liquid-gas interface (Figure 1-6).

Once α has been determined, the surface tension force can be calculated as follows [72];

$$\overrightarrow{F_{Vol}} = \sigma\kappa(\nabla\gamma), \qquad \kappa = -\nabla.\left(\frac{\nabla\gamma}{|\nabla\gamma|}\right) \tag{1-6}$$

where σ and κ represent the surface tension of the liquid and the surface curvature, respectively. $\nabla\alpha$ is a continuous function that is zero everywhere in the domain except for the transitional area at the interface.

1.5.2 Solving energy equation in the presence of solidification

Apparent capacity [74], effective capacity [75], and source-based methods [76] are the methods that treat the solidification interface and are being explained in the next section.

1.5.2.1 Apparent capacity method

In this method, capacity has been defined to include the latent heat of fusion;

$$C_{app} = \frac{\int_{T_{ref}}^{T} C(T)dT + L}{T_l - T_s}, \tag{1-7}$$

$$H = C_{app}T$$

T_s, T_l, and $C(T)$ indicate solid temperature, liquid temperature, and specific capacity as a function of temperature, respectively. The apparent capacity is defined in the range of phase change temperatures to consider the latent heat at the liquid-solid interface [74]. Apparent specific heat can be calculated either explicitly or implicitly. The apparent capacity is calculated from the temperature at the previous time step in the explicit scheme. While the capacity is evaluated from the current temperature field using an implicit scheme. Despite the simplicity, this method has a problem dealing with nodes for which temperature falls from above the liquid temperature to below the solidus temperature. As a result, the heat of fusion would not be accounted for in those cells.

1.5.2.2 Effective capacity method

This method is an extension of the apparent capacity method, which can be evaluated by integrating apparent capacity over the control volume [75].

$$C_{eff} = \frac{\int C_{app}\, dV}{V} \tag{1-8}$$

C_{eff} is the effective capacity and V is the control volume. For the cases with steep temperature gradients at the interface (similar to solidification cases), this method is expensive because higher sampling frequencies are required during the numerical integration [75].

1.5.2.3 Source-based method

In this method, the enthalpy has been expressed as a function of temperature [76];

$$H = h + \Delta H,\ h = h_{ref} + \int_{T_{ref}}^{T} C_p dT. \tag{1-9}$$

Inserting H from Equation (1-9) into Equation (1-4) results in the following.

$$\frac{\partial\left(\rho C_{p\,eff} T\right)}{\partial t} + \vec{\nabla}.\left(\rho\, \vec{U} C_{p\,eff} T\right) = \nabla.\left(k_{eff} \nabla T\right) + \frac{\partial p}{\partial t} - \left(\frac{\partial \rho K_E}{\partial t} + \vec{\nabla}.\left(\rho\, \vec{U} K_E\right)\right) + S_h \tag{1-10}$$

$$S_h = \left(\frac{\partial(\rho \Delta H)}{\partial t} + \nabla.\left(\rho \vec{U} \Delta H\right)\right)$$

where S_h, $C_{p\,eff}$, and k_{eff} are the solidification source term, the specific heat capacity, and the conduction heat transfer coefficient of the mixture, respectively.

To calculate the source term, latent heat should be represented as a function of temperature. Two approaches can be used to express latent enthalpy as a function of temperature. In the first approach, the latent enthalpy is defined directly as a function of temperature [76];

$$\Delta H = \begin{cases} 0, & T < T_s \\ \frac{L}{2\delta}\left(T - \frac{(T_l + T_s)}{2} + \delta\right), & T_s < T < T_l \\ L, & T \geq T_l \end{cases} \tag{1-11}$$

where L is the latent heat of fusion and $\delta = \frac{(T_l - T_s)}{2}$ is a temperature half range over which the phase change occurs. Using this function, the source term in Equation (1-10) can be calculated implicitly or explicitly. The drawback of this method is the difficulty of calculating the solid

fraction from the calculated enthalpy of the domain. Another approach, which is easier to implement, is to express the enthalpy of fusion in terms of the solid fraction.

Assuming phase change and the existence of a mushy zone, latent enthalpy can be considered to be a function of temperature ($\Delta H = f(T)$). Voller et al. [76] assumed that in the mushy zone, the latent heat of fusion (ΔH) is a fraction of the total latent heat of fusion (L);

$$\Delta H = \theta L \tag{1-12}$$

where θ is the liquid fraction inside the droplet. Voller et al. [76] considered θ to be a linear function of temperature. Rosler [77] suggested the following formula for function θ;

$$\theta = 0.5 erf\left(\frac{4(T - T_m)}{(T_l - T_s)}\right) + 0.5 \tag{1-13}$$

T_l is the liquidus temperature, T_s is the solidus temperature, and T_m is the average of T_l and T_s ($T_m = {}^{(T_s + T_l)}/_{2}$). Now, the liquid fraction inside the droplet becomes as follows;

$$\frac{\partial \theta}{\partial t} = \frac{4\left(e^{-\left(\frac{4(T-T_m)}{(T_l-T_s)}\right)^2}\right)}{(T_l - T_s)\sqrt{\pi}} \frac{\partial T}{\partial t} \tag{1-14}$$

Finally, the energy source term has been calculated;

$$S_h = -\rho L \frac{4\left(e^{-\left(\frac{4(T-T_m)}{(T_l-T_s)}\right)^2}\right)}{(T_l - T_s)\sqrt{\pi}} . \left(\frac{\partial T}{\partial t} + \vec{U}.\vec{\nabla} T\right) \tag{1-15}$$

Rosler's suggested technique is suitable for one domain formulation. The advantage of this technique is that it is always possible to transfer the S_h term to the right side of Equation (1-10) and implicitly calculate the temperature.

1.5.3 Solving momentum equation in the presence of solidification

Due to the phase change and solidification phenomena, the momentum equation should be modified such that at the end of solidification, the velocity of the frozen liquid becomes close to zero. Different methods to treat the solidification front are discussed in this section.

1.5.3.1 Fixed velocity and modified fixed velocity

The fixed velocity approach treats solidified computational cells as solid by imposing zero velocity [78]. This method assumes that the solidified material in a cell behaves like a wall.

The most important drawback of this approach is the fact that cells are divided only into solid or non-solid cells without accounting for the transitional region, where liquid-solid volume fraction is between one and zero.

Pasandideh-Fard et al. [46] presented a modified fixed velocity approach for treating the liquid-solid interface by considering the transitional region. To represent the liquid part of the droplet, they defined an indicator function with the value of one within the liquid and zeroed in solid.

$$\theta = \begin{cases} 1 & liquid \\ 0 < \theta < 1 & interface \\ 0 & solid \end{cases} \tag{1-16}$$

For areas in the domain occupied entirely by air and fluid, the value of θ is set to one. θ takes the zero value in any cell occupied by solid, and a value between zero and one in any cell situated at the liquid-solid interface (Figure 1-6).

This approach has been used extensively to simulate the solidification of a molten droplet in the plasma spray process. For instance, Pasandideh-Fard et al. [46] used this approach to three-dimensionally simulate a droplet on stainless steel in the presence of solidification. In addition, Liu et al. [79] employed this method to simulate the impact and freezing of droplets in the plasma spray process. This method is also used by Raessi et al. [80] to simulate water droplet impact and freezing on solid surfaces. In this approach, the presence of air is avoided by setting cells containing air as void, which may cause some inaccuracies in cases in which the presence of air is essential.

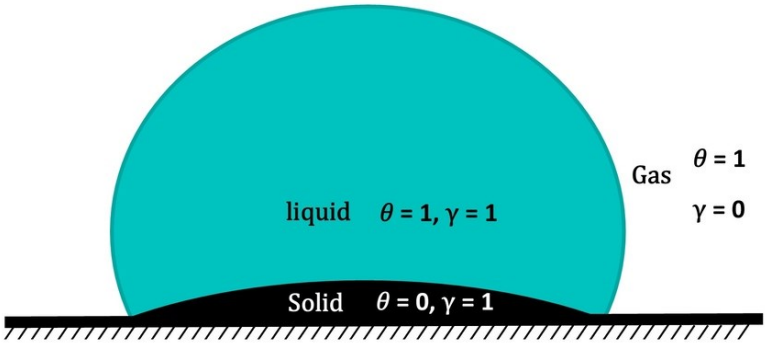

Figure 1-6. Schematic of a molten particle while freezing

1.5.3.2 Increased viscosity method

This approach considers enormous values for viscosity in the solid region so that the velocity in this region approaches zero [76]. In this method, a model has required to couple the liquid

viscosity to the solid fraction, which increases to a huge value in cells occupied by a solid. Several functions with this characteristic can be used to express the variation of viscosity within the liquid-solid interface. A relation inspired by the Carman-Koseny equation and used by Alavi and Passandideh-Fard must be written in the following form [81];

$$\mu = \left[1 + \frac{C\,(1-\theta)^2}{(\theta^3 + \varepsilon)}\right] \mu_l \tag{1-17}$$

μ_l is liquid viscosity, C is a large constant, and ε is a small number to avoid division by zero. Despite the simplicity of implementation, this method lacks information about the viscosity variation near the freezing point.

1.5.3.3 D'Arcy source term

The D'Arcy source method, used by Voller et al. [82], is a common approach to simulate the process of solidification. The main assumption of this method is that the mushy zone at the liquid-solid interface behaves as a porous medium. To accomplish this, a source term ($\overrightarrow{S_v}$) is added to the momentum equation (1-2) [76].

$$\overrightarrow{S_v} = -A\,\vec{U}, \qquad A = \frac{-C\,(1-\theta)^2}{(\theta^3 + \varepsilon)} \tag{1-18}$$

where A is a variable that increases from zero to a significant value, as the local solid fraction, C, is a large constant (that depends on the morphology of the porous medium) and e is a small number used to avoid division by zero during the computational process.

In the current formulation, the mean properties of phases must be used rather than studying each phase individually. To this end, k_{eff}, $C_{p\,eff}$ and μ have been calculated as follows. It should be noted that the droplet (indexed) consists of liquid and solid phases.

$$\begin{gathered} k_{eff} = \gamma\, k_d + (1-\gamma) k_g, \quad k_d = \theta\, k_l + (1-\theta) k_S \\ C_{p\,eff} = \gamma\, C_{pd} + (1-\gamma) C_{pg}, \quad C_{pd} = \theta\, C_{pl} + (1-\theta) C_{ps} \\ \mu = \gamma\, \mu_d + (1-\gamma)\mu_g \end{gathered} \tag{1-19}$$

Moreover, the mixture density is also defined as Follows;

$$\rho = \gamma\, \rho_d + (1-\gamma)\rho_g, \qquad \rho_d = \theta\, \rho_l + (1-\theta)\rho_S \tag{1-20}$$

1.6 Research Objectives

The solidified droplet after impact, forming lamellae, is the building block of the structure of a coating developed by plasma spray. Coating structure and properties can be manipulated by any changes in the droplet characteristics such as droplet type, size, temperature, velocity, etc. For instance, instead of dense particles, hollow particles of the same material are vastly being used as feedstock in TBC processes because their final product is more porous and has lower thermal conductivity. Hence, it is important to know the effects of these parameters on droplet behavior after impact on a surface and during solidification, which is the motivation to perform this research study.

The main **objective** of the current study is a comprehensive investigation of a hollow droplet impact and solidification in plasma spraying conditions. To do so, a combination of numerical and experimental investigations is needed. The following tasks are considered to achieve this objective

1. Numerical simulation of a two-phase flow that can predict the outcome of a droplet impact with regard to fluid compressibility.
2. Experimental study of millimeter-sized hollow droplet impacts on a surface and detailed analysis of the numerical study of hollow droplet dynamics after impact on a surface.
3. Develop a three-phase model that can predict a hollow droplet flattening and solidification.
4. Develop a three-phase model that can predict splat fragmentation at thermal spraying conditions.

The main goal of this study is to provide a better insight into the flattening and solidification process of hollow and dense droplets after impact on a surface in plasma spraying conditions.

1.7 Outline of thesis

This thesis is organized in a paper-based format which presents a fundamental study on the physics underlying a hollow droplet impact on a surface. The intrinsic behavior of a hollow droplet is investigated through experimental and numerical studies. In addition, a numerical code is developed to simulate droplet flattening and solidification at thermal spraying conditions.

Chapter 1 introduces droplet impact and solidification as the base for the thermal spraying application. Dense and hollow droplets were defined, and studies on flattening of these droplets after impact on a surface were reviewed. In addition, the “splat fragmentation” phenomenon, which occurs at special conditions in thermal spraying, was explained.

Chapter 2 presents an experimental and numerical study on the impact of dense and hollow droplets (at low Weber numbers) on surfaces with different wettability. Water and glycerol were used as the droplet material, and experiments were repeated on various surfaces, including aluminum, superhydrophobic and grid-blast surfaces. A three-phase numerical model has been implemented, which was validated with the experimental data. The numerical simulation has captured the hollow droplet movement in the air, the bubble collapse during the hollow droplet flattening, and the formation of the counter-jet as the intrinsic phenomenon of a hollow droplet impact.

Chapter 3 presents more details on the hollow droplet flattening on an aluminum surface through experimental and numerical investigations. New parameters are defined to modify the dimensionless numbers that affect a hollow droplet flattening, including Weber and Reynolds numbers. The effects of different parameters, including impact velocity, droplet size, hollowness ratio, bubble location, etc., are investigated. In the end, an analytical solution is developed to predict the maximum spreading diameter of a hollow droplet on a surface.

In Chapter 4, the effect of surface inclination on the flattening of a hollow droplet is studied experimentally and numerically. The top and the side views of a hollow droplet flattening are captured to study the effect of bubble collapse on the flattening of the hollow droplet. It is shown that the bubble rupture induces perturbations on the surface of the spreading liquid, affecting the droplet's final shape during recoil toward the center. In addition, 3D numerical simulations are performed to provide more details about the droplet flatting and the counter jet formation resulting from a hollow droplet impact on a surface.

Chapter 5 presents numerical simulations of the “fragmented splat” formation at thermal spraying conditions. To do so, a compressible numerical code is developed to capture a molten particle flattening and solidification on a surface. The numerical results are validated with previously published experimental data. The adsorption/desorption hypothesis is implemented into the numerical code to simulate “fragmented splat” formation.

Finally, in Chapter 6, a summary of our findings and further recommendations for future research are provided.

2 Chapter Two: Hollow droplet impact on a solid surface

The content of this chapter has been published in the International Journal of Multiphase Flow, in January 2021.

2.1 Introduction

Since Worthington's studies in 1877 [1], the effective parameters during droplet impact have been studied intensively through experimental [2-7], analytical [8-10], and numerical modeling [11-13] investigations. Most research on droplet impingement assumes that the droplet is dense and spherical. However, there are many natural phenomena and industrial applications in which droplets contain a bubble inside, i.e., hollow droplets. For instance, hollow droplets exist in aerosol transfer from the sea [32], raindrops reaching earth [33], oxygen dissolution in lakes, foams, spray painting and coating, ink jet printing [4], bubble bursting [34, 35], catalytic processes, microfabrication, bioprinting, cooling processes [36], etc. When these hollow droplets impinge on a solid surface, understanding the solid-liquid-gas interactions is crucial in applications such as controllable biomedicine [37], spray coatings [19, 23, 38], printing of foam materials [39], and sonoporation [40]. Specifically, for biological precision medicine, the droplets commonly serve as supports to transport a gene or drug in which reaching the required target, cavitation is triggered to release the inner substance [41-43], and in plasma spray coatings, in order to produce functional coatings, heterogeneous hollow droplets embedded with a cavity are used to control the porosity and thermal properties [44]. For instance, it has been reported that the coating produced with yttria-stabilized zirconia hollow sphere particles has lower thermal conductivity compared to a coating made with dense yttria-stabilized zirconia powders [38]. Nevertheless, the reason behind the difference in the quality of coatings produced by hollow droplets is not fully understood.

Although there are many studies on the dense droplet impingement, only a few studies have concentrated on the dynamics of hollow droplets during falling [83] and impact on a surface, for instance, Kumar and Gu [49], Safaei et al. [17], and Li et al. [84]. Even though Zhu et al. investigated the production of hollow droplets with low viscosity liquids [85], to the best of the authors' knowledge, the only experimental study on the hollow droplet flattening is the one performed by Gulyaev et al. using glycerol droplets [47]. The current work aims to understand the dynamics of hollow droplet impact by performing a combined experimental and numerical study on water and glycerol droplets impacting surfaces with various wettability. The experiments are performed with dense and hollow water droplets and the results are compared to visualize the behavior of hollow droplet after impact on the surface. The experiments were repeated on three different types of surfaces including aluminum, sand-blasted steel (SBS) and superhydrophobic to demonstrate the role of surface wettability. In parallel, a compressible multiphase Volume of Fluid solver is utilized to describe the underlying physics governing the

origin of bubble bursting and counter jet formation. The hollow droplet spreading, formation and evolution of the counter jet, and the effects of droplet velocity and viscosity on these parameters are investigated.

2.2 Governing equations and numerical methods

Figure 3-3 shows the geometry model of a droplet impact on a flat surface. These geometrical parameters defined in the figure are related to each other by the definition of A, B parameters which are,

$$D_{eq} = D_d\ , \quad \alpha = D_h/D_{eq}\ , \quad \beta = D_b/D_{eq}\ , \quad \alpha^3 - \beta^3 = 1 \tag{2-1}$$

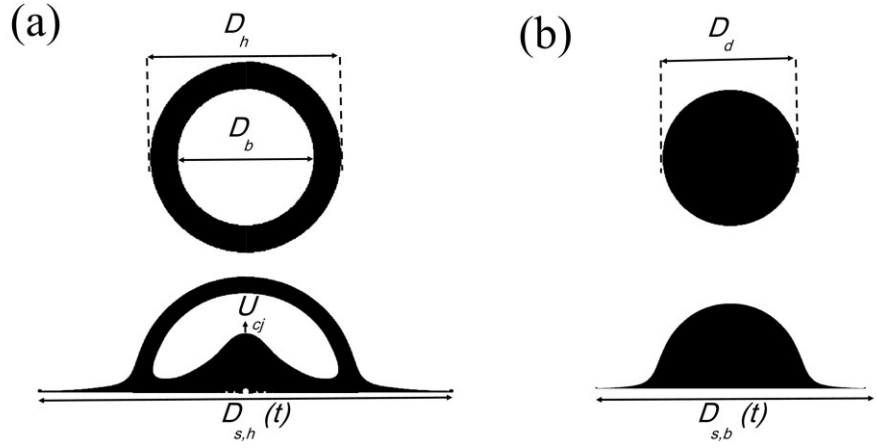

Figure 2-1. The geometry model of a droplet impacting on a flat surface.
(a) hollow droplet, (b) dense droplet. The following geometrical parameters are defined to characterize the impact process: the initial diameter of the hollow droplet (D_h), the initial diameter of bubble inside hollow droplet (D_b), the initial diameter of the dense droplet (D_d) and equivalent diameter of the droplet with the same mass (D_{eq}). A hollow droplet ($D_h = 5.6$ mm, $D_b = 4.5$ mm) and a dense droplet with the same mass ($D_d = 4.4$ mm) vertically impact on a flat aluminum surface are simulated.

Since the problem is inherently symmetric with respect to the central axis, a 2D-axisymmetric domain was used to simulate the impact of droplets on a flat surface. It should be mentioned that a 2D-axisymmetric simulation cannot capture the instabilities that can be seen in a 3D phenomenon which may lead to splat fingering during droplet spreading. However, in the current study, the operating range is set to avoid the formation of any fragmented or growing instabilities. Nevertheless, a 2D-axisymmetric simulation captures the problem's main characteristics, including the maximum spreading diameter and the counter jet formation. Furthermore, the computational cost of 2D-axisymmetric simulation is magnificently lower than a 3D simulation. Hence, all simulations are performed in a 2D-axisymmetric domain in

this study. The computational domain and boundary conditions are shown in **Error! Reference s ource not found.**.

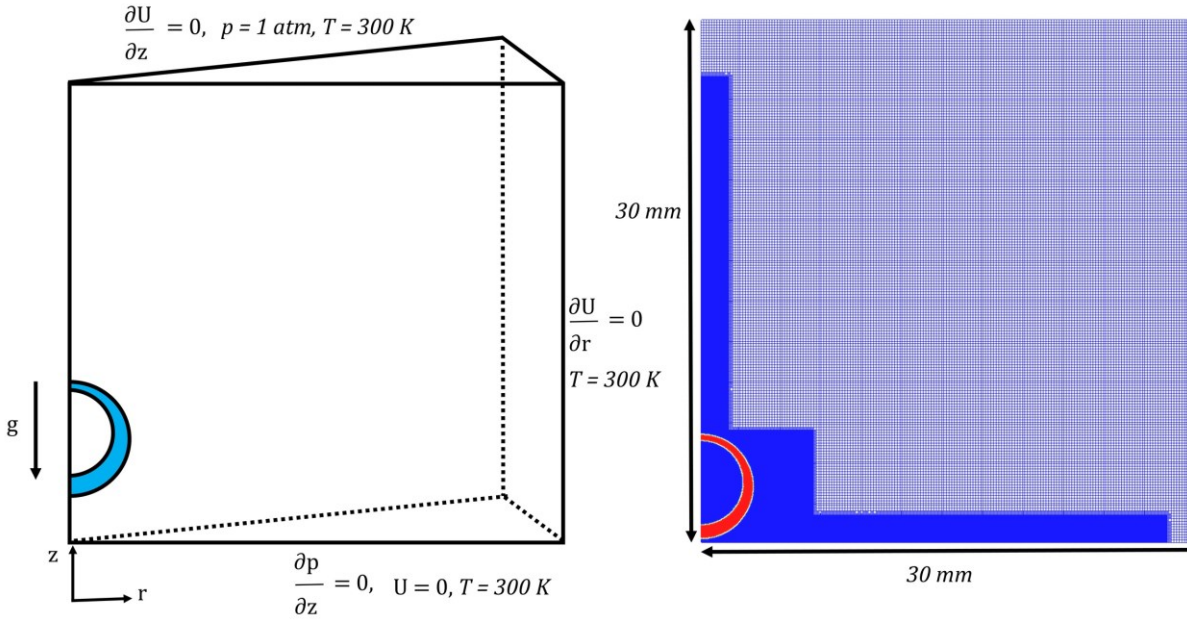

Figure 2-2. The computational domain and boundary conditions.

a structured grid with total grid numbers of 340,000 was used. The grids were concentrated closer to the symmetry axis and along the lower wall.

The behavior of a hollow droplet, including spreading and bubble ruptures, was captured in the simulations with different grid numbers ranging from 108,000 to 1,200,000. Differences in the droplet spreading diameter and the counter jet height were identified to avoid mesh dependency in the simulations results. It is observed that even though the measured parameters show different values for simulations with different numbers of grids, however, these differences are negligible for simulations with total number of grids of 340,000 or higher. Therefore, a structured grid with total grid numbers of 340,000 was used. The grids were more concentrated close to the symmetry axis and along the lower wall, where a higher gradient on variable parameters is expected.

The governing equations are conservation of mass, momentum, and energy that, along with an interface advection equation, need to be solved to simulate the droplet flattening. These equations are written as,

$$\frac{\partial \rho}{\partial t} + \vec{\nabla}.\vec{U} = 0 \tag{2-2}$$

$$\frac{\partial(\rho\vec{U})}{\partial t} + \nabla.(\rho\,\vec{U}\vec{U}) = -\vec{\nabla}p + \rho\vec{g} + \vec{\nabla}.\left\{\mu\left[\nabla\vec{U} + (\nabla\vec{U})^{T}\right]\right\} + \vec{F}_{vol} \tag{2-3}$$

$$\frac{\partial(\rho cT)}{\partial t} + \vec{\nabla}.\left(\rho c\,\vec{U}T\right) = \nabla.(k\nabla T) + \frac{\partial p}{\partial t} - \left(\frac{\partial \rho K}{\partial t} + \vec{\nabla}.\left(\rho\,\vec{U}K\right)\right) \tag{2-4}$$

where $\rho, \overrightarrow{U}, p, \vec{g}, K$and c are mixture density, velocity, pressure, gravity, kinetic energy, and the specific heat, respectively. Surface tension is considered as a source term ($\vec{F}_{vol}$) and can be calculated using the method of Brackbill et al. [72].

To solve momentum equations, the pressure field is calculated from the following equation [71]:

$$\left(\gamma\frac{\Psi_l}{\rho_l} + (1-\gamma)\frac{\Psi_g}{\rho_g}\right)\left[\frac{\partial p}{\partial t} + \vec{U}.\vec{\nabla}p\right] + \vec{\nabla}.\vec{U} = 0 \tag{2-5}$$

where Ψ_l, Ψ_g, ρ_l, and ρ_g are the compressibility and the density of liquid and gas, respectively. Defining compressibility as $\Psi = \partial\rho/\partial P$, using the ideal gas equation of state, the compressibility becomes,

$$\Psi_g = \frac{1}{zRT} \tag{2-6}$$

where z represents compressibility factor. The compressibility of liquid is,

$$\Psi_l = \frac{1}{a^2} \tag{2-7}$$

with an isothermal assumption in which parameter a represents sound velocity in the liquid. To track the interface of two fluids, the volume of fluid (VOF) equation for compressible flow should be used [71];

$$\frac{\partial(\gamma)}{\partial t} + \vec{\nabla}.\left(\gamma\,\vec{U}\right) = \frac{-\gamma\,\Psi_l}{\rho_l}\frac{Dp}{Dt} = \gamma(1-\gamma)\beta + \alpha\vec{\nabla}.\left(\vec{U}\right) \tag{2-8}$$

in which

$$\zeta = \left(\frac{\Psi_l}{\rho_l} + \frac{\Psi_g}{\rho_g}\right)\frac{Dp}{Dt} \tag{2-9}$$

By solving the above equation, the value of γ can be obtained for each computational cell. A value of $\gamma = 1$ indicates that the cell is occupied by liquid, whereas a value of $\gamma = 0$ represents a cell occupied by gas. Any value between $0 < \gamma < 1$ indicates that the cell contains a liquid-gas interface. Once γ has been determined, the surface tension force can be calculated as follows [86] ;

$$\vec{F}_{vol} = \sigma\kappa(\nabla\gamma), \qquad \kappa = -\nabla.\left(\frac{\nabla\gamma}{|\nabla\gamma|}\right) \tag{2-10}$$

Where σ and κ represent the surface tension of the liquid and the surface curvature, respectively. In this equation, $\nabla\gamma$ is a continuous function that is zero everywhere in the domain except for the transitional area at the interface. The mixture properties, including $\varphi = \{\rho, \mu, k, c_p\}$ can be obtained from corresponding values of the liquid and gas (Table 2-1) as,

$$\varphi = \gamma\,\varphi_l + (1-\gamma)\varphi_g \tag{2-11}$$

To optimize the computational time, an adaptive time-step control feature was applied that keeps the solution stable and is adjusted based on the CFL number ($Co = \frac{u_i\,\Delta t}{\Delta x}$) at the beginning of the time iteration loop [86]. Using the values of the velocity of the phase fractions and Δt from previous time steps, the maximum local CFL number (Co_0) was calculated and a new time-step was iteratively initiated as,

$$\Delta t = \min\left\{\frac{Co_{max}}{Co_0}\Delta t_0;\ \left(1+\lambda_1\frac{Co_{max}}{Co_0}\right)\Delta t_0;\ \lambda_2\Delta t_0; \Delta t_{max}\right\} \tag{2-12}$$

in which Co_{max} and Δt_{max} are prescribed values for the CFL number and time step, respectively. Moreover, at the beginning of the simulation, at a very small initial time-step (Δt_0) an intermediate time-step value is calculated by using the formula.

$$\Delta t_0^* = \min\left\{\frac{Co_{max}}{Co_0}\Delta t_0;\ \Delta t_{max}\right\} \tag{2-13}$$

Then, the intermediate value (Δt_0^*) is used as Δt_0in the new time-step calculation, providing a Co_0 close to the maximum CFL number. The time step is smoothly adjusted based on maximizing the CFL value [87].

Table 2-1. Thermophysical properties of fluids at room temperature and pressure.

	Density, ρ (Kg/m^3)	**Viscosity, μ** $(Kg/m.s)$	**Surface tension, σ** (N/m)	**Thermal conductivity, k** $(W/m.K)$	**Specific heat, c_p** $(J/Kg.K)$
Water	998	8.9×10^{-4}	72×10^{-3}	0.6	4186
Glycerol	1260	1.412	64×10^{-3}	0.292	2430
Air	1.225	1.8×10^{-5}	–	0.0242	1006.43

2.3 Experimental setup and measurements.

Impact experiments were performed at 300 K and 30% relative humidity in ambient environments. The best technique to reveal the interaction of a hollow droplet with a surface is high-speed imaging similar to a dense droplet flattening studies. However, in this case, the challenging part is the production of a stable hollow droplet. A bubble can be inserted into a droplet by triggering cavitation inside the droplet using an acoustic wave or by injecting a bubble from a needle. Although the bubble injection is more convenient for low viscosity liquids, authors faced some challenges in addition to aligning the local focus point of the high-speed camera with the impact location. The droplets are injected from a needle with an inner diameter of 2.18 mm connected to a syringe pump (Pico Plus, Harvard Apparatus, USA). Another needle was implemented inside the main needle to inject air into the liquid droplet (Figure 2-3). When a droplet was released from the main needle, the second needle was used to inject an air bubble into the droplet. Further increase in droplet mass results in detachment of the hollow droplet from the needle tip. Due to the experimental setup, the location of the entrapped bubble is usually toward the top of the droplet. The height of the needle above the surface was varied between 50 and 700 mm, resulting in impact speeds ranging from 0.5 to 3.6 m/s. A high-speed camera (Phantom v711, Vision Research, USA) recorded the impacting droplets. The process was illuminated by a lamp to enable filming of the process at a rate of 5000 fps and an exposure time of 30 μs. The images were analyzed using ImageJ software (version 1.46, National Institutes of Health, Bethesda, MD). The images were calibrated for each experiment with respect to the outer diameter of the main needle.

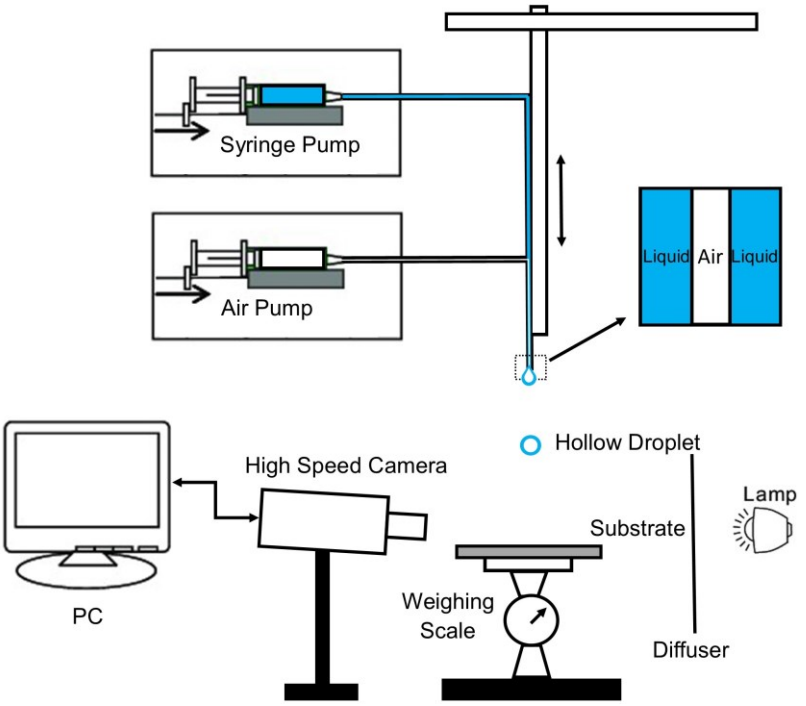

Figure 2-3. Experiments setup.

The commercially available superhydrophobic coating NeverWet was sprayed onto mirror polished stainless steel to produce the superhydrophobic surface. NeverWet consists of a flat base coat without nanoparticles and a top coat consisting of conformally coated hydrophobic nanoparticles with diameters of about 50 nm. On each sample, 3 base coats and 3–4 top coats were applied. In case of water droplet, the apparent, advancing, and receding contact angles on different surfaces are reported in Table 2-2.

Table 2-2. Measured contact angles of water on different surfaces.

	Apparent contact angle	**Advancing contact angle**	**Receding contact angle**
Aluminum	85° ± 3°	94° ± 2°	66° ± 2°
SHS	163° ± 2°	165° ± 3°	162° ± 2°
SBS	42° ± 2°	52° ± 2°	32° ± 3°

In order to measure the entrapped bubble size**,** the fall of hollow droplets from 50 mm height was recorded on the video camera, and then the spread droplets were weighed on a balance with an accuracy of to 0.05 mg. From the taken images, the outer diameters of droplet D_h, and diameter of bubble $D_{b,image}$were measured. Considering the density of water and calculating the total volume of hollow droplet, the real diameter of bubble $D_{b,actual}$ was evaluated. The measurements show that, due to fisheye effect, $D_{b,image}$ needs to be corrected. Basically, the light beams emitted from the interface of the entrapped bubble with droplet is refracted as the

environment changes. As a result, on the recorded image, the interface of the two fluids appears larger than its actual size. Therefore, a correlation between the interface diameter that the observer sees, and the actual diameter needs to be devised. In order to find the accurate value of measured lengths, a modification constant should be defined. For the case of hollow droplet, this modification constant is calculated with the help of information obtained from impact of hollow droplet at low velocity with the detail mentioned below. Then, the modified constant was used to calculate the accurate size of the entrapped bubble at impact with high velocities.

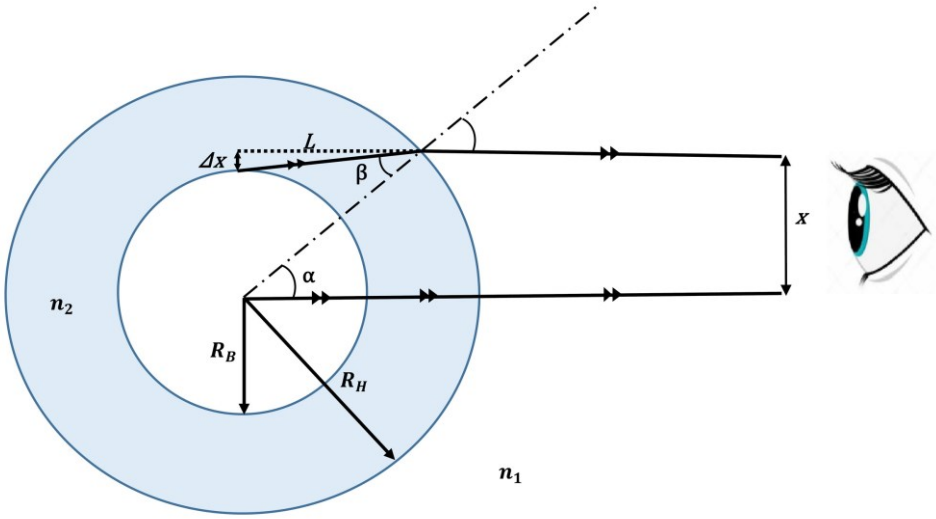

Figure 2-4 Fisheye effect for a hollow droplet.

Figure 2-4 shows the path of the light beams from their origin in the cross-section of a hollow water droplet to the observer. In order to simplify calculations, it is assumed that the bubble is located at the center of the droplet and the hollow droplet is axisymmetric. In Figure 2-4, R_b is the radius of the interface of bubble and droplet, R_h is the droplet outer radius, and x is the bubble radius that the observer sees. The refractive index used for the environment is air (n_1), and the droplet is water (n_2). For angles α and β, one can write,

$$Sin\ \tau = \frac{x}{R_h} \tag{2-14}$$

also,

$$Cos\ \tau = \frac{L}{R_h} \tag{2-15}$$

while,

$$n_1\ Sin\ \tau = n_2\ Sin\ \varsigma \tag{2-16}$$

In addition,

$$tan\,(\tau - \varsigma) = \frac{\Delta x}{L} \tag{2-17}$$

in which,

$$R_b = x - \Delta x \tag{2-18}$$

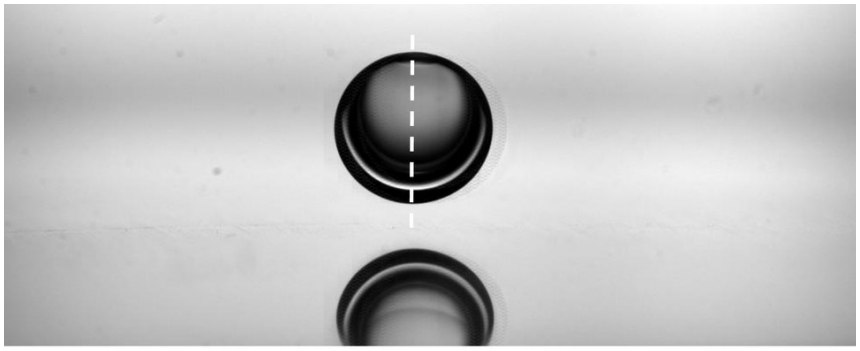

Figure 2-5. A snapshot of the hollow water droplet before impact on a surface.

The $D_h = 5.06\ mm$ droplet was released from a height of 50 mm to avoid the counter jet breakup. The spread droplet was weighed on a balance accurate to 0.05 mg. The weight of the single droplet was measured and was equal to $m_h = 37\ mg$ which gives a total volume of $Vol_{eq} = 36.93\ mm^3$ for a dense water droplet. Based on these numbers, the diameter of the dense droplet with the same mass will be $D_{eq} = 4.1\ mm$. This is while the outer diameter of the hollow droplet measured from the image is equal to $D_h = 5.06\ mm$ which gives a volume of $Vol_h = 68\ mm^3$. The volume of the entrapped bubble can be calculated as, $Vol_b = Vol_h - Vol_{eq}$, which gives $Vol_b = 31.07\ mm^3$ and, therefore, the bubble diameter will be equal to $D_b = 3.9\ mm$.

The measurements were repeated for 10 droplets and, using the above-mentioned equations, and the following correlation is obtained to calculate the actual size of the bubble from taken images,

$$D_{b,actual} = 0.86 * D_{b,image} \tag{2-19}$$

To ensure the integrity of the correlation, results were validated with the results of equation (2-19). It was observed that the calculated results from the correlation have less than 6% error compared to the measured data, which might be due to axisymmetric assumption during the calculation. This means that the proposed correlation is in good agreement with the experimental data. It is noted that these measurements can only be applied to low-velocity droplet impact because at high-velocity droplet impact, the counter jet detaches from the surface, and the actual mass of the initial droplet cannot be determined. For these cases, the size of the bubble should be calculated with the help of experimental images. Nevertheless, the

measurement of the bubble's diameter from the image is not the exact value of entrapped bubble diameter and, due to the light reflection, the fisheye effect should be considered.

2.4 Results and discussion

When a hollow droplet impacts a surface, it flattens in the lateral and azimuthal directions. However, at the same time, a unique phenomenon happens. During the spreading phase, a portion of the liquid lifts off from the surface and forms a counter jet which finally leaves the surface (Figure 2-6.a). It is observed that during the impact of the hollow droplet, the liquid phase of the droplet moves inward and outward of the center of the droplet at the contact location of entrapped bubble shell (Figure 2-6.b). A portion of liquid moves outward of the center, which results is the flattening of a hollow droplet while the other moves inward the center of the droplet and forms a counter jet. This counter jet grows till it reaches a narrow and long liquid jet and then starts to break up. This separated part of liquid leaves the surface and does not recoil to the main droplet.

In order to understand this phenomenon, experiments were repeated for dense and hollow droplets, and results were compared with each other. Considering an equal mass for both hollow and dense droplets, an equivalent diameter is calculated, which indicates the size of a dense droplet with the same mass as a hollow droplet (D_{eq}) and consequently the same initial kinetic energy.

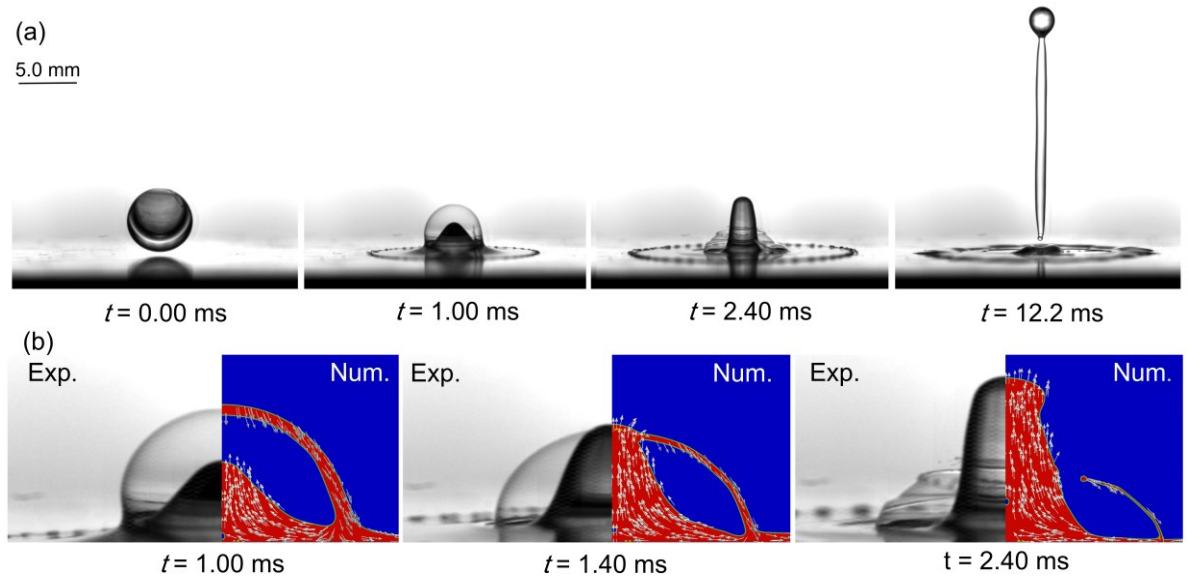

Figure 2-6. Selected snapshots showing a hollow water droplet with an external diameter $D_h = 5.6\,mm$ and internal diameter $D_b = 4.5\,mm$ impacting with velocity $\vec{U} = 3.6\ m/s$ on an aluminum surface.

Impacting an aluminum surface (Figure 2-7.a), the dense water droplet flattens on the surface until it reaches its maximum spreading radius at time $t = 5.0\,ms$ then retracts toward the center. This retracting liquid makes an oscillating bulk of water on the surface until it stabilizes. There is no liquid detachment from the surface during the whole process. On the contrary, the behavior of hollow droplets is different (Figure 2-7.b); when a hollow droplet impacts an aluminum surface, it flattens in the lateral direction, however at the same time, a counter jet forms in the axial direction at about $t = 0.2\,ms$. This counter jet crosses the upper shell of the entrapped bubble at $t = 1.4\,ms$. The rupture of bubble shell occurs later at $t = 2.8\,ms$. The hollow droplet reaches its maximum spreading radius at $t = 5.0\,ms$ while the central jet is still growing and eventually breaks up from the spreading liquid at $t = 12.4\,ms$. As a result of this breakup, a portion of liquid mass detaches from the surface while the remaining liquid is stabilized and takes a semicircular shape similar to the dense droplet. Dimensionless numbers including $Re = \frac{\rho\, U\, D_{eq}}{\mu}$ and $We = \frac{\rho\, U^2 D_{eq}}{\sigma}$ are calculated for both dense and hollow droplets based on the equivalent diameter of the hollow droplet. Here, $\rho, U, D_{eq}, \mu, \sigma$ represent density, impact velocity, equivalent diameter of the hollow droplet, viscosity, and surface tension, respectively.

The bouncing of droplets from a surface had been reported in many investigations. For example, droplets impacting on a superhydrophobic surface can bounce off quickly because of the low friction between the drop and the substrate [88] or at their maximum extension in a pancake shape [89] at low Weber numbers. Nevertheless, droplet detachment on a non-superhydrophobic surface has a totally different mechanism. In the following parts, the effects of surface wettability, liquid type, and impact velocity of hollow droplets on the formation of splat and counter jet are investigated.

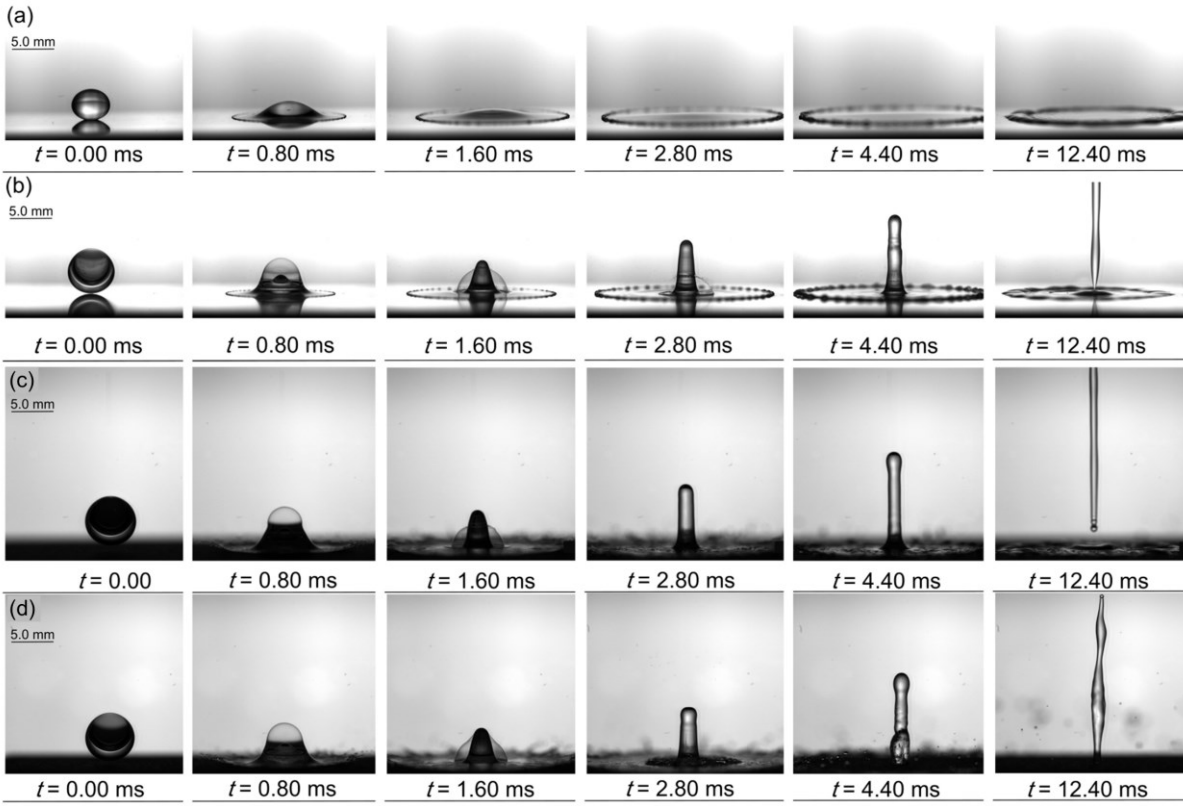

Figure 2-7. Selected snapshots of the impact of a dense and hollow droplet.
A dense water droplet with a diameter of $D_d = 4.4\ mm$ impacting on an aluminum surface, (a) hollow water droplets with $D_h = 5.6\ mm$ and $D_b = 4.5\ mm$ impacting on different surfaces including aluminum, (b) sand-blast steel, SBS, (c) and superhydrophobic (d). The mass and the impact velocity of all droplets are $m = 0.044\ g$ and $U = 3.6\ m/s$, resulting in $Re = \frac{\rho\ U\ D_{eq}}{\mu} = 17760,\ We = \frac{\rho\ U^2 D_{eq}}{\sigma} = 790$.

In order to understand the effects of surface wetting, the experiments of hollow droplet impact were repeated on different surfaces, including sand-blasted steel (SBS) and superhydrophobic (contact angles of each surface are reported in Table 2-2).

The dense droplet detachment from the surface was reported in the previous studies in the shape of droplet fragmented, corona phenomenon, or even droplet recoiling from the surface on superhydrophobic surfaces [90]. In order to study the effect of surface wettability on the hollow droplet flattening, experiments were repeated on surfaces with high and low wettability values. Figure 2-7.c shows snapshots of the hollow droplet impact on the sand-blast steel (SBS) surface. Sandblasting has been used to increase the surface wettability of hydrophilic surfaces. The spreading of the droplet on the SBS surface is different compared to the aluminum surfaces. The droplet spreads while attaching to the SBS surface till $t = 0.8\ ms$ and after that it lifts off from the surface and takes a splash form as a result of the higher dynamic contact angle [91] and droplet velocity. Even though the liquid is in contact with the surface at the

center, it has no contact at the spreading edges. However, the formation of the counter jet is totally similar to what has been observed on the aluminum and SBS surfaces where the counter jet detaches from the surface at $t = 12.4\,ms$. At the end, because of counter jet detachment and fragmented, a small portion of liquid remains on the surface which takes a disk shape due to high wettability of the surface.

In the last case, the hollow droplet impact has been investigated on a superhydrophobic surface with low wettability and high intrinsic contact angle (Table 2-2) (Figure 2-7.d). The high contact angle of the surface accompanied with high impact Weber number ($We = 790$) lead to droplet fragmented from the edges during spreading. At the same time, a counter jet takes shape in the axial direction at the center, which has a higher volume compared to the impact on the other surfaces. In the end, the liquid leaves the surface either by fragmented from spreading edges or by counter jet detachment. In addition, it is observed that the counter jet formed on a superhydrophobic surface has a wavy shape while it has a uniform shape on the aluminum, stainless steel, and sandblast steel surfaces. These waves are imposed to the surface of the counter jet because of small waves formed on the droplet's surface during spreading. These waves can be damped on surfaces with high wettability. This is while these waves do not dissipate on superhydrophobic surfaces and change the shape of the counter jet.

It should be mentioned that there are fundamental differences between dense and hollow droplets bouncing from a superhydrophobic surface due to the formation of a counter jet in the hollow droplet impact. The counter jet forms before the retraction time, while in the case of the dense droplet, bouncing and formation of the counter jet occur at the end of retraction. The shape of the jet resembles a long pillar, which is totally different from what has been reported in dense droplet bouncing [88]. In addition, dense droplet bouncing occurs only at low Weber numbers while counter jet forms at high Weber numbers. Therefore, the low wettability of the surface cannot justify the formation of counter jet during hollow droplet impact on the surface. It should be noted that there are minor differences in the behavior of the hollow droplet during impact on the surfaces with high and low wettability. The shape of the counter jet formed on the surfaces with moderate or high wettability is uniform with no perturbation on the jet surface, while the counter jet formed from the low wettability surface is totally perturbed.

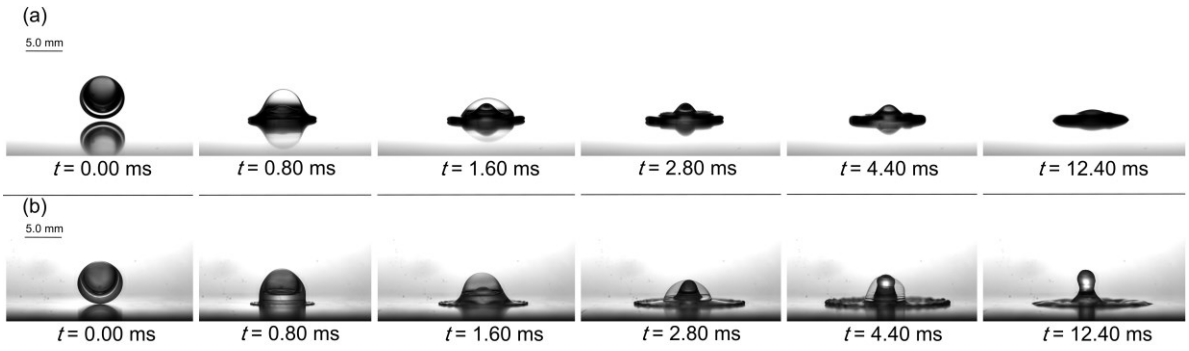

Figure 2-8. Selected snapshots show the impact of dense and hollow droplets on the aluminum surface. (a) A hollow glycerol droplet with a diameter $D_{Gly,h} = 5.6\ mm$ impacting with velocity $U = 3.6\ m/s$. $Re = 14$, $We = 1122$. (b) A hollow water droplet with $D_h = 5.6\ mm$ and $D_b = 4.5\ mm$ impacting with $U = 1.0\ m/s$, $Re = 5070$, $We = 60$.

In order to understand the effects of liquid type, the experiments were repeated with hollow glycerol droplets. Figure 2-8.a illustrates the behavior of a hollow glycerol droplet during impact on the aluminum surface. Like the hollow water droplet impact on the aluminum surface, a counter jet starts forming after the droplet impact. Nevertheless, the spreading radius, the rupture time of the bubble shell, and the counter jet length are different than the values measured for the hollow water droplet. It appears that increased viscosity damps the droplet inertia and confines maximum spreading radius and counter jet length, while the formation of counter jet still can be observed. Figure 2-8.b shows a smaller spreading radius and counter jet height of hollow water droplet impacting with low velocity ($\vec{U} = 1.0\ m/s$) on the surface. In addition, the height of counter jet is almost the same at time $t = 4.40\ ms$ and $t = 12.40\ ms$ which means that the counter jet does not leave the surface and returns to the splat. Even though the size of the counter jet is affected by droplet impact velocity and liquid viscosity, it is shown that the presence of the counter jet is inevitable. Although the counter jet crossing the upper shell expedites the bubble rupture, the bubble rupture occurs even in cases with low impact velocities in which the counter jet cannot reach the upper shell of the bubble.

Figure 2-9 presents the flattening characteristics of a hollow water droplet on an aluminum surface at different velocities. Similar to a dense droplet, the spreading radius of the hollow droplet decreases as impact velocity decreases (Figure 2-9.a). The height of the counter jet is another parameter affected by droplet velocity variation. It is shown that impacting the surface with a lower velocity, the droplet has a smaller counter jet (Figure 2-9.b). For a droplet impacting with high velocity, the velocity trend has a linear shape, while for low-velocity impact, it takes a curved shape. This means that the counter jet forms after impact at low velocities but will return to the droplet and does not detach from it.

(a) (b)

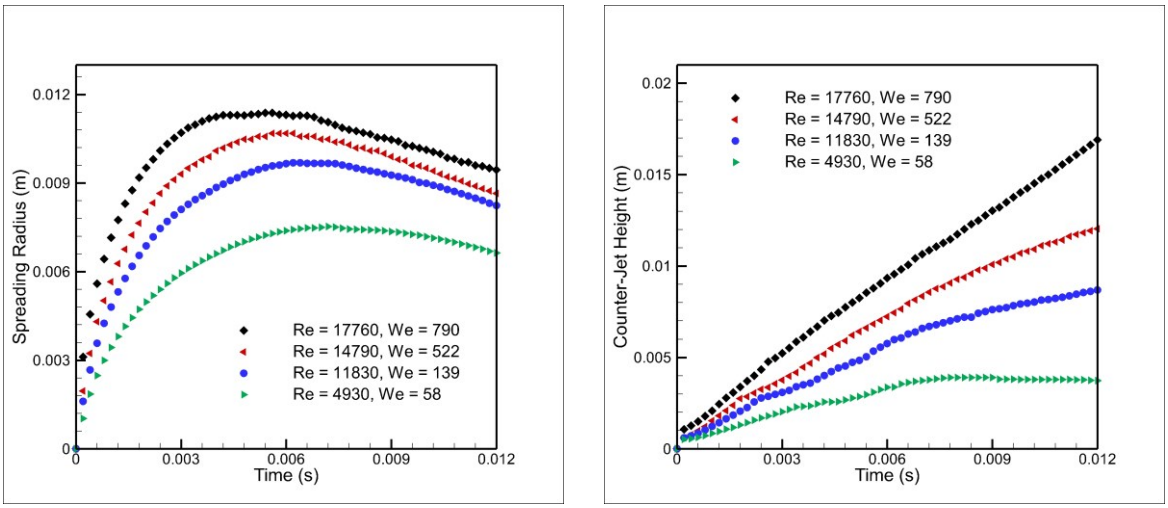

Figure 2-9. Flattening by the time of hollow water droplet.

$D_h = 5.6\,mm$ and $D_b = 4.5\,mm$ for impacts at different velocities ($U = 1, 2.4, 3.0, 3.6$ m/s corresponding to $Re = 4930, 11830,\ 14790,\ 17760$ and $We = 58, 139, 552, 790$, respectively): (a) experimental results of spreading radius, (b) experimental results of the counter jet height.

In order to better understand the mechanism of the formation and detachment of liquid counter jet, a compressible multiphase solver has been utilized to solve the equations governing the physics of the drop flattening on a surface. A 2D axisymmetric numerical simulation has been performed in order to provide more information about hollow droplet impingement. The initial simulation condition is the same as the conditions in which experiments were done. Comparison of the numerical results with experimental data shows that the evolution of drop shape during spreading and formation of the counter jet is qualitatively the same (Figure 2-6.b). Information about parameters such as counter jet tip velocity or variation of the pressure of entrapped bubble during impact is being extracted from numerical simulation to provide a good insight about the physical procedure inside a hollow droplet that leads to the formation of the counter jet.

Figure 2-10 shows mesh independence tests for hollow water droplet flattening. Based on the results for the spreading diameter and the counter jet height, it is shown that by increasing the grid numbers inside the domain, the accuracy of numerical results are increases. However, differences between numerical results with 340000 grids and 1200000 grids are negligible, and in order to prevent high computational cost, total grid numbers of 340000 is chosen for the rest of the numerical simulations.

(a) (b)

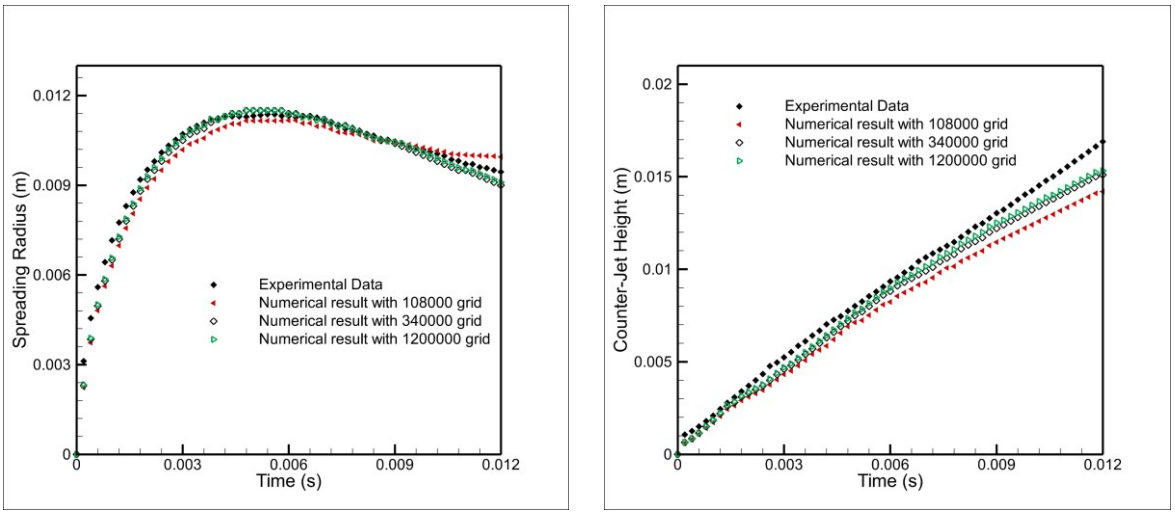

Figure 2-10. Mesh independency tests for hollow water droplet flattening.
$D_h = 5.6\,mm$ and $D_b = 4.5\,mm$ impacting at $U = 3.6$ m/s (corresponding to $Re = 17760$ and $We = 790$, respectively): (a) the spreading radius vs. time, (b) the counter jet height vs. time.

Figure 2-11 shows droplet flattening characteristics of dense and hollow droplets after impact obtained from experiment and numerical simulation. Figure 2-11.a demonstrates the temporal evolution of droplet spreading for water and glycerol droplet. After the impact, both droplets flatten till they reach their maximum spreading radius and then start to recoil. Both dense and hollow droplets have the same inertia before impact on the surface; however, the hollow droplet loses some of its energy during the formation of the counter jet. As a result, the spreading radius of the hollow droplet decreases compared to that of the dense drop.

(a) (b) (c)

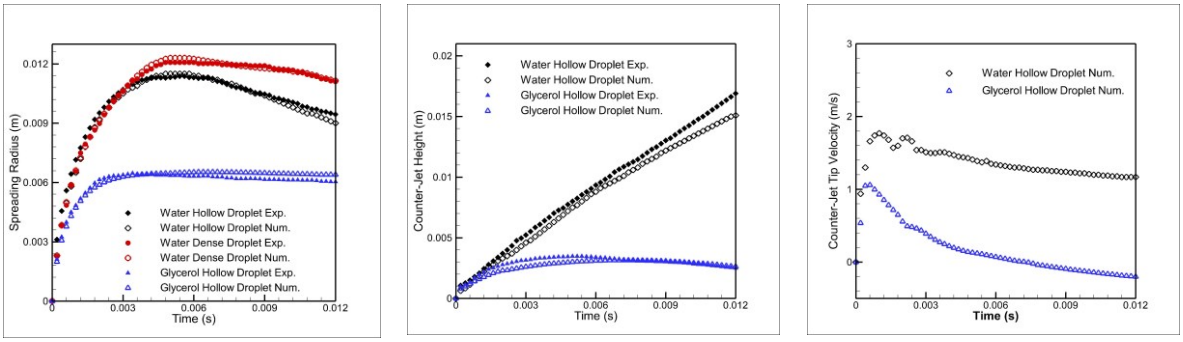

Figure 2-11. Droplet flattening characteristics.
(a) experimental and numerical results of spreading radius over time for hollow water and glycerol droplets, (b) experimental and numerical results of the counter jet height of hollow droplet over time for water and glycerol droplet, (c) numerical results of counter jet tip velocity along time for hollow water and glycerol droplet. (Water droplet at $Re = 17760$, We $= 790$, glycerol droplet at $Re = 14$, $We = 1122$).

In the case of glycerol drop, even though it has a higher Weber number before impact since it has a higher viscosity, Re number is drastically lower than a water droplet, leading to a lower spreading radius for the glycerol drop. In addition, its higher viscosity affects the formation of the counter jet, which is shown in Figure 2-11.b. For both glycerol and hollow water droplets, the formation of counter jet starts after impact. The length of the counter jet increases linearly by time for the case of water drop, while it has a curvy diagram for glycerol. It seems that the higher viscosity of glycerol cannot prevent the formation of the counter jet but damps and stops its growth.

Figure 2-11.c presents the counter jet tip velocity for the hollow water and glycerol drops. The counter jet tip velocity increases right after impact, which is followed by the formation of the counter jet. The positive slope of the counter jet tip velocity continues until it reaches a peak. After this peak, the tip velocity slope reduces and approaches zero. Some other differences are visible between the diagrams of water and glycerol droplets. The positive slope of glycerol is smaller than that of water. After reaching the peak, both diagrams show a tip velocity decreasing tendency. This tendency gradually decreases the counter jet tip velocity of water while this decrement occurs in a shorter time for glycerol. These differences are the result of the higher viscosity of glycerol which tends to dampen the liquid movement.

The other differences between water and the glycerol counter jets are the time and magnitude of the tip velocity peak. The diagram of the water droplet has a higher peak than that of the glycerol droplet, in which glycerol's higher viscosity can justify that. The viscosity is the primary locator of tip velocity peak for glycerol, while in the case of the hollow water droplet, it occurs during the interaction of the counter jet tip with the upper bubble shell. In addition, there is another small peak for a hollow water drop, representing the bubble rupture time, while this small peak is not observed in the glycerol case.

To interpret the mechanism of the formation and detachment of the liquid counter jet, a comparison between numerical simulation of a dense and a hollow droplet is presented in Figure 2-12. When a dense drop impacts the surface, the velocity vectors are directed toward the surface at about $t = 0.15\ ms$ (Figure 2-12.a) and a pressure increase occurs at the contact point of drop and the surface. The pressure gradient smooths out gradually toward the upper interface of the water droplet (Figure 2-12.b). With time progress, the high inertia of the upper portion of drop and a gradient of pressure along the z-axis prevents liquid from moving upward. Hence, liquid moves toward the low-pressure regions at the edges, and droplet flattens on the surface.

In the case of hollow droplet impact, there is a pressure distribution similar to the one reported in the dense droplet case. However, it has a jump at the interface of liquid and gas, which leads to the deformation of the bubble accompanied by the formation of a liquid counter jet (Figure 2-12. c, d). The direction of velocity vectors of the hollow droplet during the initial time steps of the impact confirms this interpretation.

Velocity vectors in Figure 2-12. c shows the upward liquid movement on the symmetric axis at $t = 0$. The volume of the upward moving liquid grows by time, and the liquid counter jet takes shape. Three high-pressure local zones can be detected during the hollow droplet flattening.

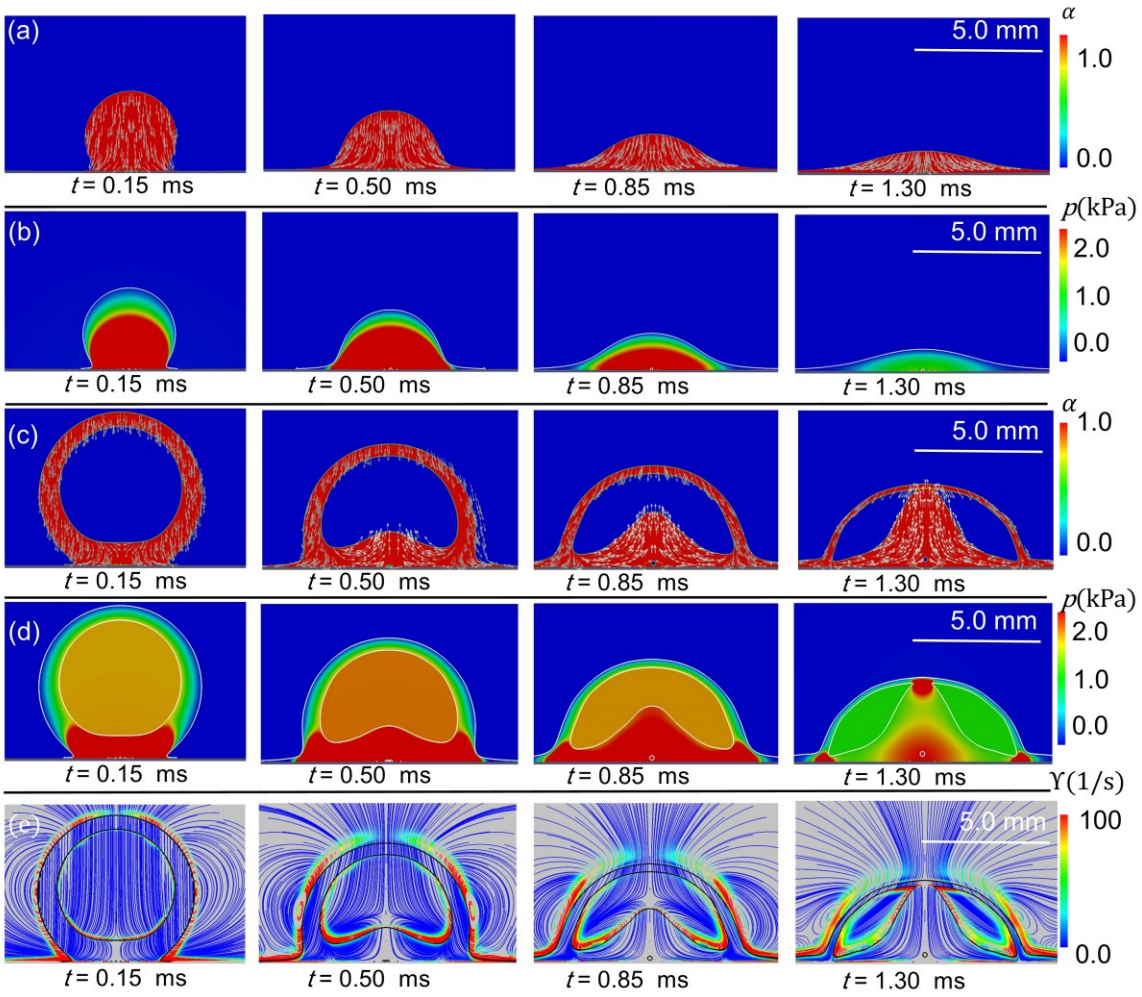

Figure 2-12. Snapshots of drop flattening and initiation of the counter jet formation for water drop at $Re = 17760$, $We = 790$.

(a) velocity vectors inside a dense droplet, (b) pressure distribution inside a dense droplet, (c) velocity vectors inside a hollow droplet, (d) pressure distribution inside a hollow bubble, (e) velocity streamlines and vorticity contours inside a hollow water droplet on an aluminum surface ($U = 3.6\ m/s$).

The strongest one is at the center of the spreading axis, which is similar to what was observed in the dense droplet, and the two others are at contact points of the upper bubble shell with the spreading liquid. The liquid in the upper shell is deflected by these local pressure zones. A portion of this liquid is forced to move toward the center while the rest is joined to the spreading liquid (Figure 2-12. d, e).

In other words, when a dense droplet impacts a surface, it spreads on the surface and moves radially due to the high pressure of the downward moving liquid. As a result, the kinetic and surface energies of the droplet before impact convert to the surface energy of the spreading droplet and dissipate through viscosity. The equilibrium between these energies determines the spreading diameter of the droplet. In the case of hollow droplet impact, the droplet can move radially on the surface toward and outward the impact location because of the lack of high-pressure liquid at the location of the entrapped bubble. As a result, a counter jet forms on the surface of the spreading liquid, which contains a portion of initial energy in the form of kinetic and surface energy. Considering the equilibrium between energy before and after impact, the spreading part of the hollow droplet has less energy to spread on the surface than the dense droplet. As a result, a smaller spreading diameter is observed for the hollow droplet in comparison to the dense droplet.

The flattening trend of the dense and hollow droplets is illustrated in Figure 2-13. Impacting the solid surface, the dense droplet spreads until it reaches its maximum radius at $t = 5.0\ ms$ (Figure 2-13.a), while for the case of the hollow droplet, the maximum spreading occurs at $t = 4.6\ ms$ (Figure 2-13.b) and a counter jet takes shape on the surface which uniformly grows. Figure 2-13.c demonstrates the difference between the spreading radius of dense and hollow droplets at the same time.

Considering the amount of liquid that leaves the surface as the counter jet, the spreading radius of the dense droplet is expected to be larger than the hollow droplet, and a distinguishable difference between the spreading radius is expected. The total trend of spreading radius is the same. Nevertheless, the difference between these values is smaller than the predicted values.

In order to explain the different behaviors of the dense and hollow droplets, their energy before and during impact needs to be considered. Kinetic and surface tension energies are two forms of energy that are involved before the droplet impact. Both dense and hollow droplets have the same kinetic energy before impact due to their equal mass and velocity.

(a) (b) (c)

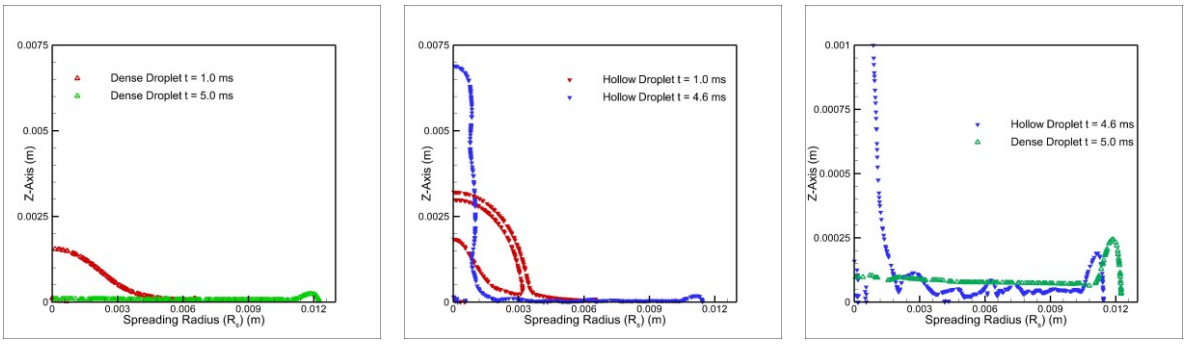

Figure 2-13. The free surface of water droplet during impact on the aluminum surface (the time taken to reach the maximum spreading of the hollow droplet is $t = 4.6\ ms$ and the one for dense droplet is $t = 5.0\ ms$. (a) dense droplet ($D_d = 4.4\ mm$), (b) hollow droplet ($D_h = 5.6\ mm$, $D_b = 4.5\ mm$), and (c) dense and hollow droplets focused on the shape of spreading, $Re = 17760$, $We = 790$.

Nevertheless, the surface tension energy stored in the hollow droplet is higher than the dense one because of the bubble inside the droplet. After impacting the dense droplet, these energies are partly dissipated by the viscosity, and the rest is converted to the surface tension of the spreading droplet until the droplet reaches its maximum flatness. In the case of the hollow droplet, a portion of initial energy leaves the surface as a counter jet and cannot associate the droplet spreading. However, the velocity of the counter jet is less than the droplet impact velocity (Figure 2-11.c). This means that even though a portion of this energy is dissipated through the viscosity, the remaining is transformed to the flattening liquid. Furthermore, the formation of the liquid counter jet leads to the compression of entrapped air. After rupturing the bubble, the compressed air with the high surface tension of the thin ruptured shell pushes the liquid toward the surface. This high-energy liquid imposes disturbances on the interface of spreading liquid. These statements might justify why the less amount of liquid that spreads in the case of the hollow droplet is compensated by its less spreading thickness.

The oscillations on the free surface of the hollow droplet splat compared to a smooth splat of the dense droplet is an important issue that was noticed (Figure 2-13.c). These oscillations which result from the bubble rupture find unique importance in the thermal spray process. When a splat solidifies, these oscillations make a solidified layer with higher roughness and allow the production of a coating with a higher porosity which is essential in the production of thermal barrier coatings.

2.5 Conclusions

The experimental and numerical results confirm that the impacts of dense and hollow droplets are significantly different from each other. Impacting a solid surface, the entrapped bubble in the hollow droplet deforms and breaks the droplet internally. Then, a counter jet forms, which, if its energy overcomes the potential and dissipation energy, will detach from the droplet and leave the surface. Results show that the variation of initial impact momentum, viscosity, and surface wettability changes the spreading of the droplet and formation of the counter jet. In addition to helping better understand the impact process of hollow droplets, the results are valuable for better controlling the energy and mass transfer between droplets and the surface with applications in biomedicine and thermal spray coating.

3 Chapter Three: Flattening of a hollow droplet impacting a solid surface

The content of this chapter has been submitted to the Journal of Fluid Mechanics, in January 2022.

3.1 Introduction

Droplet impingement on a solid surface is a widely appearing phenomenon. Falling a raindrop on a leaf or ground [2], ink-jet printing [92], and thermal spray coating [23] are good examples of droplet impact in nature and industry. In the past decades, the parameters affecting droplet impact outcome have been extensively studied through experimental [93-97], analytical [8, 9, 98, 99], and numerical modeling [100-102] investigations. The main influencing parameters are droplet size, droplet velocity, droplet type, and surface wetting conditions. To address the droplet impact and spreading dynamics, dimensionless numbers such as $\mathrm{We} = \frac{\rho U_0^2 D_{eq}}{\sigma}$, $\mathrm{Re} = \frac{\rho U_0 D_{eq}}{\mu}$, $\mathrm{Oh} = \frac{\mu}{\sqrt{\rho \sigma D_{eq}}}$, and $\mathrm{Ca} = \frac{\mu U_0}{\sigma}$ are employed known as Weber, Reynolds, Ohnesorge, and Capillary numbers, respectively. In these parameters, ρ, D_{eq}, U_0, σ and μ represent density, equivalent diameter, velocity, surface tension, and viscosity of the droplet, respectively.

In addition to the impingement of regular droplets on a surface, there are special cases that deal with hollow droplets containing void inside their volume (Figure 3-1). The interaction of hollow droplets with a rigid wall occurs in the fields of controllable biomedicine [41-43, 103], thermal spray coating [19, 44], cavitation [35], and lithotripsy [104]. It should be mentioned that the hollow droplet is different than the bubble entrapment after droplet impact on a liquid pool [105] or a surface [101, 106].

Although there are thousands of publications on dense droplet impingement, only a few studies have focused on the impact of a hollow droplet on a surface. Solonenko et al. studied the deposition of hollow sphere yttria-stabilized-zirconia (YSZ) during plasma thermal spray coating [19]. They noticed fundamental differences in the behavior of dense and hollow droplets during impact on a surface. It was shown that zirconia splats produced by the collision of hollow sphere particles to the substrate have a more stable character compared to splats formed by dense droplets. The reason behind this is not fully understood yet. Gulyaev et al. investigated the impingement of hollow glycerin droplets. They observed the formation of a liquid counter-jet due to the hollow droplet impact on a surface for the first time [47]. Kumar and Gu applied the Volume Of Fluid (VOF) method to incompressible Navier-Stokes equations and numerically investigated the flattening and solidification of a hollow droplet in plasma thermal spraying conditions [49]. A modified VOF-based numerical method was applied by Safaei et al. to consider the effects of gas compressibility along with liquid solidification during the high-velocity impact of a hollow droplet [17].

Moreover, a combined Level Set-Volume Of Fluid (CLSVOF) numerical simulation was performed to study the effects of gas pressure on the flattening of the hollow droplet [84]. Recently, the authors have conducted experimental and numerical investigations on the flattening of the hollow droplet and described its differences with the flattening of the dense droplet [107]. It was shown that even though a portion of liquid of hollow droplet leaves the surface as counter-jet, however, the maximum spreading diameter of the hollow droplet is similar to that of the dense droplet with the same mass [107].

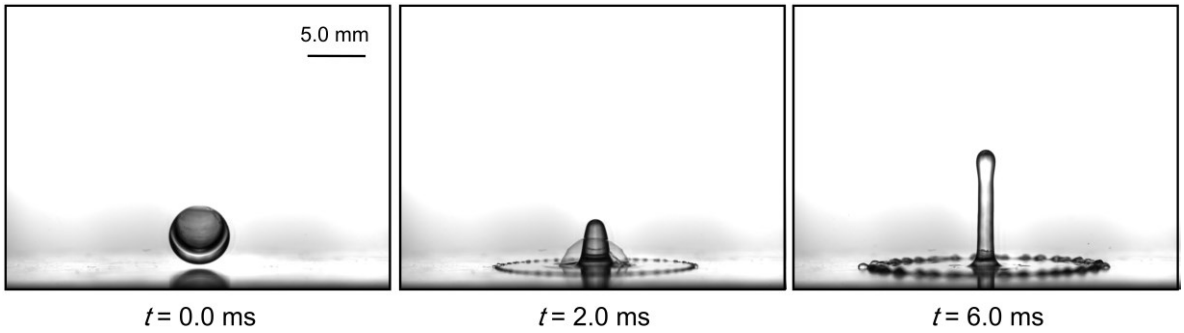

Figure 3-1. Impingement of a hollow water droplet with a speed of surface $U_0 = 3.6\, m/s$ on an aluminum surface [107].

Generally, when a hollow droplet impacts a surface, it spreads, and simultaneously a counter-jet takes shape inside the entrapped bubble (Figure 3-1) [107]. The counter-jet grows during the flattening of the hollow droplet, passes through the trapped bubble, and compresses the air inside the bubble, leading to bubble rupture. This bubble rupture induces perturbations on the surface of the spreading droplet. The counter-jet grows and, depending on the impact velocity of the hollow droplet, breaks up and detaches from the surface or recoils toward the surface.

To better understand the flattening process of a hollow droplet, in this work, a comprehensive experimental and numerical study is performed on hollow water droplets impacting a surface. The effects of bubble size and location on spreading diameter, counter-jet shape, and splat thickness are investigated. Consequently, a theoretical study is performed to calculate the maximum spreading of a hollow droplet after impact on a surface.

3.2 Experiment setup and measurements

The schematic of the experimental setup is shown in Figure 3-2. Impact experiments were performed at room temperature with 40% relative humidity in the ambient environment. The droplets are injected from a needle with an inner diameter of 2.18 mm connected to a syringe pump at a flow rate of 50 μL/ min (Pico Plus, Harvard Apparatus). Another needle was

implemented inside the main needle to inject air into the liquid droplet, where the tip of both needles was located at a line. When a droplet started to form at the tip of the liquid needle, the second needle was used to inject an air bubble into the droplet. The gas injection process was done with constant flow rate, manually. Liquid and air injection were continuous until further increment in the droplet weight causes the hollow droplet detachment from the needle tip. It should be mentioned that the proposed setup is capable of producing hollow droplets, but the size of hollow droplets produced vary significantly and the experiments had to be repeated several times to produce a hollow droplet with almost exact sizes.

The height of the needle above the surface was varied between 50 and 700 mm, resulting in impact velocities ranging from 0.5 to 3.6 m/s. A high-speed camera (Phantom v711, Vision Research) recorded the impacting droplets. The process was illuminated by a lamp enabling filming the process at a rate of 5000 fps and an exposure time of 30 µs. The video signal was recorded in the memory of a PC, and the images were analyzed using ImageJ software (version 1.46, National Institutes of Health, Bethesda, MD).

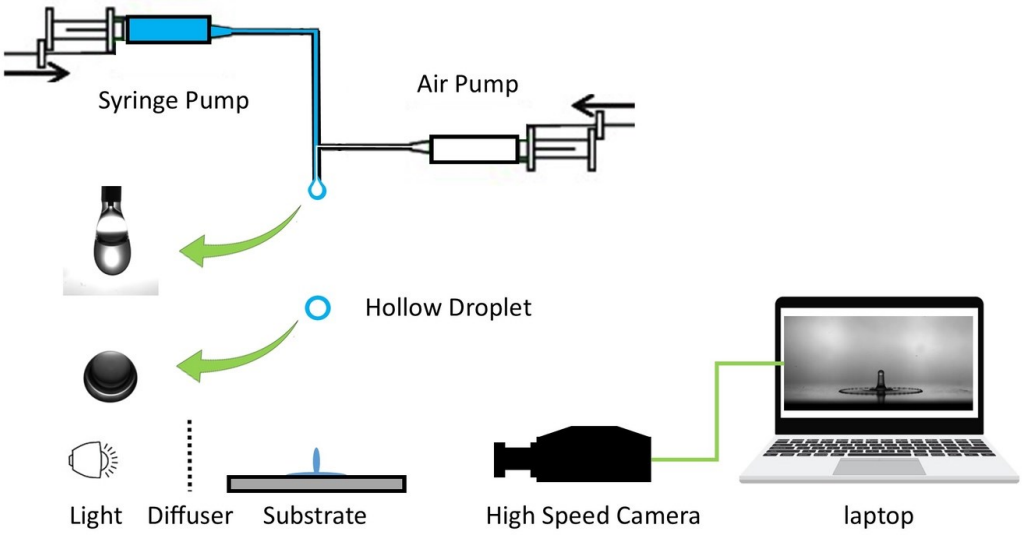

Figure 3-2. The schematic of the experimental setup of hollow droplet impact.

The apparent, advancing, and receding contact angles of a water droplet on the aluminum surface were measured as 85°±2°, 94 °±2°and 65°±2°, respectively. The fall of hollow droplets from 50 mm height was recorded on the video camera, and the spread droplets were weighed on a balance accurate to 0.05 mg. From the taken images, the outer diameter of the droplet (D_h), and the diameter of the bubble ($D_{b-image}$) were measured. Considering the density of water and calculating the total volume of the hollow droplet, the actual diameter of the bubble (D_b) was evaluated. Measurements show that, due to the fisheye effect, $D_{b-image}$ is not equal

to D_b and it needs to be corrected. These measurements were repeated for ten droplets, and at the end, the following correlation was derived from calculating the actual size of the bubble from token images,

$$D_b = 0.86 * D_{b-image}. \quad (3\text{-}1)$$

The details of the hollow droplet size calculations and experimental setup are presented in the previously published article of Nasiri et. Al. [107]. To report the experimental data, ten similar hollow droplets with less than 10% standard deviation in the size of droplet and bubble were measured.

3.3 Numerical analysis

To explain the experiments and provide a better understanding of the reasoning behind the formation and detachment of liquid counter-jet, a numerical model has been utilized to solve compressible continuum equations for the drop flattening on a surface. Figure 3-3 shows schematics of a hollow droplet impacting a flat surface. Several parameters are defined to characterize this process. The main geometrical parameters are the initial diameter of the hollow droplet (D_h) and initial diameter of the bubble inside the hollow droplet (D_b) which are shown in the Figure 3-3.a. The flattening of a hollow droplet is schematically shown in Figure 3-3.c showing the related parameters of counter-jet diameter (D_{cj}), counter-jet height (h_{cj}), counter-jet velocity (U_{cj}), spreading diameter (D), splat height (h), spreading velocity (U_R). Equivalent diameter (D_{eq}) of a hollow droplet is defined as the diameter of a dense droplet with the same weight (Figure 3-3.b). These diameters are related to each other by the definition of α, β parameters as,

$$D_h = \alpha D_{eq}, \quad D_b = \beta D_{eq}. \quad (3\text{-}2)$$

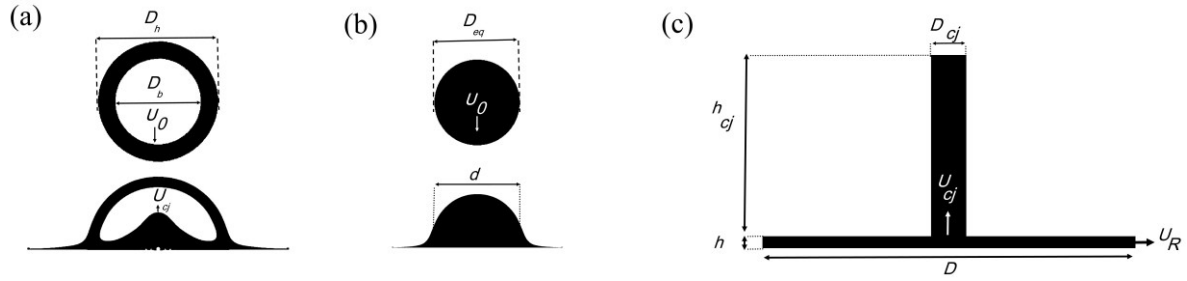

Figure 3-3. Geometrical model of a droplet impacting a flat surface.

(a) hollow droplet before and after impact, (b) dense droplet before and after impact, (c) hollow droplet spreading after impact.

From equation set (3-2), it can easily be concluded that $\alpha^3 - \beta^3 = 1$. To study the impact process, a hollow droplet with a size of $D_h = 5.6$ mm, $D_b = 4.5$ mm, and $D_{eq} = 4.4$ mm is simulated at different velocities. The hollow droplet vertically impacts a flat aluminum surface with an initial temperature of 300 K. The ambient pressure is 1 atm. The ambient temperature is 300 K. The properties of fluids used in this simulation are presented in Table 3-1.

Table 3-1. Properties of water and air at T=300 K.

	Density, ρ ($\mathbf{kg/m^3}$)	**Viscosity, μ ($\mathbf{kg/m.s}$)**	**Surface Tension, σ ($\mathbf{N/m}$)**	**Thermal conductivity, k ($\mathbf{W/m.K}$)**	**Specific Heat, C_p ($\mathbf{J/kg.K}$)**
Water	998	8.9×10^{-4}	72×10^{-3}	0.6	4186
Air	1.225	1.8×10^{-5}	–	0.0242	1006.43

Due to the symmetry of the process, a 2D-axisymmetric domain was used to simulate the droplet impact on a flat surface. The computational domain and boundary conditions are shown in Figure 3-4. The behavior of a hollow droplet, including spreading and bubble ruptures, was captured in the simulations with grid numbers from 208,000 to 1,200,000. The results were validated with extracted experimental data. Compromising the accuracy and time, a structured grid with total grid numbers of 340,000 was chosen to simulate all the cases. The results for mesh independency of the solution had been reported in the previous study of the authors [107]. The size of the largest cell in the domain was 2 mm while size of the smallest cell in the domain was 0.125 mm. With the current grid distribution, near 100 cells exists inside the hollow droplet before the impact. It should be mentioned that cells were more concentrated near the symmetry axis and along the bottom boundary, the cells are fine and uniform at the impact location, and the grid distribution is constant at different time steps.

No slip boundary condition is applied on the bottom surface and pressure boundary conditions is zero gradient. Dynamic contact angle is used to simulate the liquid motion on the bottom wall. The apparent, advancing, and receding contact angle for water on aluminum surface are reported in Table 2-2. For other side of the domain, velocity boundary conditions are assumed to be zero gradient while the pressure is atmospheric pressure.

Table 2.Measured contact angles of water on different surfaces.

	Apparent contact angle	**Advancing contact angle**	**Receding contact angle**
Aluminum	85°	94°	66°

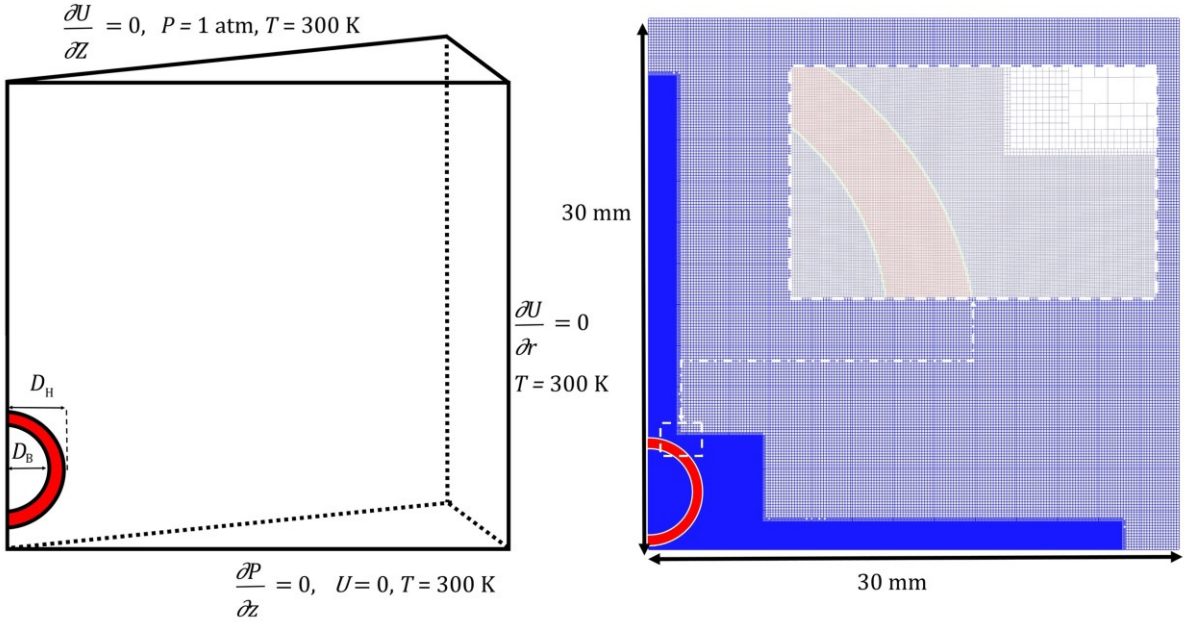

Figure 3-4. Computational domain and boundary conditions of the specified problem.

The mass, momentum, and energy equations are the governing equations to be solved to simulate hollow droplet flattening with the VOF method as,

$$\frac{\partial \rho}{\partial t} + \nabla.(\rho \vec{U}) = 0, \tag{3-3}$$

$$\frac{\partial(\rho\vec{U})}{\partial t} + \nabla.(\rho \vec{U}\vec{U}) = -\vec{\nabla}p + \rho\vec{g} + \vec{\nabla}.\left\{\mu\left[\nabla\vec{U} + (\nabla\vec{U})^T\right]\right\} + \vec{F}_{vol}. \tag{3-4}$$

$$\frac{\partial(\rho C_p T)}{\partial t} + \vec{\nabla}.(\rho C_p \vec{U} T) = \nabla.(k\nabla T) + \frac{\partial p}{\partial t} - \left(\frac{\partial \rho K}{\partial t} + \vec{\nabla}.(\rho \vec{U} K)\right). \tag{3-5}$$

where $\rho, \overrightarrow{U}$, P, $\vec{g}$, K and C_p are mixture density, velocity field, pressure, gravitational acceleration, the kinetic energy of fluid, and the specific heat, respectively. Surface tension is considered as a source term ($\vec{F}_{vol}$) and can be calculated using Brackbill method [72]. To solve momentum equations correctly, the pressure field can be calculated from the following equation [71]:

$$\left(\gamma\frac{\Psi_l}{\rho_l} + (1-\gamma)\frac{\Psi_g}{\rho_g}\right)\left[\frac{\partial p}{\partial t} + \vec{U}.\vec{\nabla}p\right] + \vec{\nabla}.\vec{U} = 0, \tag{3-6}$$

where Ψ_l, Ψ_g, ρ_l, and ρ_g are the compressibility and the density of liquid and gas, respectively. Defining compressibility as $\Psi = \partial\rho/\partial P$ based on the ideal gas equation of state, gas compressibility and liquid compressibility take the forms of,

$$\Psi_g = \frac{1}{zRT}\,, \Psi_l = \frac{1}{a^2}\,, \tag{3-7}$$

where z represents compressibility factor with the isothermal equation of state assumption. Parameter a represents sound velocity in the liquid. It should be noted that regarding the impact velocity of the hollow droplet (1 - 6 m/s), the effect of compressibility is negligible and can be ignored. Nevertheless, Regarding the main application of hollow droplets in thermal spraying in which the molten particles impact with velocity higher than 100 m/s and temperature higher than 3000 K, the effects of compressibility and heat transfer are considered in the current study to be used in the future studies of the authors.

To track the interface of two fluids, the VOF equation is used [71],

$$\frac{\partial(\gamma)}{\partial t} + \vec{\nabla}.\left(\gamma\,\vec{U}\right) = \frac{-\gamma\,\Psi_l}{\rho_l}\frac{Dp}{Dt} = \gamma(1-\gamma)\zeta + \gamma\vec{\nabla}.\left(\vec{U}\right), \tag{3-8}$$

$$\zeta = \left(\frac{\Psi_l}{\rho_l} + \frac{\Psi_g}{\rho_g}\right)\frac{Dp}{Dt}.$$

By solving the above equation, the value of γ can be obtained for each computational cell. The cell is occupied by liquid if $\gamma = 1$ whereas the cell is occupied with gas if $\gamma = 0$. Any value between $0 < \gamma < 1$ indicates that the cell contains a liquid-gas interface. Once γ has been determined, the surface tension force can be calculated as follows [72],

$$\vec{F}_{vol} = \sigma\kappa(\nabla\gamma), \qquad \kappa = -\nabla.\left(\frac{\nabla\gamma}{|\nabla\gamma|}\right), \tag{3-9}$$

where σ and κ represent the surface tension of the liquid and the surface curvature, respectively. $\nabla\gamma$ is a continuous function that is zero everywhere in the domain except for the transitional area at the interface. The mixture properties can be expressed as,

$$\mu = \gamma\mu_l + (1-\gamma)\mu_g, \tag{3-10}$$

$$\rho = \gamma\rho_l + (1-\gamma)\rho_g, \tag{3-11}$$

$$k = \gamma k_l + (1-\gamma)k_g, \tag{3-12}$$

$$c_p = \gamma c_{p,l} + (1-\gamma)c_{p,g}. \tag{3-13}$$

To optimize the computational time, an adaptive time-step control feature was applied. This controller, which keeps the solution stable, was adjusted based on the CFL number ($Co = \frac{U_i \Delta t}{\Delta x}$) at the beginning of the time iteration loop. Using the values of the velocity of the phase fractions and Δt from the previous time step, the maximum local CFL number (Co_0) was calculated, and a new time-step was iteratively initiated as,

$$\Delta t = \min\left\{\frac{Co_{max}}{Co_0}\Delta t_0;\ \left(1+\lambda_1\frac{Co_{max}}{Co_0}\right)\Delta t_0;\ \lambda_2 \Delta t_0; \Delta t_{max}\right\}, \tag{3-14}$$

where Co_{max} and Δt_{max} prescribe values for the CFL number and time step, respectively [87]. It should be noted that codes of OpenFOAM open-source software have been used to simulate the droplet flattening.

3.4 Results and discussion:

After impact, dense droplet flattens on the surface until reaching its maximum spreading diameter and then retracts toward the center (Figure 3-5.a). This retracting liquid results in an oscillating bulk of water on the surface until it stabilizes. There is no liquid detachment from the surface during the whole process.

On the contrary, the behavior of a hollow droplet impact is different (Figure 3-5.b); while a hollow droplet spreads on the surface, a counter-jet takes shape in the axial direction. This counter-jet crosses the upper shell of the entrapped bubble. When the hollow droplet reaches its maximum spreading diameter, the central counter-jet is still growing and eventually breaks up from the spreading liquid. As a result of this breakup, a portion of liquid mass detaches from the surface while the remaining liquid stabilizes and takes a semicircular shape similar to the dense droplet.

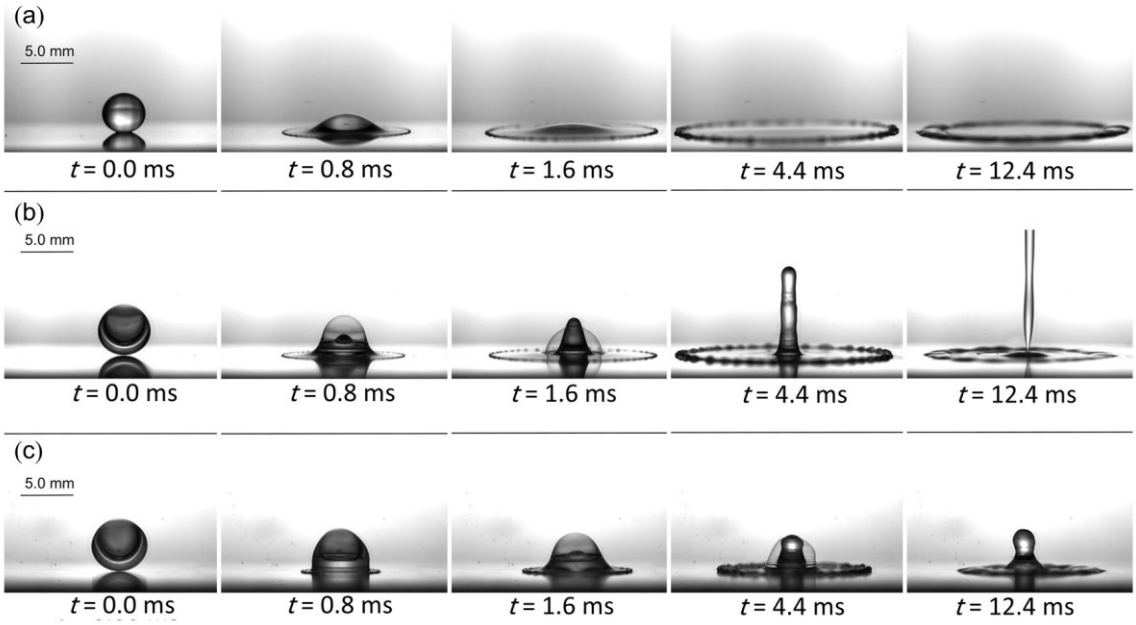

Figure 3-5. Selected snapshots show droplet impact on an aluminum surface.
(a) dense water droplet with $D_{eq} = 4.4\,mm$ impacting at $U_0 = 3.6\,m/s$ $(We = 790, Ca = 0.0016)$ (b) hollow water droplet with $D_h = 5.6\,mm, D_b = 4.5\,mm$ and $D_{eq} = 4.4\,mm$ impacting at $U_0 = 3.6\,m/s$ $(We = 790, Ca = 0.0016)$ (c) hollow water droplet with $D_h = 5.6\,mm, D_b = 4.5\,mm$ and $D_{eq} = 4.4\,mm$ impacting at $U_0 = 1.0\,m/s$ $(We = 60,, Ca = 0.0016)$.

When a dense droplet impacts a surface, the pressure of the liquid at the contact point increases. This high pressure gradually decreases inside the droplet. The liquid located at this high-pressure region intended to move to regions with lower pressure. Nevertheless, the liquid cannot recoil and move upward because of the pressure gradient inside the droplet. Therefore, the liquid can only spread in the radial direction and consequently, the dense droplet flattens on the surface. As a result, the kinetic and surface energies of droplet before impact convert to the surface energy of the spreading droplet and dissipate through viscosity. The equilibrium between these energies determines the spreading diameter of the droplet [107].

However, when a hollow droplet impacts a surface, the same high-pressure region at the impact location can be observed. The only difference is that this high-pressure region does not gradually decrease inside the droplet. Instead, there is a pressure gap between the high-pressure region of the droplet with the upper half of the droplet. This pressure gap allows the pressurized liquid to move upward in addition to spreading on the surface. Thereupon, a counter-jet forms on the surface as the hollow droplet flattens. Considering the equilibrium between the energy before and after impact, the spreading portion of the hollow droplet has less energy to spread on the surface compared to the dense droplet. Therefore, a smaller spreading diameter is

observed for the hollow droplet in comparison to the dense droplet. It should be noted that as a result of the impact, the pressure inside the bubble increases [107].

Many parameters affect the behavior of a hollow droplet after impact on the surface, including droplet velocity (Figure 3-5.c), type of the liquid, size, and location of the entrapped bubble. For instance, at hollow droplet impact with low velocity or high viscosity, which can be distinguished as low Re number, the spreading diameter of the hollow droplet is lower than hollow droplet impact at high Re numbers. This is due to lower kinetic energy, which can be dissipated by a higher ratio of viscous force, surface tension and gravitation force. The other difference is about the formation of the counter-jet. Even though the counter-jet forms even at impacts with low Re numbers, the length of counter-jet is small, there is no detachment, and the counter-jet returns to the spreading portion of the liquid. Therefore, the effects of these parameters on the behavior of the hollow droplet are studied through a detailed numerical investigation. Figure 3-6 shows snapshots of the simulation of a hollow droplet impacting on a surface with $U_0 = 3.6\ \mathrm{m/s}$. As it can be seen, the flattening behavior of the hollow droplet predicted by the numerical simulation is similar to the captured experimental photos. The only difference is the fingering phenomenon in the experimental images, which was not captured due to the 2D-axisymmetric assumption in the numerical simulations.

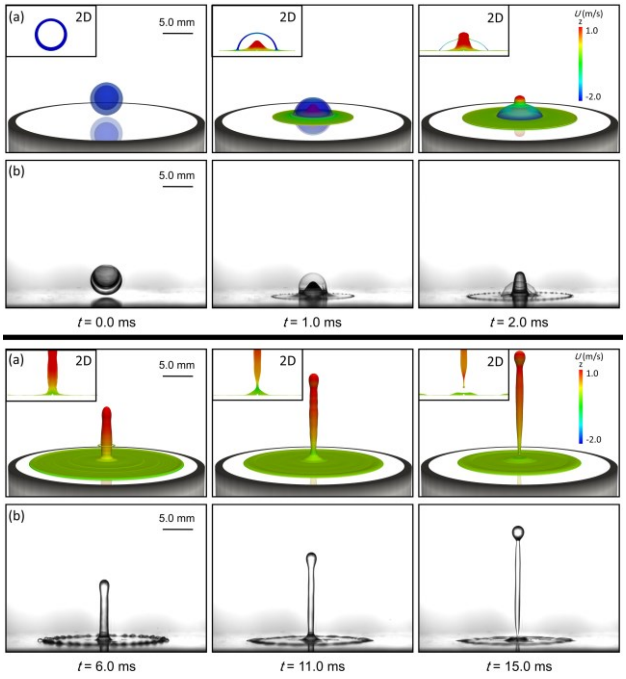

Figure 3-6. Selected snapshots of experimental images and numerical simulation for a hollow water droplet. $D_h = 5.6\ mm, D_b = 4.5\ mm, D_{eq} = 4.4\ mm$ impacting on an aluminum surface at $U_0 = 3.6\ m/s$. The experimental images are shown to be compared with the results of the numerical simulation.

Moreover, two critical parameters obtained by the numerical simulation, i.e., the spreading diameter and the counter-jet height of the hollow droplet after impact, are compared with the measured experimental data in Figure 3-7. As it is shown, the numerical results are in good agreement with the experimental data at different velocities.

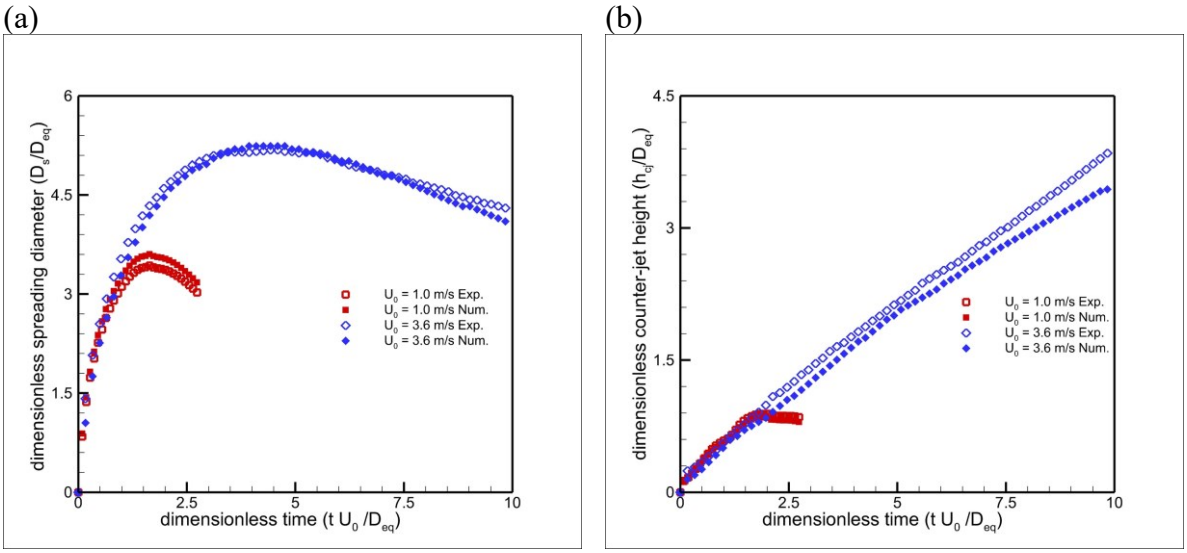

Figure 3-7. Characteristics of a hollow droplet with $D_h = 5.6\ mm$, $D_b = 4.5\ mm$ and $D_{eq} = 4.4\ mm$ and $Ca = 0.0016$ impacting at different velocities.

(a) spreading diameter ($D_s^* = D_s/D_{eq}$) versus time ($t^* = t\ U_0/D_{eq}$) (b) counter-jet height ($h_{cj}^* = h_{cj}/D_{eq}$) versus time.

3.4.1 Hollow droplet impact at different velocities

Figure 3-8 shows snapshots of the numerical simulations of the hollow droplet at different velocities. The spreading and the counter-jet formation is captured in all different velocities. By increasing the impact velocity, the length of the counter-jet becomes longer while its width gets thinner. In addition, the spreading diameter is increased by the impact velocity of the hollow droplet.

The characteristics of the hollow droplet impingement on a surface are demonstrated in Figure 3-9 and Figure 3-10. Dimensionless numbers are defined to provide more comprehensive information. Figure 3-9.a shows the dimensionless spreading diameter ($D_s^* = D_s/D_{eq}$) of hollow droplet during dimensionless time ($t^* = t\ U_0/D_{eq}$) at different impact velocities. The droplet spreading increases with droplet impact velocity (U_0) until it reaches its maximum value, then recoils and forms a semicircular shape.

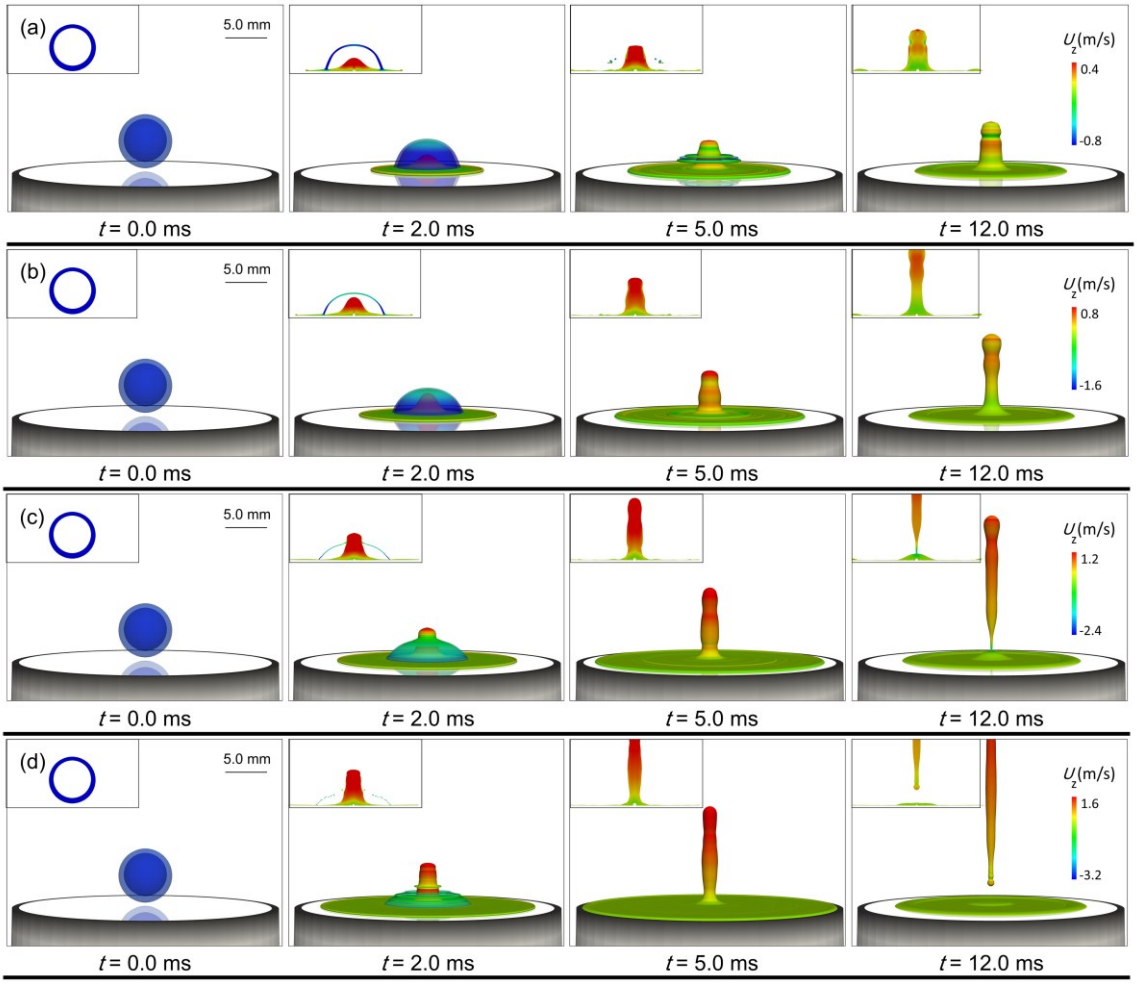

Figure 3-8. Selected snapshots of numerical simulation of a hollow water droplet with $D_h = 5.6\ mm,\ D_b = 4.5\ mm,\ D_{eq} = 4.4\ mm$ and $Ca = 0.0016$ impacting a surface at different velocities.
(a) $U_0 = 1.8\ m/s\ \ (We = 198)$ (b) $U_0 = 2.4\ m/s\ \ (We = 350)$ (c) $U_0 = 3.6\ m/s\ \ (We = 790)$ (d) $U_0 = 4.8\ m/s\ (We = 1410)$

The dimensionless counter-jet height $(h_{cj}^* = h_{cj}/D_{eq})$ against dimensionless time is demonstrated in Figure 3-9,b. The height of the counter-jet grows until it reaches a maximum value and then starts to fall at low impact velocities. However, the height of the counter-jet increases permanently until it detaches from the surface at high impact velocities. The slope of counter-jet height against time at different droplet impact velocities is shown here. Clearly, a similar slope at different impact velocities can be observed, especially at initial instances of the counter-jet formation. Then, the slope decreases, resulting from dissipation of energy during counter-jet formation and progress. The decrement is more evident at low impact velocities, while the slope is almost linear during counter-jet progress, especially at high impact velocities.

(a) (b)

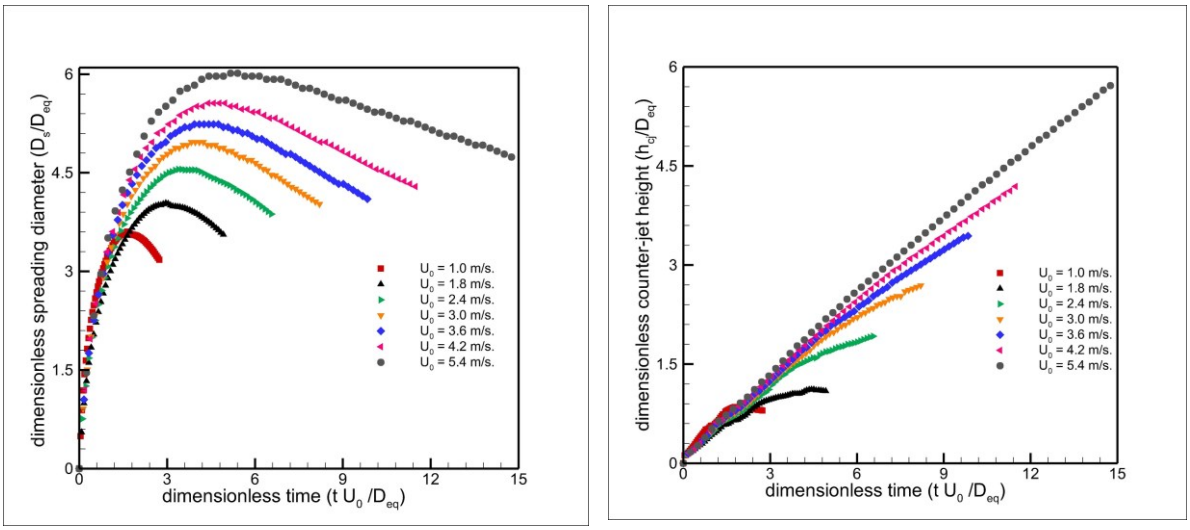

Figure 3-9. Characteristics of a hollow droplet with $D_h = 5.6\ mm$, $D_b = 4.5\ mm$ and $D_{eq} = 4.4\ mm$ and $Ca = 0.0016$ impacting at different velocities.

(a) spreading diameter ($D_s^* = D_s/D_{eq}$) versus time ($t^* = t\ U_0/D_{eq}$), (b) counter-jet height ($h_{cj}^* = h_{cj}/D_{eq}$) versus time.

Figure 3-10.a shows the dimensionless counter-jet velocity ($U_{cj}^* = U_{cj}/U_0$) against dimensionless time (t^*) at different impact velocities. At the impact of the hollow droplet on the surface, a counter-jet forms, which moves perpendicular to the surface. The velocity of the counter-jet increases with progress in time. This increment continues until a maximum velocity decreases and reaches almost a constant value. The maximum velocity point occurs before the penetration of the counter-jet into the upper shell of the entrapped bubble (Figure 3-11). At low Re number, the counter-jet retracts toward the surface after reaching a peak which is shown by negative velocity in Figure 3-10.a. However, at high Re number, the counter-jet develops with a constant velocity ($U_{cj}^* = 0.4$) until it detaches from the surface.

The dimensionless volume of the counter-jet ($V_{cj}^* = V_{cj}/[\alpha\beta\ V_{eq}]$) at the maximum spreading time is demonstrated in Figure 3-10.b for different velocities. This volume includes the liquid pillar from the surface which has a positive velocity in the Z direction. As it can be seen, the volume of the counter-jet is almost $V_{cj} = 0.3\ \alpha\beta\ V_{eq}$ at the maximum spreading, no matter of the hollow droplet impact velocity.

(a) (b)

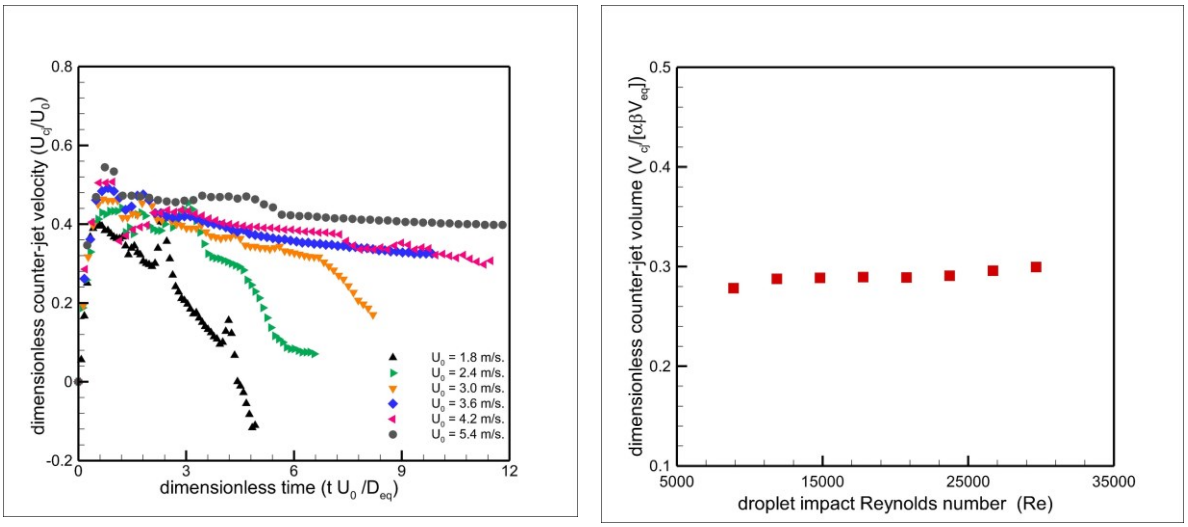

Figure 3-10. Characteristics of hollow droplet $D_h = 5.6\ mm, D_b = 4.5\ mm$ and $D_{eq} = 4.4\ mm$ impacting at different velocities.

(a) the velocity of the counter-jet ($U^*_{cj} = U_{cj}/U_0$) versus time ($t^* = t\ U_0/D_{eq}$) (b) counter-jet volume ($V^*_{cj} = V_{cj}/[\alpha\beta\ V_{eq}]$) versus droplet impact Reynolds number.

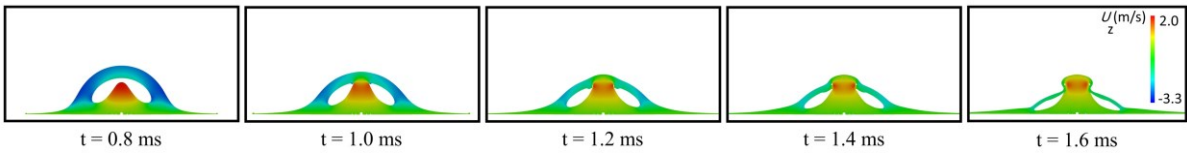

Figure 3-11. snapshots of the counter-jet penetration into the upper shell of the bubble for a hollow droplet with $D_H = 5.6\ mm$ and $D_B = 2.8\ mm$ impacting at at $Re = 17760$ and $We = 790$ (corresponding to $U = 3.6\ m/s$)

3.4.2 Bubble size

The other parameter that affects the hollow droplet impact characteristics is the size of the entrapped bubble. Figure 3-12 shows snapshots of hollow droplets impact with different bubble sizes. The formation of the counter-jet is the same for all droplets. Nevertheless, the counter-jet shape is different. As the size of entrapped bubble increases, the size of the counter-jet grows. In addition, there are oscillations on the counter-jet's surface for hollow droplets with small trapped bubbles, leading to faster breakup and detachment of the counter-jet from the surface compared to hollow droplets with larger bubbles.

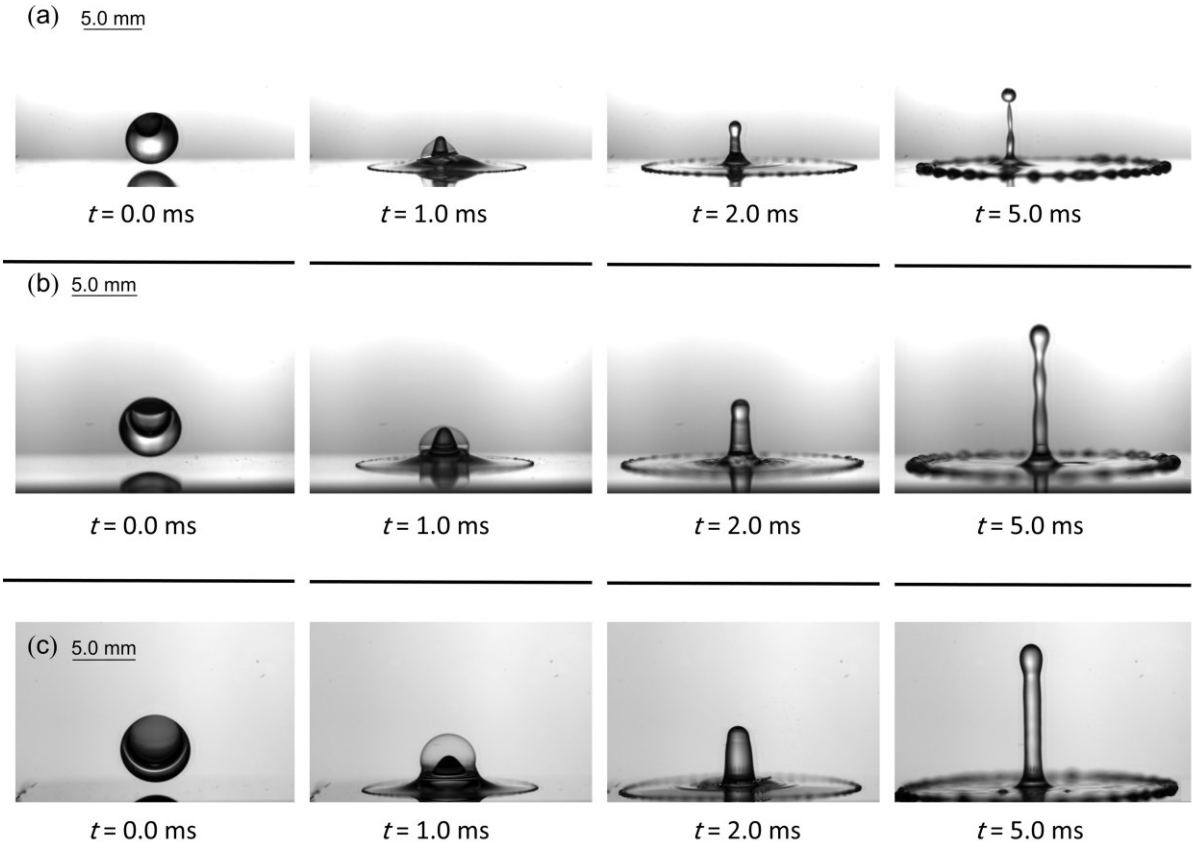

Figure 3-12. Selected snapshots showing hollow droplet impact at $U_0 = 3.6\frac{m}{s}$ and $D_{eq} = 4.54\ mm$ ($We = 790, Ca = 0.0016$) with different bubble sizes.
(a) $D_h = 4.6\ mm, D_b = 0.96\ mm$, (b) $D_h = 4.84\ mm, D_b = 2.7\ mm$, and (c) $D_h = 5.4\ mm, D_b = 4.0\ mm$.

In order to have an accurate comparison between hollow droplet impacts with different bubble sizes, numerical simulations are performed on hollow droplets with a diameter of $D_h = 5.6$ mm and different bubble sizes impacting on a surface with velocity $U_0 = 3.6$ m/s. Hollow droplets with constant outer diameter ($D_h = 5.6$ mm) and different bubble sizes (D_b) are considered where the hollowness ratio (β/α) varies from 0.25 to 0.85. Snapshots of numerical results for hollow droplet impact with different bubble locations are presented in Appendix A.

Generally, hollow droplets with different bubble sizes have similar behavior after impact on the surface. As the size of the entrapped bubble decreases, the maximum spreading diameter of the hollow droplet increases due to higher mass of the droplet, which impacts the surface (Figure 3-13.a). It should be mentioned that in Figure 3-13.a, spreading diameter is non-dimensional using an equivalent diameter of each specific droplet and can be calculated by equation (3-2). The other parameter which is influenced by the size of the bubble is the counter-jet height. As it is shown in Figure 3-13,b, the height of the counter-jet increases by time with a similar slope for all hollow droplets except for hollow droplets with hollowness ratio

parameter $\beta/\alpha < 0.35$. This is due to the higher thickness of the bubble shell for low hollowness ratio droplets, which reduces counter-jet energy during passing through the upper shell of the bubble. Nevertheless, the maximum height of the counter-jet at each time does not belong to the hollow droplet with the smallest or largest bubble. There is an optimum value for the size of the bubble, which leads to the highest counter-jet length, which is ($D_h = 4.0$ mm) and can be calculated for any hollow droplet with the optimized hollowness ratio parameter $(\beta/\alpha)^* = 0.71$.

(a) (b)

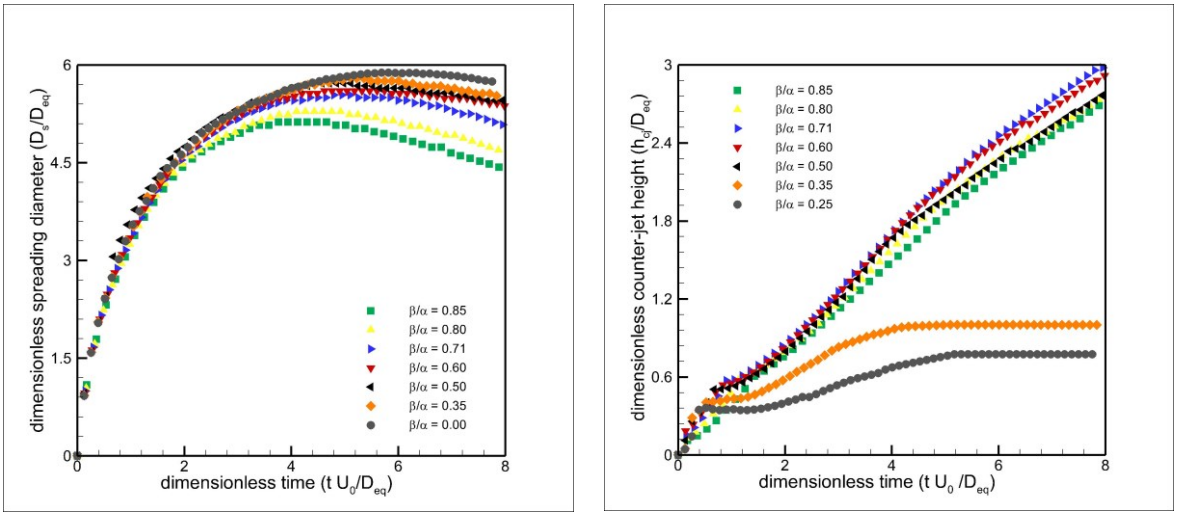

Figure 3-13. The spreading characteristics of a hollow droplet $D_h = 5.6\ mm$ $(Ca = 0.0016)$ with different bubble sizes impacting on a surface at $U_0 = 3.6\frac{m}{s}$.

(a) spreading diameter $(D_s^* = D_s/D_{eq})$ versus time $(t^* = t\ U_0/D_{eq})$ (b) counter-jet height $(h_{cj}^* = h_{cj}/D_{eq})$ versus time.

Figure 3-14.a shows the dimensionless velocity of the counter-jet during the dimensionless time. The trend of the counter-jet velocity is similar to what had been seen in Figure 3-10.a. After formation, the counter-jet velocity increases until it reaches the upper shell of the bubble. For hollow droplets with $\beta/\alpha > 0.35$, the counter-jet passes through this shell and loses a portion of its kinetic energy and continues with an average velocity of $(U_{cj}^* = 0.4)$. This value is less for hollow droplets with $\beta/\alpha < 0.35$, which justifies lower slopes of the counter-jet heights of these droplets in Figure 3-13.b. The other issue is the counter-jet level falling after the first peak. It is shown that as the hollowness ratio (β/α) increases, the minimum point decreases and for the hollow droplets with highest hollowness ration (β/α), the minimum point peak is vanished.

The counter-jet velocity shows two picks during counter-jet evolution. The first picks occurs when the counter-jet penetrates the bubble and reaches upper shell of the bubble. At this point, the liquid in the upper portion of the hollow droplet damps the counter-jet motion and reduces the counter-jet velocity. This pick has been observed in all cases and it is more severe in case with low hollowness ratio, as the counter-jet has to pass a thicker shell.

(a) (b)

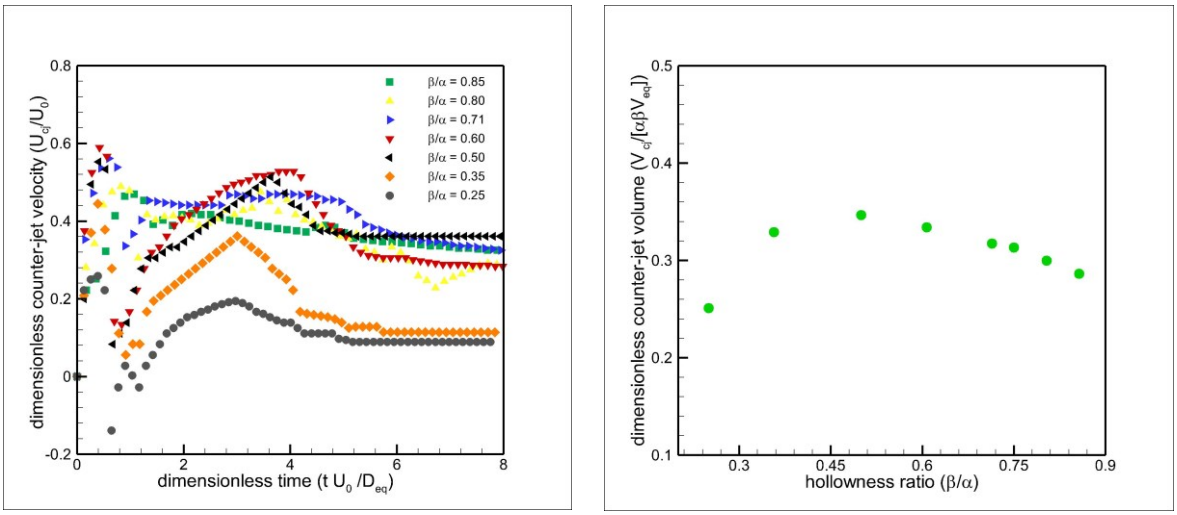

Figure 3-14. The spreading characteristics of a hollow droplet $D_h = 5.6\ mm$ $(Ca = 0.0016)$ with different bubble sizes impacting on the surface at $U_0 = 3.6\ m/s$.
(a) Velocity of the counter-jet $(U^*_{cj} = U_{cj}/U_0)$ versus time $(t^* = t\ U_0/D_{eq})$ (b) counter-jet volume $(Vol^*_{cj} = Vol_{cj}/[\alpha\beta\ Vol_{eq}])$ versus hollowness ratio.

However, there is a second pick that only has been seen in cases with lower hollowness ratio. This pick can be due to the liquid portion which is still falling after the bubble collapse or because of bubble rupture which induces velocity to counter-jet. In the case of hollow droplets with low hollowness (thicker bubble shell), when the bubble ruptures, the liquid shell moves fast toward the substrate as a ligament and joins the flattening liquid. This liquid mass increases the counter-jet velocity again until a point that the gravity decelerates the counter-jet. As the hollowness ratio increases, the bubble shell becomes thinner. In droplets with high hollowness ratio, the bubble explodes, and thin liquid shell disperse around it which cannot significantly change the counter-jet velocity.

The dimensionless counter-jet volume at the maximum spreading time is demonstrated in Figure 3-14.b. The size of the entrapped bubble can affect the shape, and the volume of the counter-jet at it was reported in Figure 3-12. Nevertheless, the dimensionless volume of the counter-jet is in the range of $0.26 < Vol^*_{cj} < 0.34$. This variation decreases for hollow droplets

with high hollowness ratio and reaches a constant value of $Vol_{cj}^{*} = 0.3$ or $Vol_{cj} = 0.3\ \alpha\beta\ Vol_{eq}$.

Plasma spraying is one of the main applications of hollow droplets due to the possibility of producing coatings with higher porosity. This increased porosity is a result of increased roughness on the solidified splats. Hence the effect of bubble size on the roughness of the splat at maximum spreading is demonstrated in Figure 3-15. In addition to differences in the shape of the counter-jet and the spreading diameter of hollow droplets with different bubble sizes, which can be seen in Figure 14, the splat surface roughness is the another parameter that can distinguish the effect of bubble size (Figure 3-15.b). As can be seen, droplets with a higher hollowness ratio have a rougher surface than the hollow droplets with a lower hollowness ratio. This is due to a thinner bubble shell of hollow droplets with a high hollowness ratio which can be affected by the bubble explosion that induces more strong perturbations to the surface of the splat. The other issue that is importanct to note is that when a droplet impacts a surface, a small portion of air entraps underneath the droplet that cannot be washed off by the liquid inertia due to axisymmetric definition of the problem [108].

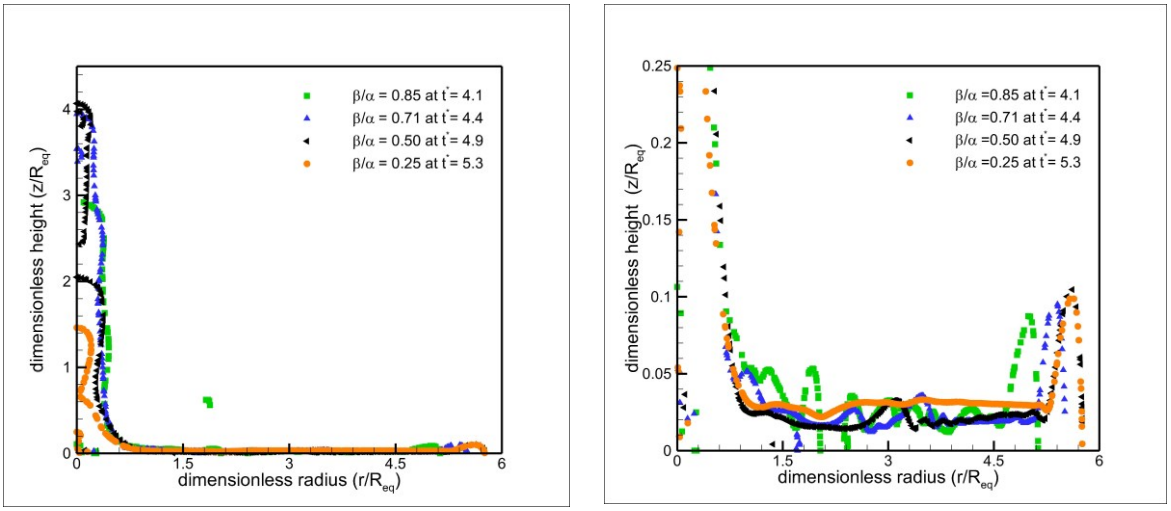

Figure 3-15. Counter-jet height versus spreading radius of a hollow droplet $D_h = 5.6\ mm$ $(Ca = 0.0016)$ with different bubble sizes impacting on a surface at $U_0 = 3.6\ m/s$ at maximum spreading time.

3.4.3 Bubble location

The location of the entrapped bubble inside the hollow droplet plays some role in the outcome of the droplet impact as demonstrated in Figure 3-16.

Four different cases are numerically simulated to investigate the effect of bubble location accurately (Figure 3-17). In the first case, the bubble is located at the center, and in the last one,

it is located at the top. The dimensionless parameter $\delta^* = \delta/D_{eq}$ shows the location of the bubble inside the hollow droplet in which δ is the distance between the center of the bubble and the center of the droplet. In this figure, the size of the hollow droplet (D_h) and bubble (D_b) are the same for all four cases. Snapshots of numerical results for hollow droplet impact with different bubble locations are presented in Appendix B.

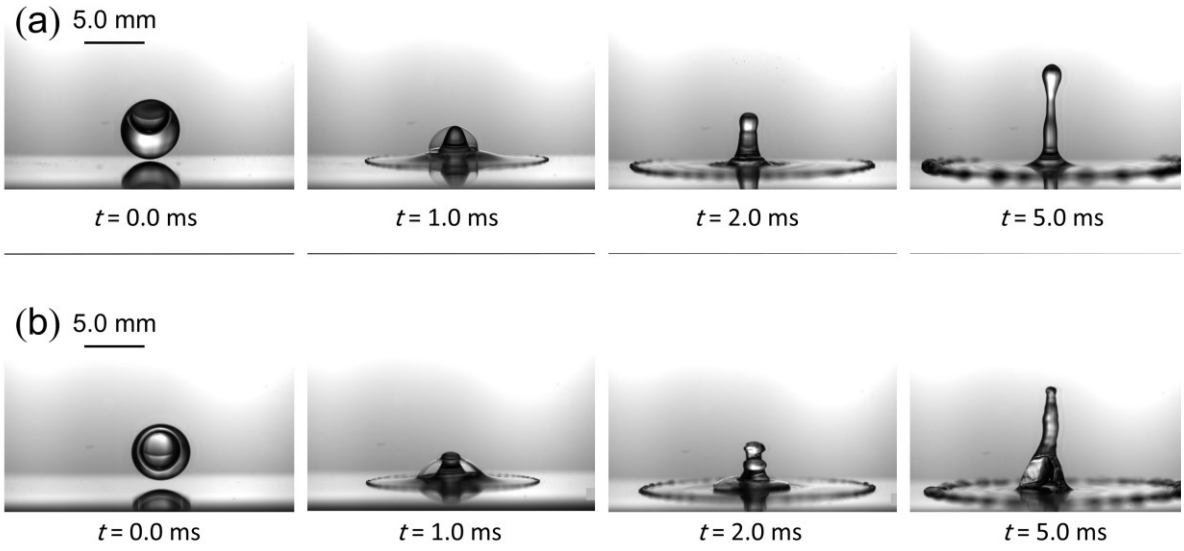

Figure 3-16. Selected snapshots showing the spread of a hollow water droplet with different bubble locations impact at $U_0 = 3.6\ m/s$ with
(a) $D_h = 4.8\ mm, D_b = 3.1\ mm$ and $D_{eq} = 4.3\ mm$, $\delta^* = 0.14$(b) $D_h = 4.92\ mm, D_b = 3.44\ mm$ and $D_{eq} = 4.4\ mm, \delta^* = 0.0$

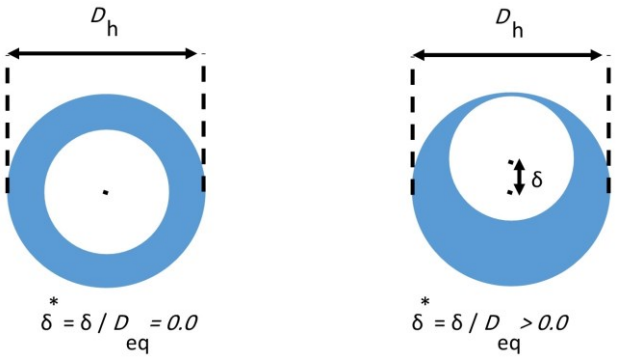

Figure 3-17. Geometrical representation of the bubble location inside a hollow droplet.

Figure 3-18 shows characteristics of hollow droplets after impact on the surface. As it is shown, the spreading diameter of all four cases is almost the same (Figure 3-18.a). It is shown that the hollow droplet with a bubble located on the center slightly has a higher maximum spreading diameter. The behavior of the hollow droplet is reversed in the case of counter-jet height (Figure 3-18,b). Even though the slope of counter-jet height against time is almost equal for all cases, but this slope is slightly higher for the bubble located on the top.

(a) (b)

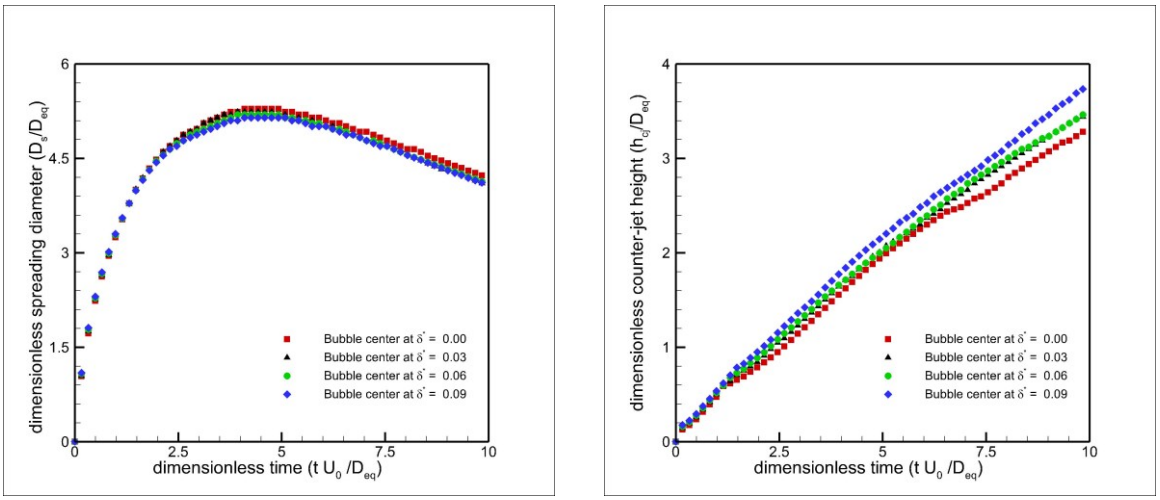

Figure 3-18. Characteristics of a hollow droplet ($D_h = 5.6\,mm$and $D_b = 4.5\,mm$) with different bubble locations impacting on a surface with $U_0 = 3.6\,m/s$ ($We = 790, Ca = 0.0016$).
(a) spreading diameter ($D_s^* = D_s/D_{eq}$) versus time ($t^* = t\,U_0/D_{eq}$) (b) counter-jet height (h_{cj}^*) versus time.

The effect of bubble location is more obvious on the smoothness of the formed splat at the maximum spreading time. As shown in Figure 3-19, the hollow droplet with the bubble located at the center has higher roughness than the hollow droplets with the bubble on the top. It is probably due to the higher thickness of the upper bubble shell when the droplet is located at the center. When the counter-jet forms and passes through the upper shell and then ruptures it, the thicker bubble shell transfers more oscillations to the splat's surface, making its surface rougher.

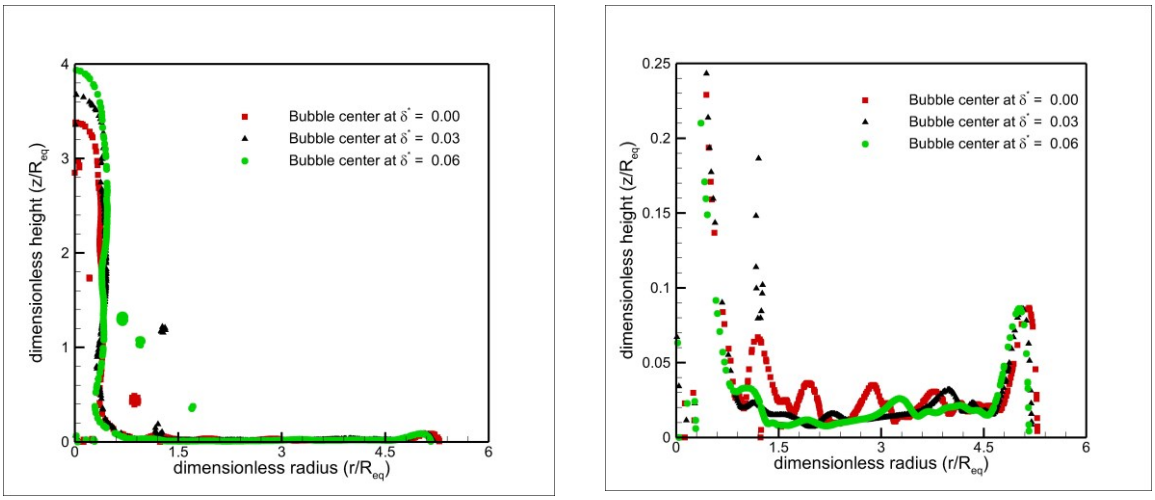

Figure 3-19. counter-jet height versus spreading radius for a hollow droplet $D_h = 5.6\,mm$and $D_b = 4.5\,mm$ with different bubble locations impacting on the surface with $U_0 = 3.6\,m/s$ ($We = 790, Ca = 0.0016$) at maximum spreading time.

Due to 2D axisymmetric numerical simulations, it is assumed that the bubble is located on the vertical centerline of the hollow droplet. However, during experimental studies, it was observed that any small deviation in the bubble's location from the center of the droplet affects the location of the counter-jet, as shown in Figure 3-20.

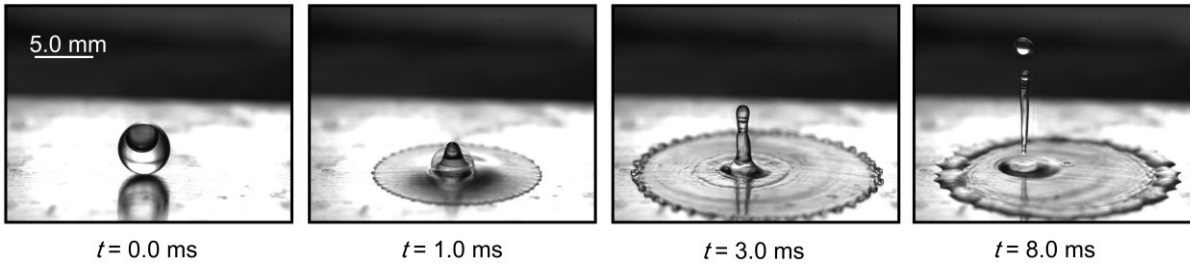

Figure 3-20. The impingement of a hollow water droplet with $D_h = 4.8\,mm, D_b = 3.2\,mm$ and $D_{eq} = 4.15\,mm$ on an aluminum surface at $U_0 = 3.6\,m/s$.

3.4.4 Theoretical analysis

In characterizing the hollow droplet impact, a void water sphere with a diameter of D_h is considered in which the diameter of the entrapped bubble is D_b. The mass of this hollow droplet is equal to the mass of a dense droplet with a diameter of D_{eq}. After impact, the hollow droplet divides into two portions. One portion spread on the surface in the shape of a flat cylinder with a diameter of D and height of h, while the other portion forms a counter-jet in the shape of a vertical cylinder with a diameter of D_{cj} and height of h_{cj}. It is assumed that no splashing occurs, and the edge effects associated with the rim formation are negligible. The droplets are considered large enough that the capillary length could be neglected. (i.e., $\rho g D_{eq}^2 / \gamma \approx 1$). Therefore, the effect of gravity is neglected, and the only contribution to the potential energy of the drop arises from the surface tension [109]. In addition, as impact velocity increases, droplet kinetic energy will be much larger than surface energy (i.e., $We \gg 1$), and surface tension and contact angle effects will eventually become negligible [9].

Before impact, the effective energies of the hollow droplet are kinetic energy (KE_1) and surface energy (SE_1) and the energy conservation equation of a hollow droplet can be written as,

$$KE_1 + SE_1 + GE_1 = KE_{2s} + SE_{2s} + GE_{2s} + W + KE_{2cj} + SE_{2cj} + GE_{2cj}. \quad (3\text{-}15)$$

Considering the hollow droplet exactly before the impact, the center of droplet is located at $h_D = \frac{D_{eq}}{2}$. Assuming a constant surface tension, the energy values on the left side are given by,

$$KE_1 = \left(\frac{1}{2}\,\rho\, U_0^2\right)\left(\frac{\pi}{6}D_{eq}^3\right), \tag{3-16}$$

$$SE_1 = \pi D_h^2 Y + \pi D_b^2 Y = \pi\alpha^2 D_{eq}^2 Y + \pi\beta^2 D_{eq}^2 Y = \pi D_{eq}^2 Y(\alpha^2+\beta^2). \tag{3-17}$$

$$GE_1 = (\rho g h_D)\left(\frac{\pi}{6}D_{eq}^3\right) = \left(\rho g \frac{D_{eq}}{2}\right)\left(\frac{\pi}{6}D_{eq}^3\right) \tag{3-18}$$

After the hollow droplet impact, a portion of the droplet spreads, and the other portion forms a counter-jet. When the spreading part reaches the maximum spreading diameter, its kinetic energy is zero. The gravitational energy is also negligible and assumed to be zero. The only effective energy is the splat surface energy. The surface energy can be calculated by,

$$GE_{2s} = 0, \tag{3-19}$$

$$KE_{2s} = 0, \tag{3-20}$$

$$SE_{2S} = \frac{\pi}{4}D_{max}^2 Y(1-cos\eta_a), \tag{3-21}$$

where θ_a is advancing contact angle [9]. In addition, the work done by viscous force can be calculated by,

$$W = \int_0^{t_c}\int_0^{v} \phi\, d\Omega\, t_s, \tag{3-22}$$

where Ω is the volume of viscous fluid, t_c is time for the droplet to reach maximum spreading, and ϕ is viscous dissipation function which is estimated by,

$$\phi \sim \mu\left(\frac{U_0}{L}\right)^2. \tag{3-23}$$

Here, μ is liquid viscosity, and L is characteristic length estimated by the boundary layer thickness (δ) at a solid-liquid interface.

The time required for the hollow droplet to reach the maximum spreading diameter can be estimated by assuming the outcome of the hollow droplet impact into two different parts, one is a cylindrical disk with the diameter of D and thickness of h responsible for the droplet spreading, and the other one is a cylinder with a diameter of D_{cj} and height of h_{cj} responsible for counter-jet formation (Figure 3-3). Liquid flows from the droplet into the film and counter-

jet through an area of diameter d with velocity U_0. The velocity at the edge of the splat during spreading (U_R) is given by the conservation of mass law,

$$U_0 \frac{\pi d^2}{4} = U_R \pi D h + U_{cj} \frac{\pi {D_{cj}}^2}{4}. \tag{3-24}$$

Based on Figure 3-10 and Figure 3-14, velocity (U_{cj}), diameter (D_{cj}) and volume (V_{cj}) associated to the counter-jet are estimated as $U_{cj} \simeq 0.4\, U_0$, $D_{cj} \simeq 0.5\, D_b$ while $D_b = \beta D_{eq}$ and $V_{cj} \simeq 0.3\alpha\beta\, V_{eq}$).

The splat thickness (h) after impact can be calculated by equating the volume of hollow droplet before impact (V_h), the volume of the spreading liquid (V_{sp}) in the shape of a disk with height h and diameter D_{max}, and the volume of counter-jet (V_{cj}) as a cylinder with a height of h_{cj} and diameter of D_{cj},

$$V_h = V_{sp} + V_{cj}, \tag{3-25}$$

$$\frac{4\pi}{3} \times \frac{D_{eq}^3}{8} = \frac{\pi\, D_{max}^2 h}{4} + (0.3\alpha\beta) \times \left(\frac{4\pi}{3} \times \frac{D_{eq}^3}{8} \right), \tag{3-26}$$

$$h = (1 - 0.3\alpha\beta) \times \frac{2}{3} \times \frac{D_{eq}^3}{D_{max}^2}. \tag{3-27}$$

Since d varies between 0 and D_{eq}, an average value is assumed for $d \sim D_{eq}/2$. Substituting h from equation (3-27) and d parameter into equation (3-24) results in,

$$\frac{dD}{dt} = 2U_R = \frac{3}{32} \frac{D_{max}^2\, U_0}{D_{eq}} \left(\frac{1 - 0.4\, \beta^2}{1 - 0.3\alpha\beta} \right), \tag{3-28}$$

$$\frac{D^2}{D_{max}^2} = \frac{3}{8} \frac{U_0}{D_{eq}} \left(\frac{1 - 0.4\, \beta^2}{1 - 0.3\alpha\beta} \right) t_{sp}. \tag{3-29}$$

At maximum spreading condition $D = D_{max}$, therefore,

$$t_{sp} = \frac{8}{3} \frac{D_{eq}}{U_0} \left(\frac{1 - 0.3\alpha\beta}{1 - 0.4\, \beta^2} \right). \tag{3-30}$$

In addition, the volume of viscous fluid can be calculated by,

$$\Omega = \frac{\pi\, D_{max}^2\, \delta}{4}. \tag{3-31}$$

Pasandideh-Fard et al. [9] calculated the boundary layer thickness of a dense liquid droplet after impact on a surface as,

$$\delta = 2\left(\frac{D_{eq}}{\sqrt{Re}}\right). \tag{3-32}$$

Similarly, considering the assumption $V_{cj} \simeq 0.3\alpha\beta\ V_{eq}$, the volume of the liquid spreading on the surface is $(1 - 0.3\alpha\beta)\ V_{eq}$ and the boundary layer for the hollow droplet thickness can be written as,

$$\delta = 2\left(\frac{\sqrt{(1 - 0.3\alpha\beta)} \times D_{eq}}{\sqrt{Re}}\right), \tag{3-33}$$

in which the Reynolds number is defined as $Re = \rho U_0 D_{eq}/\mu$. Substituting equations (3-23), (3-27), (3-30), (3-31), (3-32) into equation (3-22) yields,

$$W = \frac{\pi}{3}\ \rho\ U_0^2 D_{eq}\ D_{max}^2 \frac{1}{\sqrt{(1 - 0.3\alpha\beta) \times Re}}\left(\frac{1 - 0.3\alpha\beta}{1 - 0.4\ \beta^2}\right). \tag{3-34}$$

Kinetic energy of the counter-jet at maximum spreading time can be calculated as,

$$KE_{2cj} = \frac{1}{2}\ \rho\ V_{cj} U_{cj}^2. \tag{3-35}$$

Considering $U_{cj} \simeq 0.4\ U_0$ and $V_{cj} \simeq 0.3\alpha\beta\ V_{eq}$ (Figure 3-10 and Figure 3-14) one can obtain,

$$KE_{2cj} = \frac{1}{2}\ \rho\ (0.4 \times U_0)^2 \left(\frac{\pi}{6} \times D_{eq}^3\right) \times (0.3\alpha\beta\ ). \tag{3-36}$$

On the other hand, the counter-jet surface energy can be calculated by considering the counter-jet in the shape of a cylinder with a semi-sphere on the top,

$$SE_{2cj} = SE_{2cj1} + SE_{2cj2}, \tag{3-37}$$

$$SE_{2cj} = \frac{\pi}{4} D_{cj}^2\ \Upsilon + \pi D_{cj} h_{cj}\ \Upsilon. \tag{3-38}$$

Assuming $U_{cj} = 0.4\ U_0$, $D_{cj} \simeq 0.5\ D_b$, $D_b = \beta D_{eq}$ and $V_{cj} = 0.3\alpha\beta\ V_{eq}$, hence $h_{cj} \simeq 0.8\ \frac{\alpha}{\beta} D_{eq}$ and,

$$SE_{2cj} = \frac{\pi}{2} D_{cj}^2\ \Upsilon + \pi D_{cj} h_{cj}\ \Upsilon, \tag{3-39}$$

$$SE_{2cj} = \pi \Upsilon D_{eq}^2 \left[\frac{\beta^2}{8} + 0.4\alpha\right]. \tag{3-40}$$

Gravitational energy of the counter-jet at maximum spreading time can be calculated as,

$$GE_{2cj} = \rho V_{cj} g \frac{h_{cj}}{2}. \tag{3-41}$$

Assuming $D_{cj} \simeq 0.5\, D_b$, $D_b = \beta D_{eq}$ and $V_{cj} = 0.3\alpha\beta\, V_{eq}$, hence $h_{cj} \simeq 0.8\, \frac{\alpha}{\beta} D_{eq}$ and

$$GE_{2cj} = = (\rho g)\left(0.3\alpha\beta * \frac{\pi}{6} D_{eq}^3\right)\left(0.4\, \frac{\alpha}{\beta} D_{eq}\right) \tag{3-42}$$

Substituting equations (2-16), (2-17), (2-18), (2-19), (3-16), (3-17), (3-20), (3-21), (3-22), (3-36), (3-40) into equation (3-15) and noting that $\alpha = \sqrt[3]{1+\beta^3}$ (equation (3-2)), one obtains

$$\frac{D_{max}}{D_{eq}} = \sqrt{\frac{M\, We + 12N + Q\, Bo}{3(1 - cos\theta_a) + 4\frac{We}{\sqrt{Re}} \times I}}. \tag{3-43}$$

in which *M, N* and *I* are defined as,

$$M = \left(1 - 0.048\beta \sqrt[3]{1+\beta^3}\right), \tag{3-44}$$

$$N = \sqrt[3]{(1+\beta^3)^2} + \beta^2 - \frac{\beta^2}{8} - 0.4\sqrt[3]{1+\beta^3}, \tag{3-45}$$

$$I = \frac{\sqrt{(1 - 0.3\beta \sqrt[3]{1+\beta^3})}}{(1 - 0.4\beta^2)}. \tag{3-46}$$

$$Q = \left(1 - 0.24\, \sqrt[3]{(1+\beta^3)^2}\right). \tag{3-47}$$

The accuracy of the predicted maximum spreading from equation (3-43) was tested by comparison with experimental and numerical measurements for a variety of hollow droplets impacting a surface in a wide range of Weber and Reynolds numbers.

The results of theoretical prediction for hollow droplet flattening are compared with numerical data in Figure 3-21.

(a) (b)

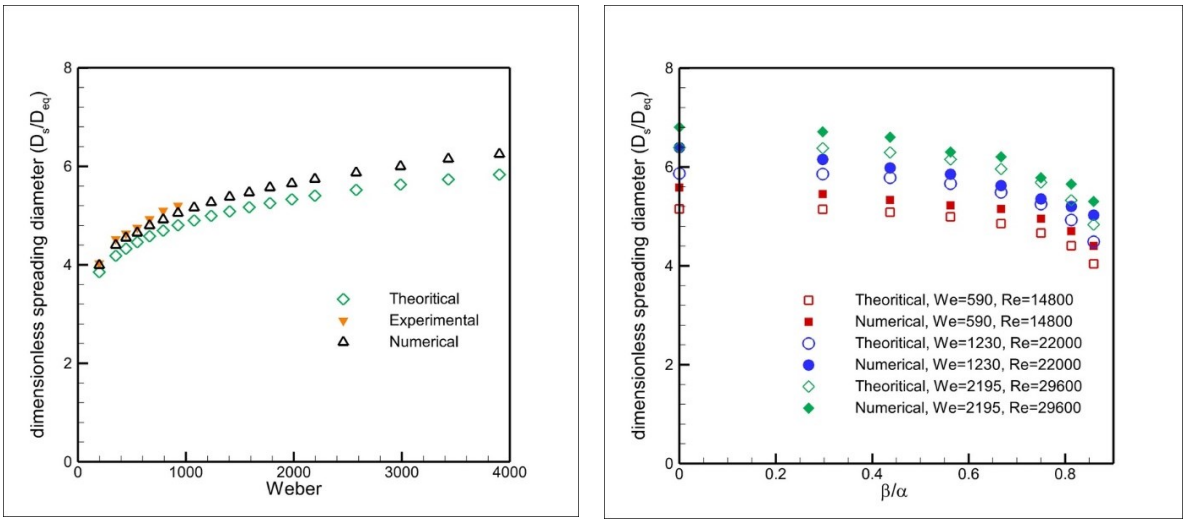

Figure 3-21. Theoretical prediction of maximum spreading diameter of a hollow droplet (a) with $D_{eq} = 4.4\ mm$ $D_h = 5.6\ mm$ and $D_b = 4.5\ mm$, impacting at different We and Re numbers, (b) with $D_{eq} = 4.4\ mm$, impacting on the surface with $U_0 = 3.6\ m/s$ $(We = 790, Ca = 0.0016)$ with different hollowness ratios.

"The results show that the proposed model predicts maximum spreading diameter of a dense droplet of a hollow droplet with less than 10 percent error. The hollowness ratio for the hollow droplet that have been tested varies between 0.25-0.85.

The magnitude of term $3(1-\cos\theta_a)$ in equation (3-43) can be most 6. Therefore, in cases where $\frac{We}{\sqrt{Re}}I$ is large in comparison, the value of the contact angle with have little effect on the maximum spreading diameter of the hollow droplet. In addition, it can be concluded that if $We \gg I\sqrt{Re}$ the capillary effect can be neglected during the hollow droplet modeling. Furthermore, for the hollow droplets with $Bo \ll 1$, the effect of the gravity can be ignored during the modeling. It should be noted that this condition is applicable during the simulation of hollow droplet in thermal spraying process in which the size of the particle is in the range of milometers.

Considering the value for M and N parameters, if $We \gg 12$ the equation (3-43) reduces to

$$\frac{D_{max}}{D_{eq}} = \sqrt{\frac{M}{4I}}.Re^{0.25} \tag{3-48}$$

Based on the previous studies [47, 48], if the $We \to \infty$,

$$\frac{D_{max}}{D_{eq}} = 0.7\left(1 + \frac{4}{5}\chi\right) + (0.72 - \frac{2}{3}\chi)\mathrm{Re}^{0.25(1+\frac{\chi}{5})} \quad (3\text{-}49)$$

Where $\chi = (1 - (D_h - D_b))^3$.

Also if Re→∞, the equation (3-43) reduces to

$$\frac{D_{max}}{D_{eq}} = \sqrt{M\,We + 12N + Q\,Bo} \quad (3\text{-}50)$$

This is while based on the Gulyaev and Solonenko studies [47, 48],

$$\frac{D_{max}}{D_{eq}} = 0.75(1 + 0.8\chi) + (0.53 - 0.45\chi)\mathrm{We}^{0.508+0.02\chi} \quad (3\text{-}51)$$

Based on the numerical and theoretical results for hollow droplet flattening, the maximum spreading of the hollow droplet can be between 80-100% of the maximum spreading diameter of a dense droplet with the same mass. This percentage varies by the initial conditions before the impact including droplet velocity, bubble size, etc.

3.5 Conclusion

The flattening of hollow droplets is investigated comprehensively in the current study. We studied the influence of different parameters that may affect the hollow droplet characteristics after impact using experimental measurements and numerical modeling. Comparison of simulated images with photographs shows that the numerical analysis accurately predicts droplet shape during deformation. The results confirm that the main difference between the hollow and dense droplets is the formation of a counter-jet after the hollow droplet impact. As expected, the spreading diameter increases with droplet impact velocity increment, resulting from the higher kinetic energy of the droplet before impact. In addition, droplet impact velocity directly affects the counter-jet length. The counter-jet height grows as the droplet impact velocity increases. However, the counter-jet height rate change is the same almost for all velocities. The effect of bubble size is the other parameter that is studied and shows that for hollow droplets with the same outer diameter, the maximum spreading increases with bubble size reduction. In addition, the formation of the counter-jet is not dependent on the bubble size. However, there is an optimum bubble size which results in the most extended length for the counter-jet.

Furthermore, an analytical expression is developed to estimate the hollow droplet maximum spreading on a surface using the most influential parameters. Predictions from this model were shown to be in good agreement with the experimental measurements over a large range of *We* and *Re* numbers. It has been shown that the maximum spreading diameter of the hollow droplet is almost 90% of the maximum spreading of the dense droplet with the same mass and impact velocity. Furthermore, the splat thickness of the hollow droplet is nearly half of the splat thickness of the dense droplet.

3.6 Appendix

Appendix A.

The Mesh independency results are shown in Figure 3-22. The spreading diameter and the counter-jet length are shown for simulations with different numbers of meshes and the results show that the numerical solver simulations do not depends on the number of cells.

(a) (b)

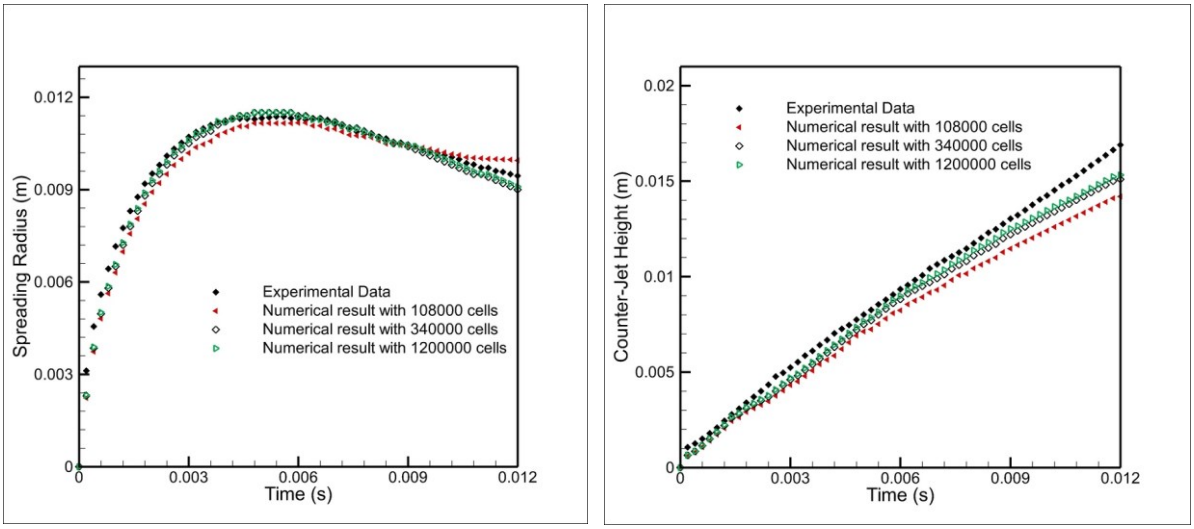

Figure 3-22. Mesh independency tests for hollow water droplet flattening. $D_H = 5.6\,mm$ and $D_B = 4.5\,mm$ impacting at $V = 3.6$ m/s (a) the spreading radius vs. time, (b) the counter jet height vs. time [107].

Figure 3-23 shows snapshots of numerical simulation of hollow water droplet impact on a surface. The outer diameter of the droplet and the impact velocity is the same for all cases. The only difference is the size of the entrapped bubble, which is located at the center of the droplet and varies from $\frac{\beta}{\alpha} = 0.5$ to $\frac{\beta}{\alpha} = 0.8$.

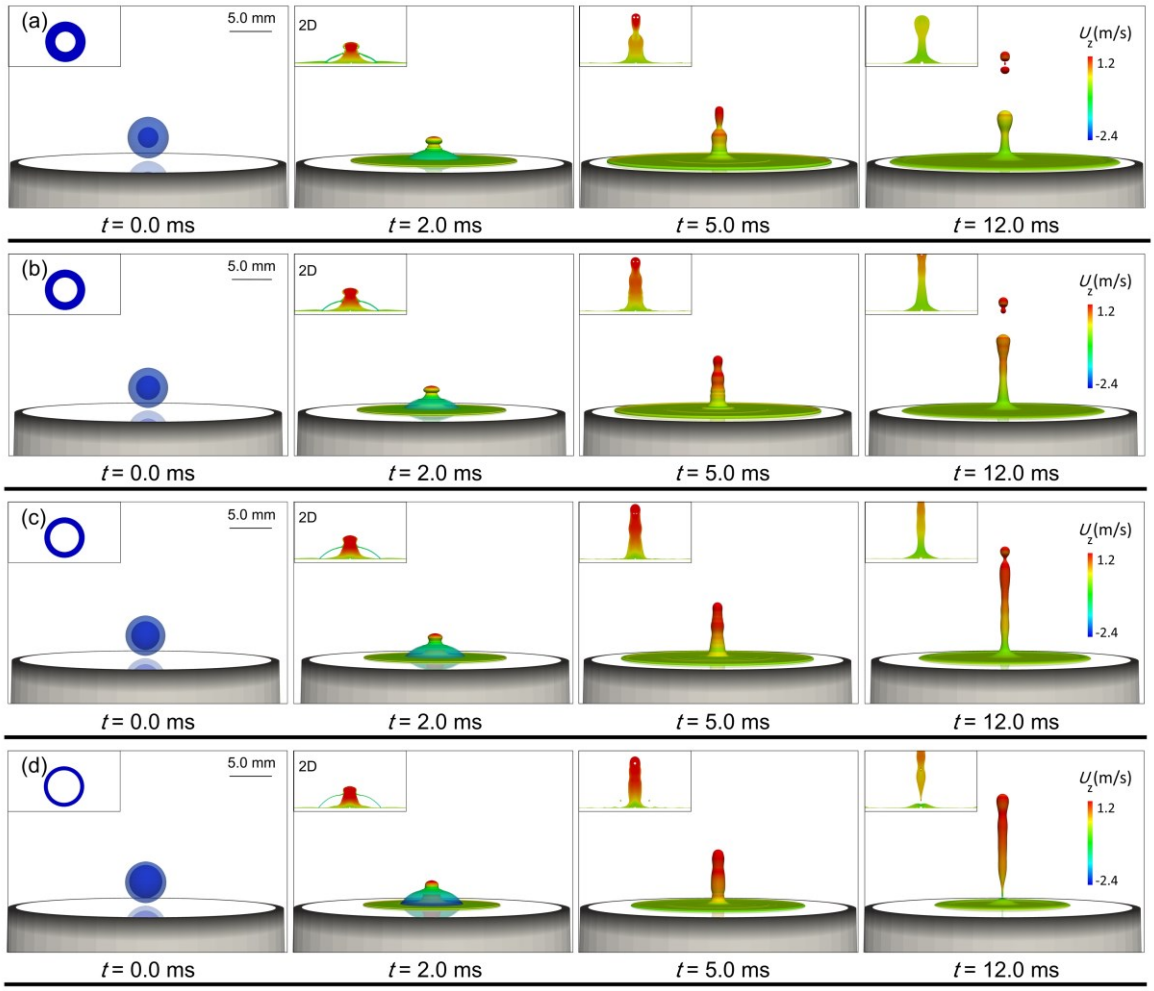

Figure 3-23. Selected snapshots of numerical simulation of a hollow water droplet impact with $D_h = 5.6\ mm, Ca = 0.0016$,and $U_0 = 3.6\ m/s$ with different bubble sizes.

(a) $\frac{\beta}{\alpha} = 0.5$ (b) $\frac{\beta}{\alpha} = 0.60$ (c) $\frac{\beta}{\alpha} = 0.71$ (d) $\frac{\beta}{\alpha} = 0.8$

Appendix B.

Figure 3-24 shows snapshots of numerical simulation of hollow water droplet impact on a surface. All impact parameters are the same except the location of the bubble, which varies from the droplet center ($\delta^* = 0.00$) to the upper half of the droplet ($\delta^* = 0.09$).

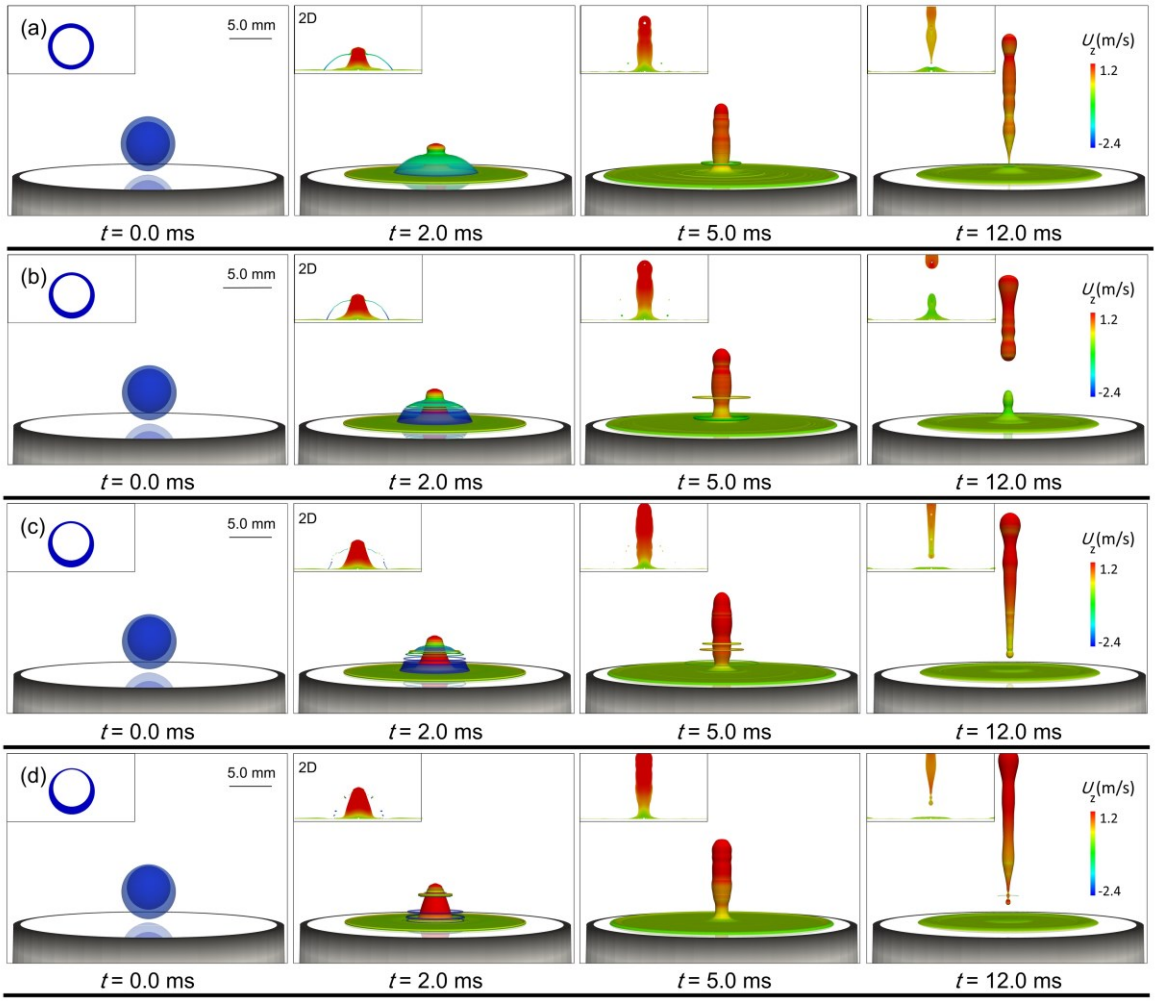

Figure 3-24. Selected snapshots of numerical simulation of a hollow water droplet with $D_h = 5.6\,mm, D_b = 4.5\,mm, D_{eq} = 4.4\,mm, U_0 = 3.6\,m/s,\ We = 790\ and\ Ca = 0.0016$ with different bubble locations. (a) bubble center at $\delta^* = 0.00$, (b) bubble center at $\delta^* = 0.03$, (c) bubble center at $\delta^* = 0.06$, and (d) bubble center at $\delta^* = 0.09$.

4 Chapter Four: Experimental and numerical simulation of a hollow droplet impacting a solid surface held at different angles

The content of this chapter will be submitted in the International Journal of Physics of Fluids, in April 2022.

4.1 Introduction

Droplet impingement on a solid or liquid surface is required for a wide variety of applications, including combustion, coatings deposition, inkjet printing, soil erosion, and air entrapment at the sea's surface [85, 110-113]. Drop impingement on a horizontal, smooth substrate is relatively fundamental. Alternatively, drop impingement on an inclined surface is much more complex, exhibiting other post-impacts [114-116]. Complex fluids in the drops have many applications in the industry [117], such as water-oil emulsions for steel strip manufacturing [118] or polymer solutions for agricultural sprays [119]. Several additive manufacturing processes have recently been proposed, including the use of multi-component droplets containing immiscible liquids, biomaterials, or reactive chemicals [119, 120].

Although thousands of studies have been published on dense droplet impingement [9, 93-97], only a minority have focused on the impact of a hollow droplet on a surface. Gulyaev et al. [47] and Nasiri et al. [107] are the only scholars who have studied the hollow droplet impact experimentally. Other research on hollow droplet flattening has concentrated on numerical modeling [17, 49, 52-54]. They have studied counter-jet formation, heat transfer rate prediction, maximum spreading diameter prediction, and multiple hollow droplets impact.

When a hollow droplet hits a surface, it spreads, and at the same time, a counter-jet forms inside the entrapped bubble (Figure 4-1) [107]. The counter-jet grows during the flattening of the hollow droplet, passes through the trapped bubble, and compresses the air inside the bubble, causing the bubble to rupture. The counter-jet expands and, depending on the impact velocity of the hollow droplet, either breaks apart and detaches from the surface or recoils toward the surface [107].

This study conducts a thorough experimental and computational investigation of the impact of hollow water droplets on surfaces held at various angles. A high-speed camera is used to study the flatting behavior of dense and hollow droplets as well as the development of the counter-jet. In addition, the volume of fluid (VOF) is utilized to simulate droplet flattening on surfaces at various angles.

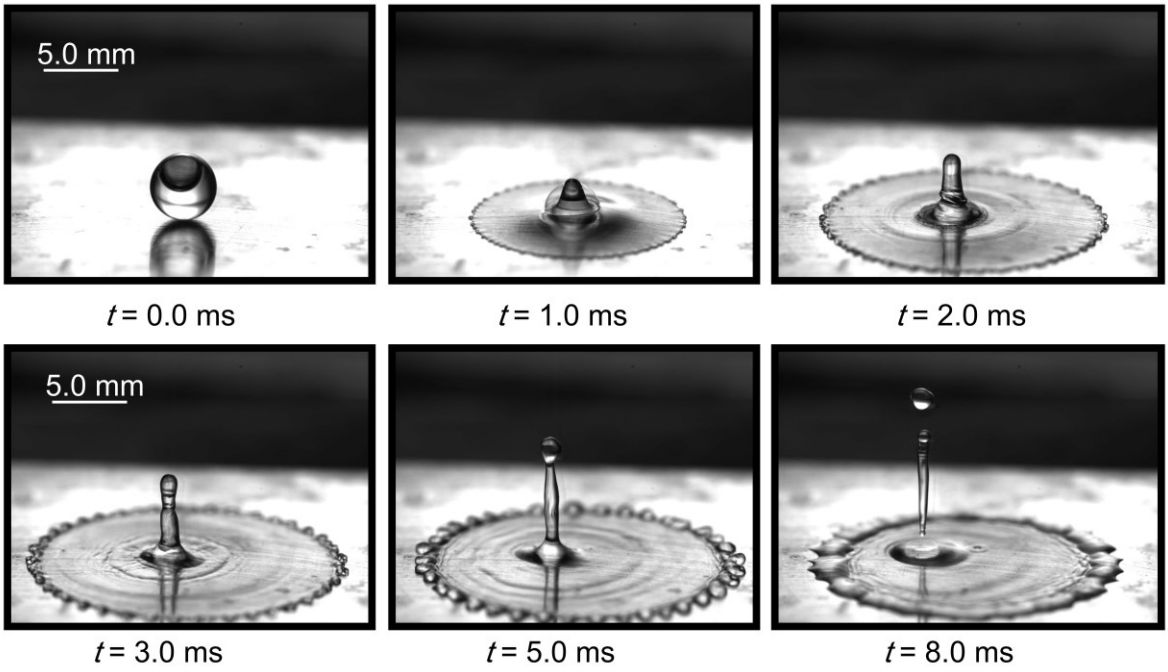

Figure 4-1. The impingement of a hollow water droplet with $D_h = 4.8\ mm$, $D_b = 3.2\ mm$ and $D_{eq} = 4.15\ mm$ on an aluminum surface at $U_0 = 3.6 \frac{m}{s}$.

4.2 Experiment setup and measurements

The experimental setup is depicted schematically in Figure 4-2. The impact trials were carried out in the natural environment, at room temperature, and with a relative humidity of 40%. The droplets are injected at a flow rate of 50 $\mu L/\ min$ through a needle with an outer diameter of 908 μm coupled to a syringe pump (Pico Plus, Harvard Apparatus). To inject air into the liquid droplet, another needle was placed within the primary needle. When a water droplet was released from the primary needle, the second needle injected an air bubble into it. The needle's height above the surface was changed from 20 to 70 mm, resulting in impact velocities ranging from 1.0 to 3.6 m/s. A high-speed camera (Phantom v711, Vision Research) captured the hitting droplet at 5000 fps and 30 μs exposure period. Two lights were utilized to illuminate the impact spot in order to catch both the top and side views of the droplet impact. In addition, three mirrors were used to reflect droplet impact photos into the camera from the top and side viewpoints (two mirrors to reflect the top view and one to reflect the side view). The video signal was saved to a PC's memory, and the images were processed with ImageJ software (version 1.46, National Institutes of Health, Bethesda, MD).

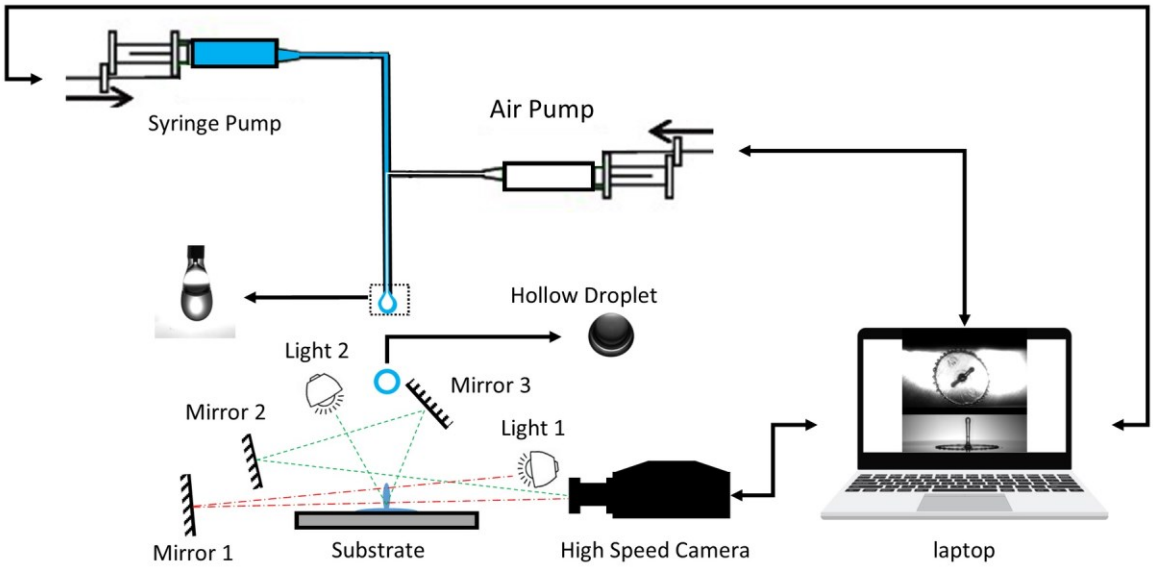

Figure 4-2. The schematic of the experimental setup of hollow droplet impact.

The apparent, advancing, and receding contact angles of the aluminum surface with water droplets were measured as 85°±2°, 94 °±2°and 65°±2°, respectively. Equation (4-1) was used to calculate the exact size of the bubble and the mass of the water droplet, considering the fisheye effect.

$$D_b = 0.86 * D_{b-image}. \tag{4-1}$$

$D_{b-image}$ indicates the measured diameter of the bubble, whereas D_b represents the precise diameter of the entrapped bubble. The accurate mass of the hollow water droplet was estimated using the actual outer diameter of the hollow droplet (D_h) and the diameter of the entrapped bubble (D_b).

4.3 Numerical analysis

The mass, momentum, and energy equations are the governing equations to be solved to simulate hollow droplet flattening with VOF method as [35],

$$\frac{\partial \rho}{\partial t} + \vec{\nabla}.(\rho \vec{U}) = 0, \tag{4-2}$$

$$\frac{\partial(\rho \vec{U})}{\partial t} + \nabla.(\rho \vec{U}\vec{U}) = -\vec{\nabla}p + \rho\vec{g} + \vec{\nabla}.\left\{\mu\left[\nabla\vec{U} + (\nabla\vec{U})^T\right]\right\} + \vec{F}_{vol}. \tag{4-3}$$

$$\frac{\partial(\rho c_p T)}{\partial t} + \vec{\nabla}.(\rho c_p \vec{U} T) = \nabla.(k\nabla T) + \frac{\partial p}{\partial t} - \left(\frac{\partial \rho K}{\partial t} + \vec{\nabla}.(\rho \vec{U} K)\right). \tag{4-4}$$

Where $\rho, \overrightarrow{U}, p, \vec{g}, K$ and c_p are mixture density, velocity field, pressure, gravitational acceleration, the kinetic energy of fluid, and the specific heat, respectively. To solve momentum equations properly, the pressure field can be calculated from the following equation [71]:

$$\left(\gamma \frac{\Psi_l}{\rho_l} + (1-\gamma)\frac{\Psi_g}{\rho_g}\right)\left[\frac{\partial p}{\partial t} + \vec{U}.\vec{\nabla}p\right] + \vec{\nabla}.\vec{U} = 0, \tag{4-5}$$

where Ψ_l, Ψ_g, ρ_l, and ρ_g are the compressibility and the density of liquid and gas, respectively.

To track the interface of two fluids, the VOF equation is used [71],

$$\frac{\partial(\gamma)}{\partial t} + \vec{\nabla}.(\gamma\,\vec{U}) = \frac{-\gamma\,\Psi_l}{\rho_l}\frac{Dp}{Dt} = \gamma(1-\gamma)\zeta + \gamma\vec{\nabla}.(\vec{U}) \tag{4-6}$$

By solving the above equation, the value of γ can be obtained for each computational cell. Once γ has been determined, the surface tension force can be calculated as follows [86, 121],

$$\vec{F}_{vol} = \sigma\kappa(\nabla\gamma), \qquad \kappa = -\nabla.\left(\frac{\nabla\gamma}{|\nabla\gamma|}\right), \tag{4-7}$$

where σ and κ represent the surface tension of the liquid and the surface curvature, respectively. The mixture properties can be expressed as,

$$\mu = \gamma\mu_l + (1-\gamma)\mu_g, \tag{4-8}$$

$$\rho = \gamma\rho_l + (1-\gamma)\rho_g, \tag{4-9}$$

$$k = \gamma k_l + (1-\gamma)k_g, \tag{4-10}$$

$$c_p = \gamma c_{p,l} + (1-\gamma)c_{p,g}. \tag{4-11}$$

The equations utilized to numerically solve the droplet impact phenomena are detailed in the author's previously published article [107].

To analyze the impact mechanism, a hollow droplet with $D_h = 5.6\,mm, D_b = 4.5\,mm$, and $D_{eq} = 4.4\,mm$ is simulated. With an initial temperature of 300 K, the hollow droplet impacts a flat metal surface vertically. The ambient temperature is 300 K, and the ambient pressure is 1 atm. Table 4-1 summarizes the fluid characteristics that were employed in this simulation.

Table 4-1. Physical properties of the employed fluids.					
	Density, ρ (Kg/m^3)	**Viscosity, μ** $(Kg/m.s)$	**Surface Tension, σ** (N/m)	**Thermal conductivity, k** $(W/m.K)$	**Specific heat, c_p** $(J/Kg.K)$
Water	998	8.9×10^{-4}	72×10^{-3}	0.6	4186
Air	1.225	1.8×10^{-5}	–	0.0242	1006.43

To investigate the hollow water droplet impact on inclined surfaces, a 3D domain must be used to simulate the droplet impact (Figure 4-3). Only half of the 3D domain is simulated for the symmetrical behavior of the droplet in the Y direction. It should be noted that the substrate is always kept horizontally (Z-plate), and it has no angle with the X-axis. To simulate drop impact on an inclined surface, the droplet's initial velocity vector components and gravitational force vector components are changed to account for the effect of the collision on an inclined surface. Table 4-2 shows the velocity and gravity vector components that describe droplet impact on sloping surfaces.

Table 4-2. Droplet initial velocity and gravity component before the impact					
		magnitude	**X component**	**Y component**	**Z component**
Impact on a surface held at 0 degrees	Impact velocity (m/s)	3.0	0.0	0.0	-3.0
	Gravity (m/s^2)	9.81	0.0	0.0	-9.81
Impact on a surface held at 10 degrees	Impact velocity (m/s)	3.0	0.52	0.0	-2.95
	Gravity (m/s^2)	9.81	1.70	0.0	-9.66
Impact on a surface held at 25 degrees	Impact velocity (m/s)	3.0	1.27	0.0	-2.72
	Gravity (m/s^2)	9.81	4.14	0.0	-8.05
Impact on a surface held at 45 degrees	Impact velocity (m/s)	3.0	2.12	0.0	-2.12
	Gravity (m/s^2)	9.81	6.94	0.0	-6.94

Except for the top and symmetry boundary, the boundaries are assumed to be walls. On the walls, the pressure is set to be zero-gradient, and the velocity is considered to be zero. On the top boundary, the pressure is presumed to equal atmospheric pressure, and the velocity is set to zero-gradient.

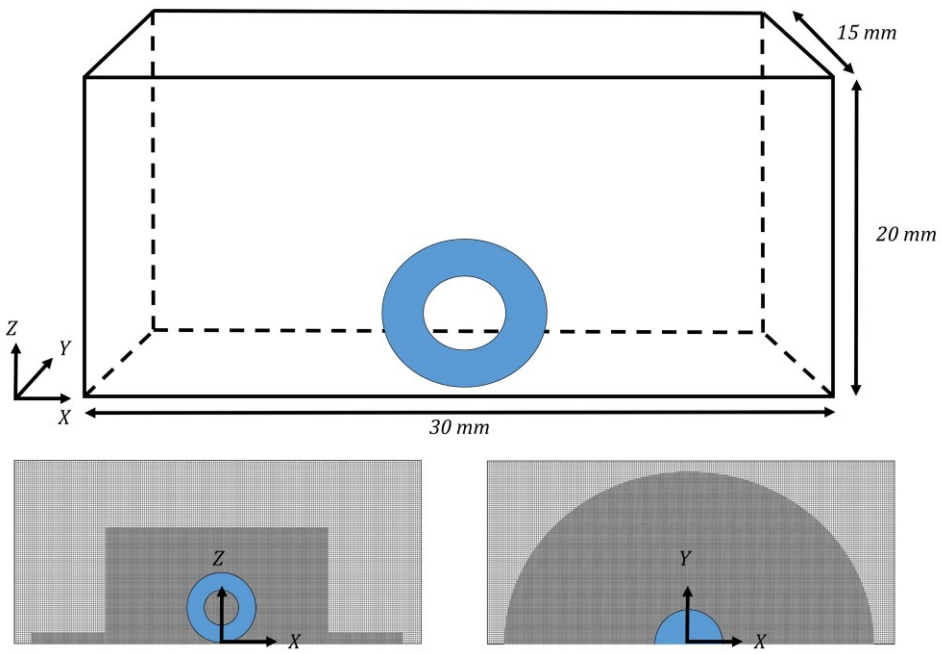

Figure 4-3. Computational domain and boundary conditions of the specified problem.

4.4 Results and discussion

When a dense droplet collides with a surface, the liquid pressure rises due to the droplet's kinetic energy prior to contact. As a result, the droplet spreads across the surface until its maximum spreading diameter is reached (Figure 4-4.a, and b). There are no disturbances or oscillations on the spreading droplet's surface, and there are little fingerings on the droplet's rim until the droplet becomes an integrated liquid sheet, as can be seen. When the droplet's kinetic energy converts to surface energy or dissipates due to viscosity, it achieves its maximum spreading diameter. The liquid sheet recoils toward the center at this point, and little waves emerge on its surface until the equilibrium point between surface energy and potential energy is met. Depending on the contact angle between the liquid and the surface, the liquid normally forms a semi-sphere at this point.

On the contrary, when a hollow droplet impacts a surface, a counter-jet takes shape in the axial direction (Z-axis) as the droplet flattens on the surface (Figure 4-4.c, and d). The pressure gap inside the droplet caused by bubble entrapment enables the counter-jet to form following the hollow droplet impact. While the hollow droplet achieves its maximum spreading width, the center counter-jet continues to develop. The counter-jet eventually breaks up from spreading liquid, and a portion of the liquid mass detaches and leaves the surface. The presence of the entrapped bubble has an additional influence on the droplet's flattening. The bubble compresses

and collapses during the first stages of the hollow droplet impact due to the high pressure of the droplet. The ruptured bubble generates waves and disturbances on the flattening liquid's surface, breaking apart the liquid sheet from the center and forming a hole within the flattening liquid sheet.

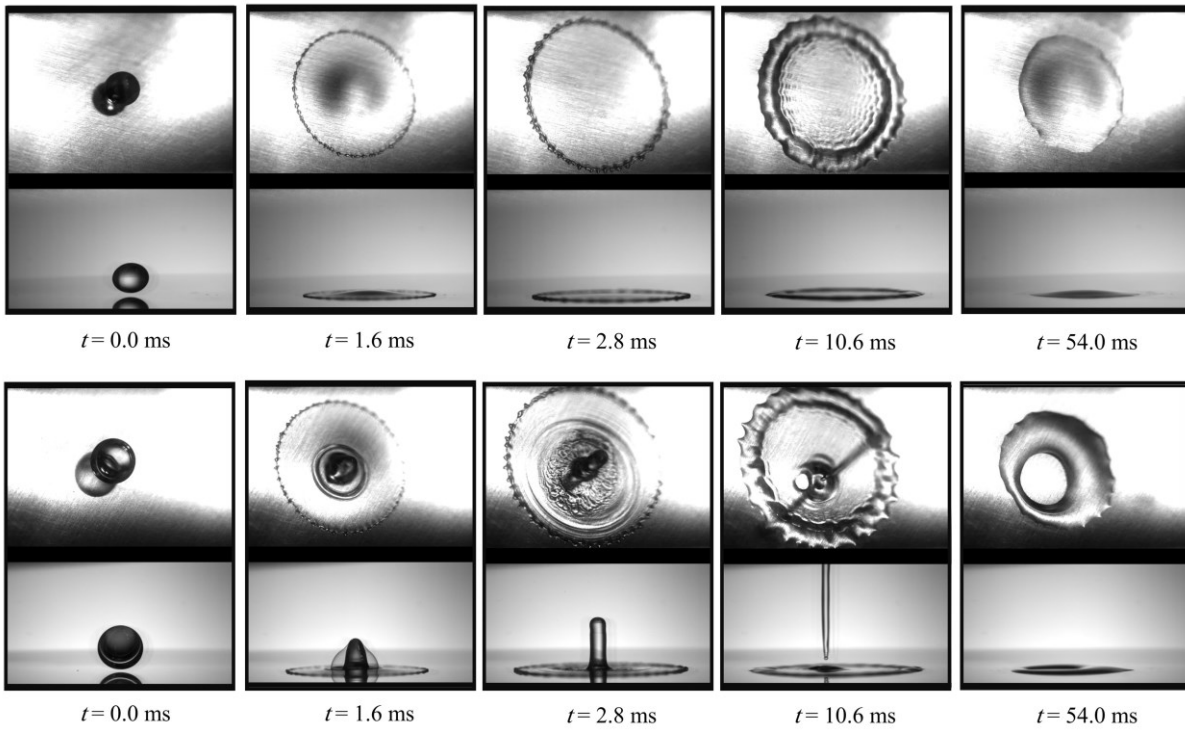

Figure 4-4. Selected snapshots showing droplet impact on an aluminum surface at $U_0 = 3.4\ m/s$.
(a) top view of a dense water droplet with $D_{eq} = 4.4\ mm$ (b) side view of a dense water droplet with $D_{eq} = 4.4\ mm$ (c) top view of a hollow water droplet with $D_h = 5.6\ mm, D_b = 4.5\ mm$ and $D_{eq} = 4.4\ mm$ (c) hollow water droplet with $D_h = 5.6\ mm, D_b = 4.5\ mm$ and $D_{eq} = 4.4\ mm$ (d) hollow water droplet with $D_h = 5.6\ mm, D_b = 4.5\ mm$ and $D_{eq} = 4.4\ mm$.

As a result, as the liquid recoils toward the center, it cannot acquire a semi-spherical shape and instead remains on the surface as a donut shape (Figure 4-4.d at $t = 54.0\ ms$). The production of a counter-jet, the breakup of a bubble, and the imposed perturbations are all inherent phenomena observed after a hollow droplet impact on varied wettability surfaces. Appendix A shows the outcomes of a hollow droplet impact on superhydrophobic and grid-blasted surfaces.

The counter-jet grows and penetrates the bubble shell, which ruptures the bubble eventually. As it can be seen, even though a portion of the mass of the hollow droplet leaves the surface, the spreading diameter of both dense and hollow droplets is almost the same (Figure 4-5.c, and d). This similar spreading diameter can be attributed to the increased surface energy of hollow

droplets prior to impact. The liquid sheet fragmentation induced by the hollow droplet collision is also captured during simulations.

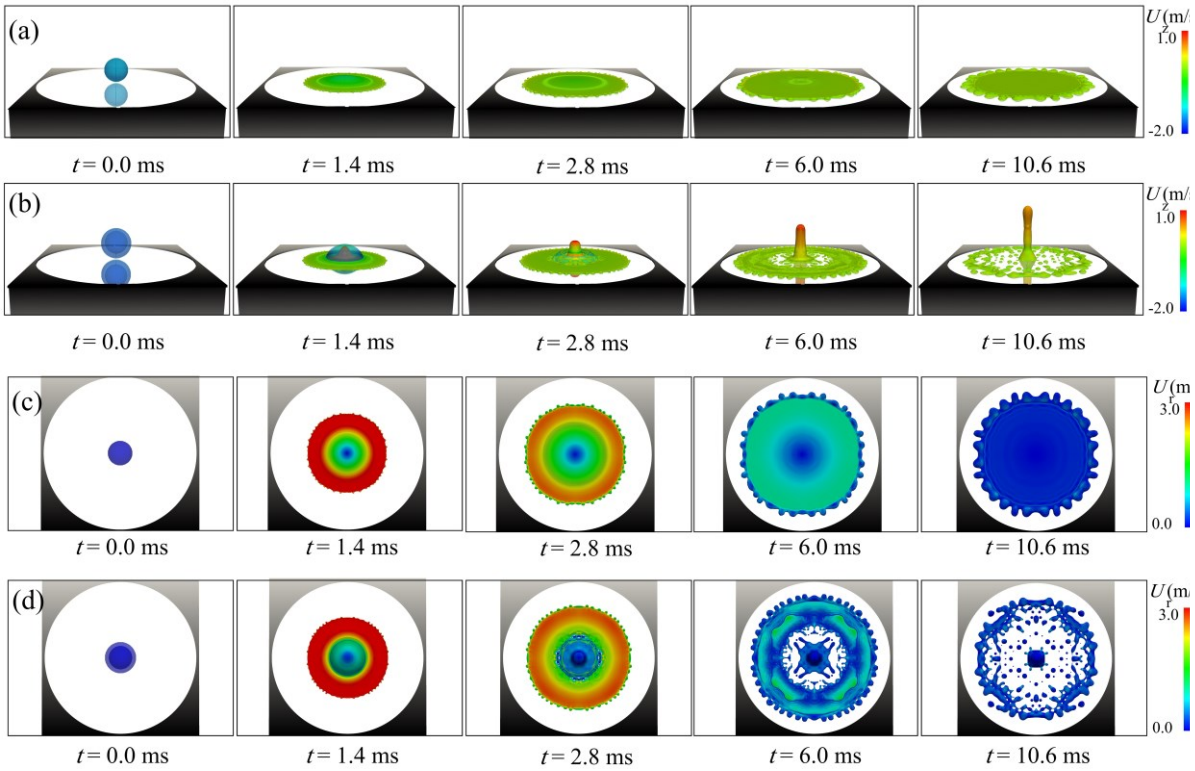

Figure 4-5. Selected snapshots of numerical simulation of a water droplet impact with $U_0 = 3.0\, m/s$ on a surface.

(a) side view of dense droplet impact $D_{eq} = 4.4\, mm$ (b) side view of the hollow droplet impact $D_h = 5.6\, mm, D_b = 4.5\, mm, D_{eq} = 4.4\, mm$ (c) radial velocity contour of the top view of the dense droplet impact $D_{eq} = 4.4\, mm$ (d) radial velocity contour of the top view of the hollow droplet impact $D_h = 5.6\, mm, D_b = 4.5\, mm, D_{eq} = 4.4\, mm$.

Figure 4-6 depicts snapshots of a numerical simulation of bubble rupture during the first stages of a hollow droplet impact on a surface. As it is clear, the penetration of the counter-jet into the bubble upper shell triggers the bubble rupture (Figure 4-6.a). The bubble rupture occurs at the center of the spreading liquid, which has a lower radial velocity (Figure 4-6.b). The bubble rupture imposes minor disturbances on the surface of the spreading liquid, as seen by the vorticity contour in Figure 4-6.c. These disturbances disintegrate the spreading liquid sheet. As a result, the liquid cannot rebound toward the center, and the liquid sheet ultimately acquires the form of a doughnut (Figure 4-4).

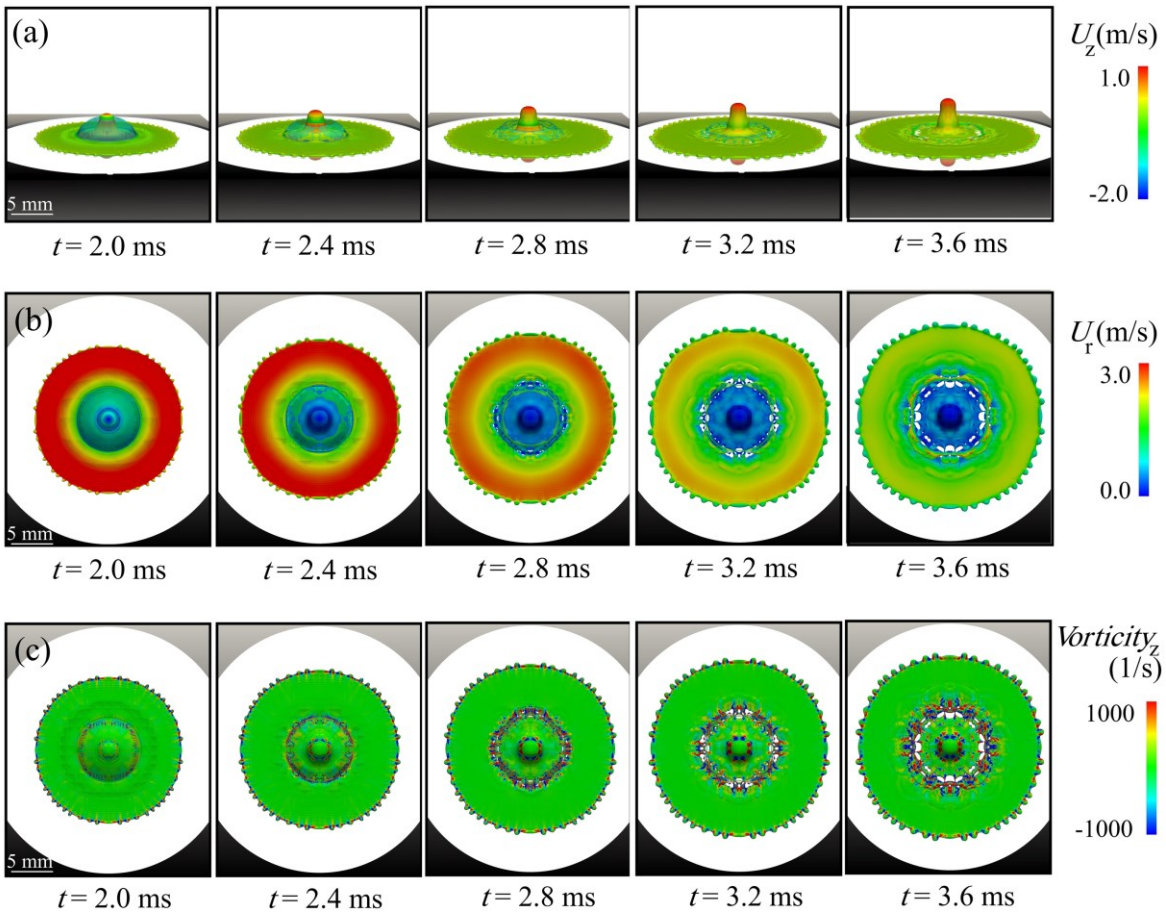

Figure 4-6. Selected snapshots of numerical simulation of the bubble rupture during a hollow water droplet impact.

$U_0 = 3.0\ m/s,\ D_h = 5.6\ mm, D_b = 4.5\ mm, D_{eq} = 4.4\ mm$ (a) side view of the bubble rupture, (b) radial velocity contour of the top view of the bubble rupture, (c) vorticity contour of the top view of the bubble rupture

As previously stated, liquid fragmentation is created by the disturbances imposed on the liquid surface following bubble rupture. The effects of the hollow droplet impact velocity on counter-jet production and droplet spreading are visualized in Figure 4-7. After a high-velocity hollow droplet impacts on a surface ($U_0 = 3.4\ m/s$), a counter-jet forms immediately after impact, passes through the bubble shell, and expands until it detaches from the surface (Figure 4-7.c, and d). In the case of a low-velocity hollow droplet impact ($U_0 = 2.0\ m/s$), the counter-jet emerges after the collision and passes through the bubble the shell at a lower velocity than in the case of a high-velocity impact. Because of the counter-low jet's inertia, it cannot detach from the surface and recoil toward the surface. The maximum spreading diameter of the droplet is another variation between the hollow droplet impact at various velocities. As can be observed, the droplet spreads further after impact with higher velocity, owing to the droplet's higher inertia prior to impact. The final distinction is the form of the droplet after impact.

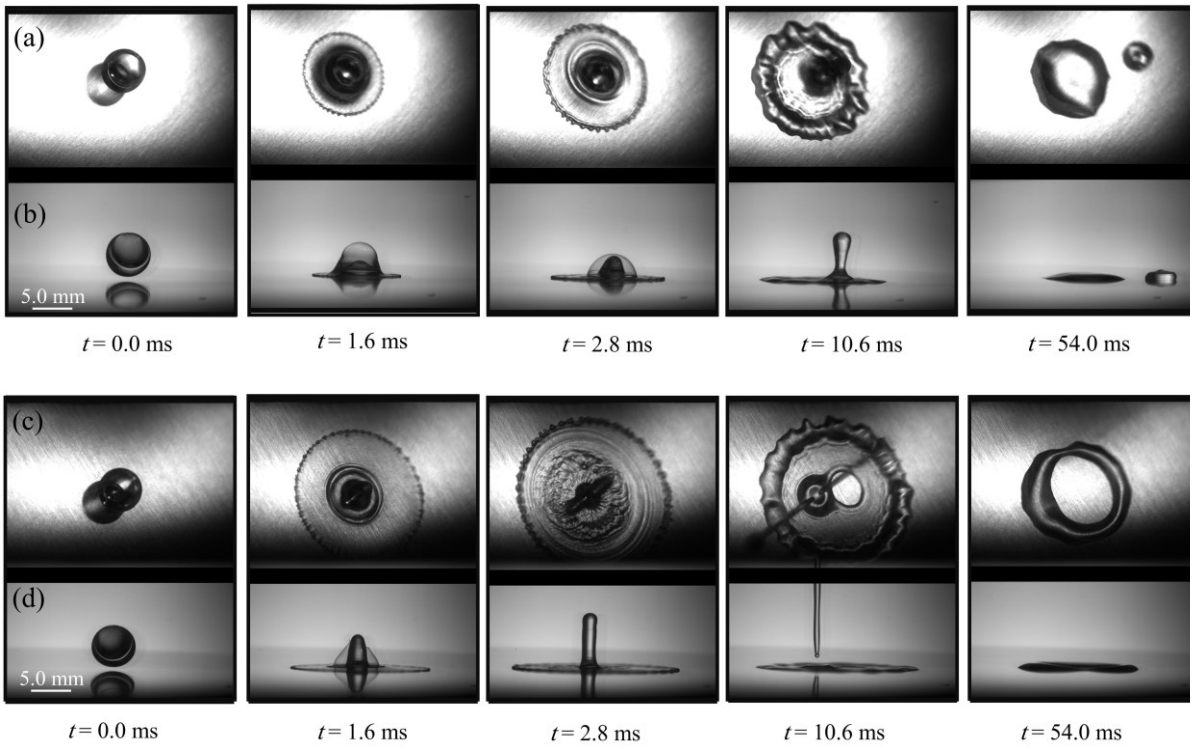

Figure 4-7. Selected snapshots showing hollow droplet impact on an aluminum surface at different velocities. (a) top view of the hollow droplet impact at $U_0 = 2.0\ m/s$ (b) side view of the hollow droplet impact at $U_0 = 2.0\ m/s$ (c) top view of the hollow droplet impact at $U_0 = 3.4\ m/s$ (d) top view of the hollow droplet impact at $U_0 = 3.4\ m/s$.

As shown, the hollow droplet develops a donut form after impacting with high velocity due to disturbances induced on the liquid's surface. However, even if the bubble rupture is caught in the case of a low-velocity hollow droplet collision, the imposed perturbations are not strong enough to split the liquid sheet. The liquid dampens the disturbances and persists as a coherent liquid bulk, recoiling toward the center and forming a semi-spherical shape. Experiments were done for a hollow droplet contacting an aluminum surface at 10, 25, and 45 degrees to investigate the influence of surface inclination on the flattening of a hollow droplet.

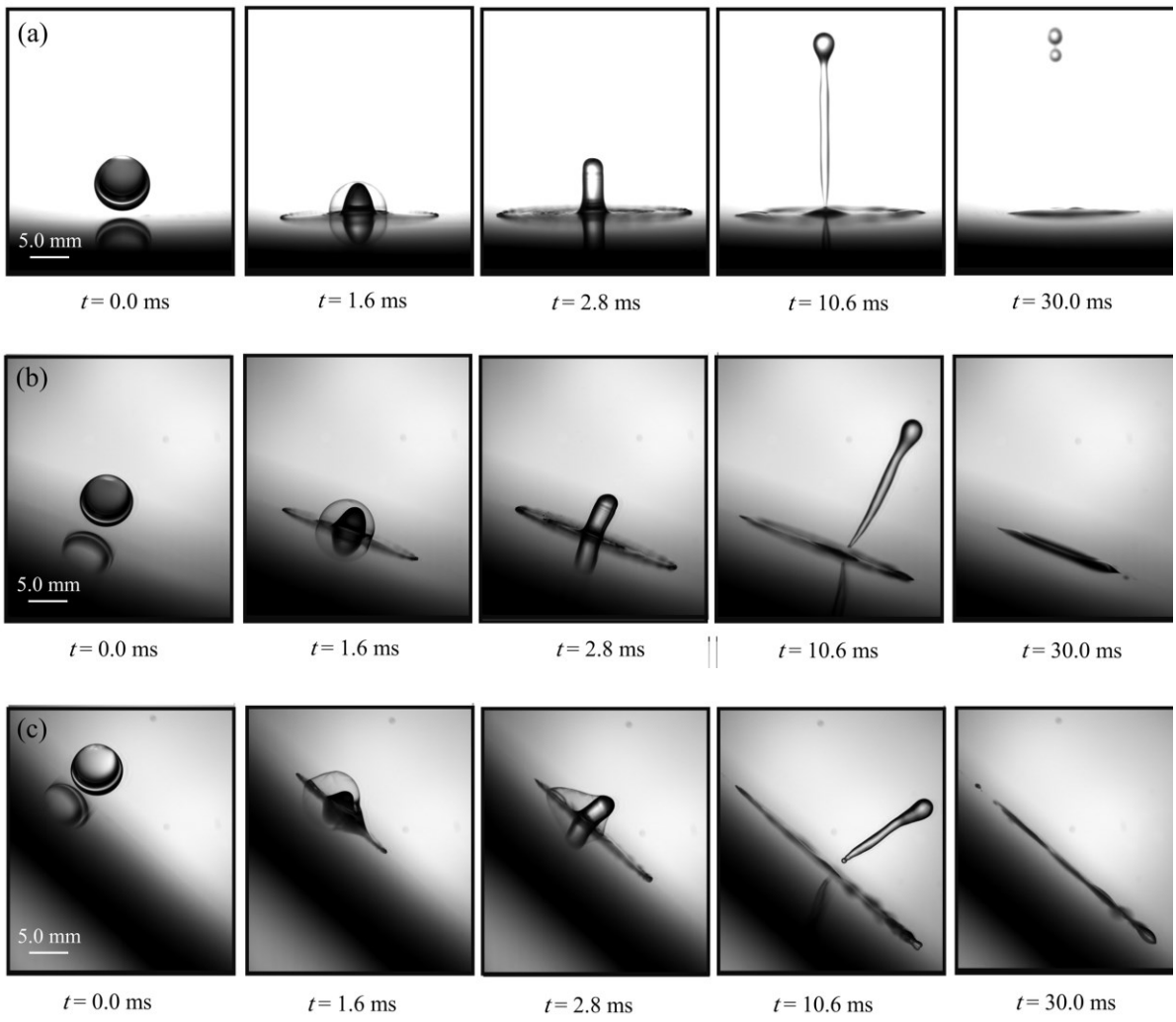

Figure 4-8. Selected snapshots showing side view of a hollow droplet impact with $U_0 = 3.0\, m/s$ on an aluminum surface at different angles.

(a) surface held at 0 degrees (b) surface held at 25 degrees (c) surface held at 45 degrees.

Figure 4-8 and Figure 4-9 show the effect of surface inclination. The counter-jet occurs after the collision perpendicular to the inclined surfaces, similar to the hollow droplet impact on a horizontal surface. Nonetheless, there are two distinctions between droplet impact on a horizontal surface and droplet impact on an inclined surface. The length of the counter-jet generated after collision on a level surface is greater than the length of the counter-jet formed after impact on an inclined surface. The impact velocity of a droplet on an inclined surface is divided into normal and tangential components.

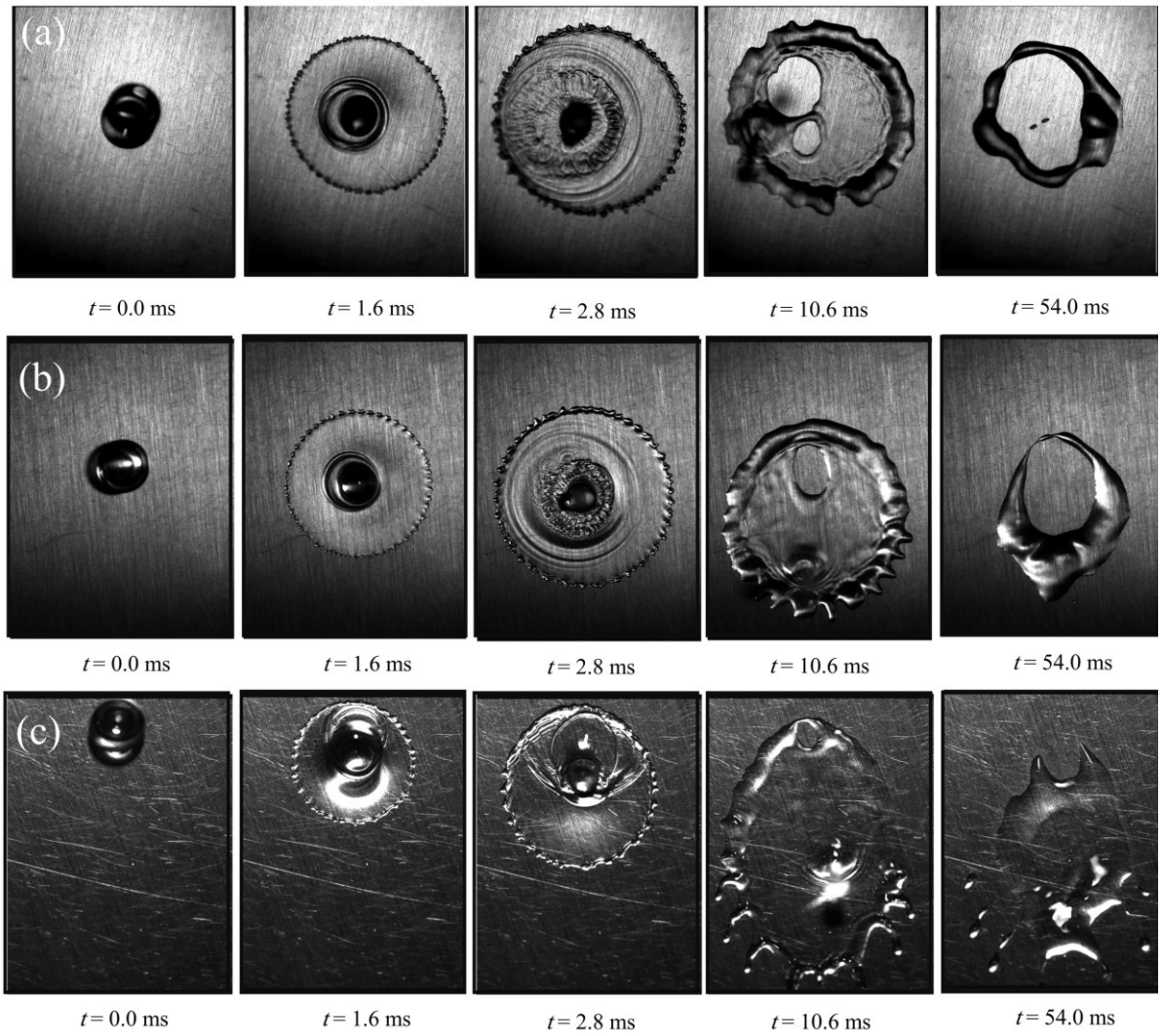

Figure 4-9. Selected snapshots showing the top view of a hollow droplet impact with $U_0 = 3.0\ m/s$ on an aluminum surface at different angles.

(a) surface held at 0 degrees (b) surface held at 20 degrees (c) surface held at 45 degrees.

The shorter length of the counter-jet on sloped surfaces is owing to the droplet velocity vector's smaller normal component. The tangential velocity of the droplet, on the other hand, influences its spreading. Furthermore, the droplet's tangential velocity causes a tangential velocity in the counter-jet. As a result, the counter-jet flows in the direction of surface inclination while remaining perpendicular to the surface. When a droplet collides with an inclined surface, its structure is distorted, and it spreads asymmetrically relative to the point of contact (Figure 4-9). With time, elongation and back-to-front asymmetry grow. For impact on a horizontally held surface, the difference in the spread velocity of the lamellas in the front and back directions is identical. This discrepancy grows as the surface inclination rises. When the radial velocity in that direction approaches zero, the maximum spread of the rear lamella is attained.

Even on the surface with high angles, the bubble collapse is caught (45 angles). The bubble rupture causes disturbances on the spreading liquid's surface, which leads to liquid sheet breakup. Following the impact of the hollow droplet on the horizontal substrate, the liquid sheet disintegration might begin at any point. However, when the surface slope increases, the fragmentation point moves to the shorter side of the spreading droplet. This is due to the lower energy of the spreading liquid's rear portion, which can be dominated by the induced perturbations.

Figure 4-10 displays the flattening properties of a dense and hollow droplet upon impact on a surface with various slopes. It should be noticed that the x values were defined starting from the impact point. Despite the fact that a portion of the hollow droplet mass exits the surface after impact, the hollow droplet's spreading behavior is comparable to that of the dense droplet (Figure 4-10.a, and b). This resemblance is due to the greater surface energy of the hollow droplet before contact because of bubble entrapment. The spreading lengths of the hollow droplet are identical on the surface at 0 degrees, as shown. This symmetric behavior, however, is eliminated by substrate inclination.

Another characteristic that is affected by substrate inclination is counter-jet length (Figure 4-10.c). It is shown that the size of the counter-jet decrease as the substrate inclination grows. This is due to the hollow droplet's lower normal velocity vector component before the impact. The counter-jet has the shortest length after impacting substrate held at 45 angles.

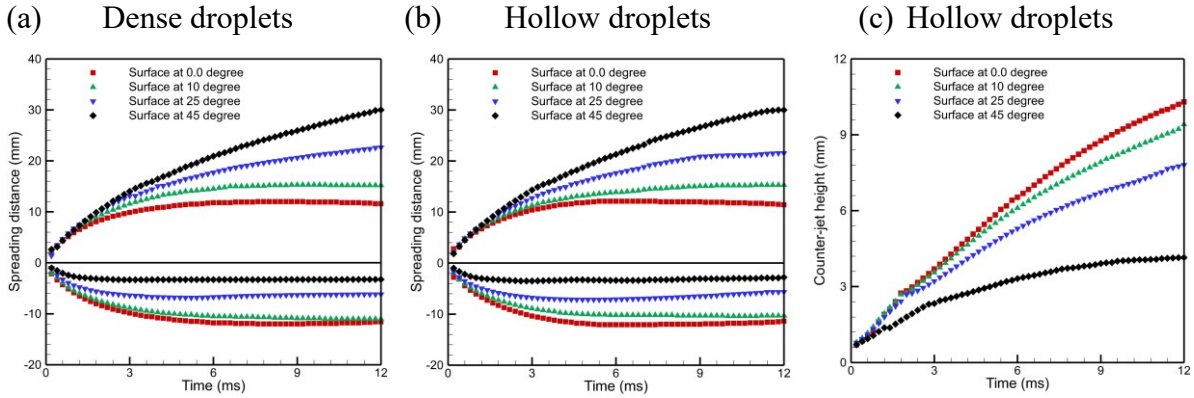

Figure 4-10. Spreading characteristics of droplets with $D_{eq} = 4.4\ mm$ and $Ca = 0.0016$ impacting at different velocities.

(a) spreading diameter ($D_s^* = D_s/D_{eq}$) versus time ($t^* = t\ U_0/D_{eq}$) for a dense droplet $D_{eq} = 4.4\ mm$ (b) spreading diameter ($D_s^* = D_s/D_{eq}$) versus time ($t^* = t\ U_0/D_{eq}$) for a hollow droplet $D_h = 5.6\ mm, D_b = 4.5\ mm$ and $D_{eq} = 4.4\ mm$ (c) counter-jet height ($h_{cj}^* = h_{cj}/D_{eq}$) versus time for the hollow droplet

To learn more about the influence of surface inclination on the flattening of hollow droplets, numerical simulations were conducted. All surfaces are assumed to be at 0 degrees, and the

impact velocity and gravity direction components are specified to account for the surface inclination. The properties of the velocity and gravity components representing a surface with various inclination angles are presented in Table 4-2. Figure 4-11 depicts snapshots of a hollow droplet flattening on surfaces at various angles. It should be noted that the droplet velocity magnitude in all cases is $U_0 = 3\ m/s$. While the velocity and gravity components are set in such a way that Figure 4-11.a, b, and c depict hollow droplet impact on a surface maintained at 0, 25, and 45 degrees, respectively.

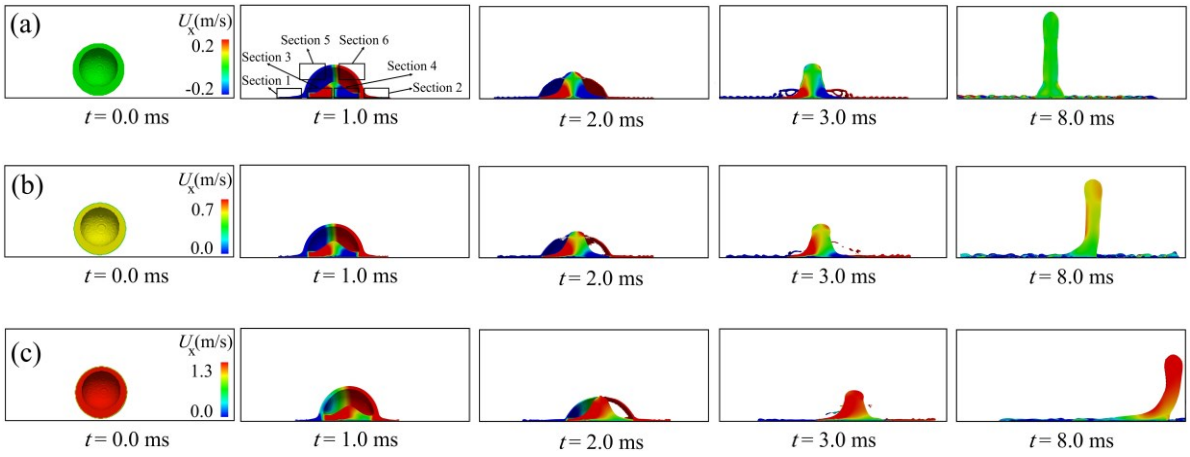

Figure 4-11. The contour of the velocity X-component after a hollow droplet with $D_h = 5.6\ mm, D_b = 4.5\ mm$ and $D_{eq} = 4.4\ mm$ impact.

(a) surface held at 0 degrees with $U_0 = 3\ m/s$ (equal to droplet impact on a horizontal surface with velocity and gravity components $U_{0_X} = 0.0, U_{0_Y} = 0.0, U_{0_Z} = -3.0, g_X = 0.0, g_Y = 0.0, g_Z = -9.81$) (b) surface held at 25 degrees with $U_0 = 3\ m/s$ (equal to droplet impact on a horizontal surface with velocity and gravity components $U_{0_X} = 1.27, U_{0_Y} = 0.0, U_{0_Z} = -2.72,\ g_X = 4.42, g_Y = 0.0, g_Z = -8.89$) (c) Droplet impact on a surface held at 45 degrees with $U_0 = 3\ m/s$ (equal to droplet impact on a horizontal surface with velocity and gravity components $U_{0_X} = 2.12, U_{0_Y} = 0.0, U_{0_Z} = -2.12, g_X = 6.94, g_Y = 0.0, g_Z = -6.94$).

When a hollow droplet collides with a horizontal surface (Figure 4-11.a at $t = 1.0\ ms$). several sections can be evaluated. Sections 1 and 2 are the liquid portions that spread on the surface and move away from the center, Sections 2 and 3 are the liquid portions that move toward the center to produce the counter-jet, and Sections 5 and 6 are the upper shell of the bubble that is stretching and moving away from the center. Only sections 1-4 remain on the surface once the bubble ruptures. Sections 1 and 2, 3 and 4, and 5 and 6 are symmetric after a hollow droplet impact on a surface kept at 0 degrees. However, these sections become asymmetric when the surface angle fluctuates. The counter-jet acquires tangential velocity in the X-direction, and the

magnitude of the tangential velocity is equal to the droplet velocity component in the X-direction prior to impact on the surface.

4.5 Conclusion

The flattening of a hollow droplet on horizontal and inclined surfaces is thoroughly examined utilizing experimental measurements as well as numerical modeling. As simulated images are compared to photographs, the numerical analysis successfully predicts droplet shape during deformation. The creation of a counter-jet after a hollow droplet contacts a surface is a primary distinction between hollow and dense droplets. The pressure gap inside the hollow droplet due to an entrapped bubble allows the counter-jet to develop. Consequently, the bubble rupture induces disturbances on the surface of the liquid sheet, leading it to spread and disintegrate. As a result of the recoil toward the center, the liquid adopts the form of a doughnut.

When a droplet collides with an angled surface, it spreads asymmetrically. In both hollow and dense droplets, this behavior is predicted. Besides, the counter-jet forms on an inclined surface, comparable to the effect of a hollow droplet on a horizontal surface. However, the surface inclination affects the counter-jet length. The counter-jet length decreases with the hollow droplet impact with constant velocity as the surface inclination increases. In fact, the size of the counter-jet jet is controlled by the velocity component that is normal to the surface. In addition, the tangential component of the hollow droplet velocity vector before impact imposes a tangential velocity on the counter-jet. As a result, the counter-jet forms parallel to the surface.

4.6 Appendix

Appendix A.

The hollow droplet impact experiments were repeated on superhydrophobic and grid-blast surfaces to demonstrate that counter-jet production is a natural result of the hollow droplet impact. Table 4-3 displays the measured contact angles of aluminum, superhydrophobic, and grid-blast surfaces.

Table 4-3. Measured contact angles of water on different surfaces.

	Apparent contact angle	Advancing contact angle	Receding contact angle
Aluminum	85° ± 3°	94° ± 2°	66° ± 2°
SHS	163° ± 2°	165° ± 3°	162° ± 2°
GBS	42° ± 2°	52° ± 2°	32° ± 3°

The counter-jet formation of the hollow droplet after impact on a grid-blast surface is similar to the aluminum surface (Figure 4-12). Nevertheless, there are minor differences in the flattening of the droplet on this surface. As shown in Figure 4-12 at time 10.6, the number of holes inside the liquid sheet is higher than the liquid sheet on the aluminum surface due to the different dynamic contact angles of the surfaces, which makes the liquid sheet prone to fragmentation. That is why that recoiled liquid forms a narrow rim with several big holes inside of it.

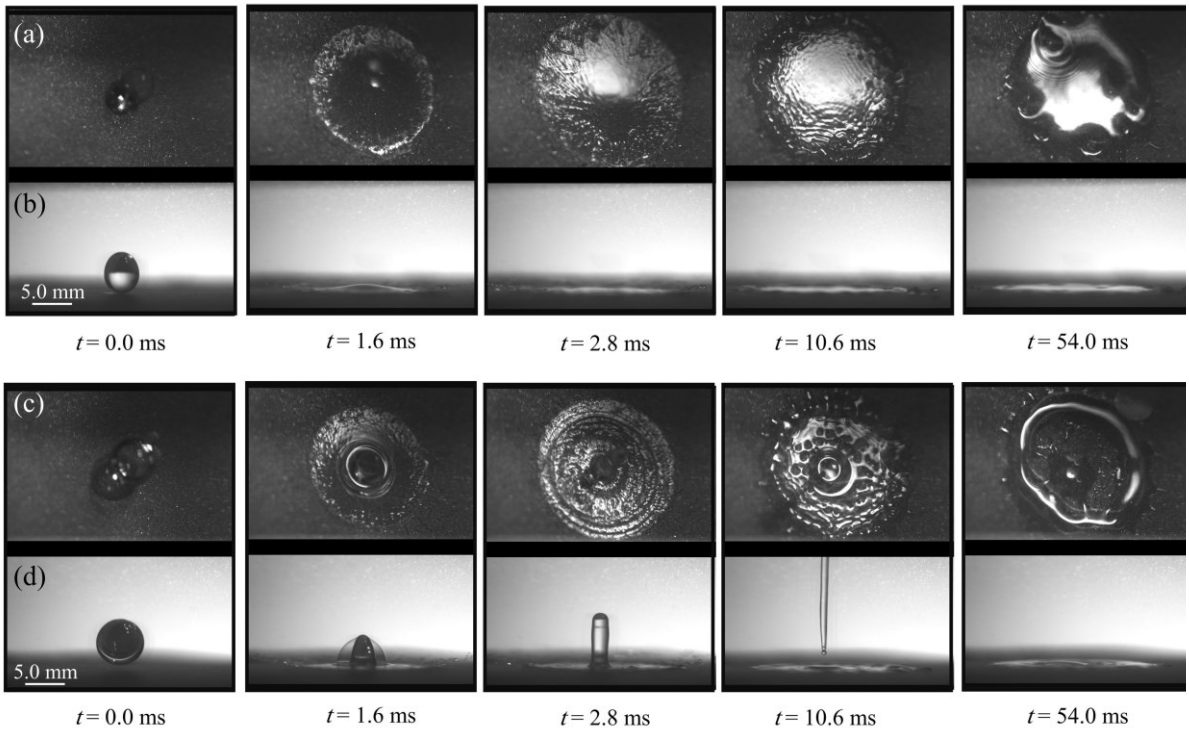

Figure 4-12. Selected snapshots showing droplet impact on a Grid-blast surface at $U_0 = 3.4\ m/s$.
(a) top view of a dense water droplet with $D_{eq} = 4.4\ mm$ (b) side view of a dense water droplet with $D_{eq} = 4.4\ mm$ (c) top view of a hollow water droplet with $D_h = 5.6\ mm, D_b = 4.5\ mm$ and $D_{eq} = 4.4\ mm$ (c) hollow water droplet with $D_h = 5.6\ mm, D_b = 4.5\ mm$ and $D_{eq} = 4.4\ mm$ (d) hollow water droplet with $D_h = 5.6\ mm, D_b = 4.5\ mm$ and $D_{eq} = 4.4\ mm$.

In the case of a dense droplet impact on a superhydrophobic surface, the contact between the liquid and substrate is lower on superhydrophobic surfaces compared to hydrophobic surfaces. For droplets with high kinetic energy, splashing is a common phenomenon that occurs after the droplet impact on a superhydrophobic surface. In summary, when a droplet impacts the superhydrophobic surface, it cannot make good contact with the surface spreads faster, and produces a thinner liquid sheet than the droplet impact on hydrophobic surfaces (Figure 4-13.a,

and b). When the liquid sheet reaches its maximum spreading diameter, it cannot dissipate small perturbations that are imposed from the surface to the liquid sheet, and liquid disintegration occurs. The liquid sheet disintegration starts from the rim of the liquid sheet and grows until the whole liquid sheet breaks up and leaves the surface (Figure 4-13.a and b).

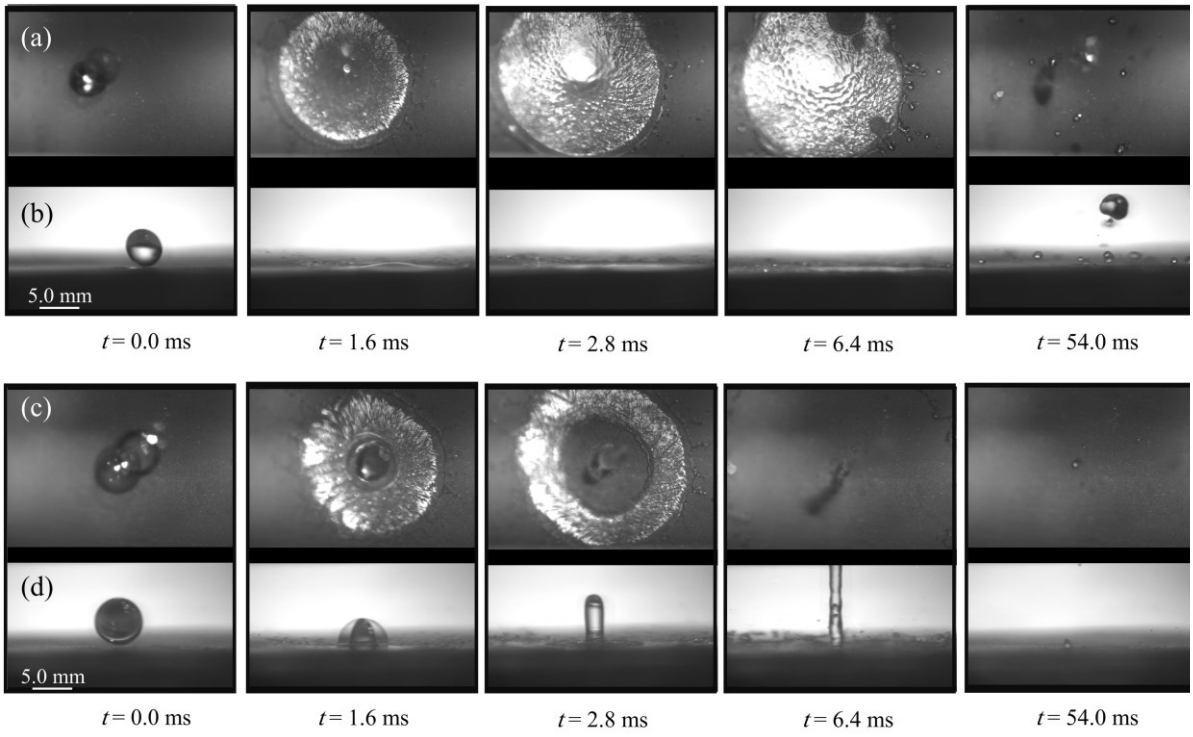

Figure 4-13. Selected snapshots showing droplet impact on a superhydrophobic surface at $U_0 = 3.4\ m/s$. (a) top view of a dense water droplet with $D_{eq} = 4.4\ mm$ (b) side view of a dense water droplet with $D_{eq} = 4.4\ mm$ (c) top view of a hollow water droplet with $D_h = 5.6\ mm, D_b = 4.5\ mm$ and $D_{eq} = 4.4\ mm$ (c) hollow water droplet with $D_h = 5.6\ mm, D_b = 4.5\ mm$ and $D_{eq} = 4.4\ mm$ (d) hollow water droplet with $D_h = 5.6\ mm, D_b = 4.5\ mm$ and $D_{eq} = 4.4\ mm$.

The counter-jet formation sequences seen in the case of hollow droplet impact on the superhydrophobic surface are comparable to those found on the aluminum surface (Figure 4-13). Conversely, the flattening of the hollow droplet on the hydrophobic surface differs in several aspects. When a bubble ruptures on a superhydrophobic surface, it forms waves and perturbations on the liquid sheet's surface. This time, the liquid sheet is unable to withstand these disturbances and fractures rapidly from the center. The liquid sheet's disintegration rate is so quick that it does not allow the liquid sheet to extend to its greatest extent. The liquid sheet of a hollow droplet separates from the surface considerably more quickly than the liquid sheet of a dense droplet (Figure 4-13.c, and d).

Figure 4-14 represents the impact of a hollow droplet at various velocities on a surface held at 25 degrees. At all velocities, the counter-jet forms as predicted after the droplet impact. The spreading size and counter-jet length, on the other hand, grow as the impact velocity increases. Furthermore, in droplet impact with higher velocity, the counter-jet has higher tangential velocity. As a result, the counter jet moves faster along a straight line parallel to the surface.

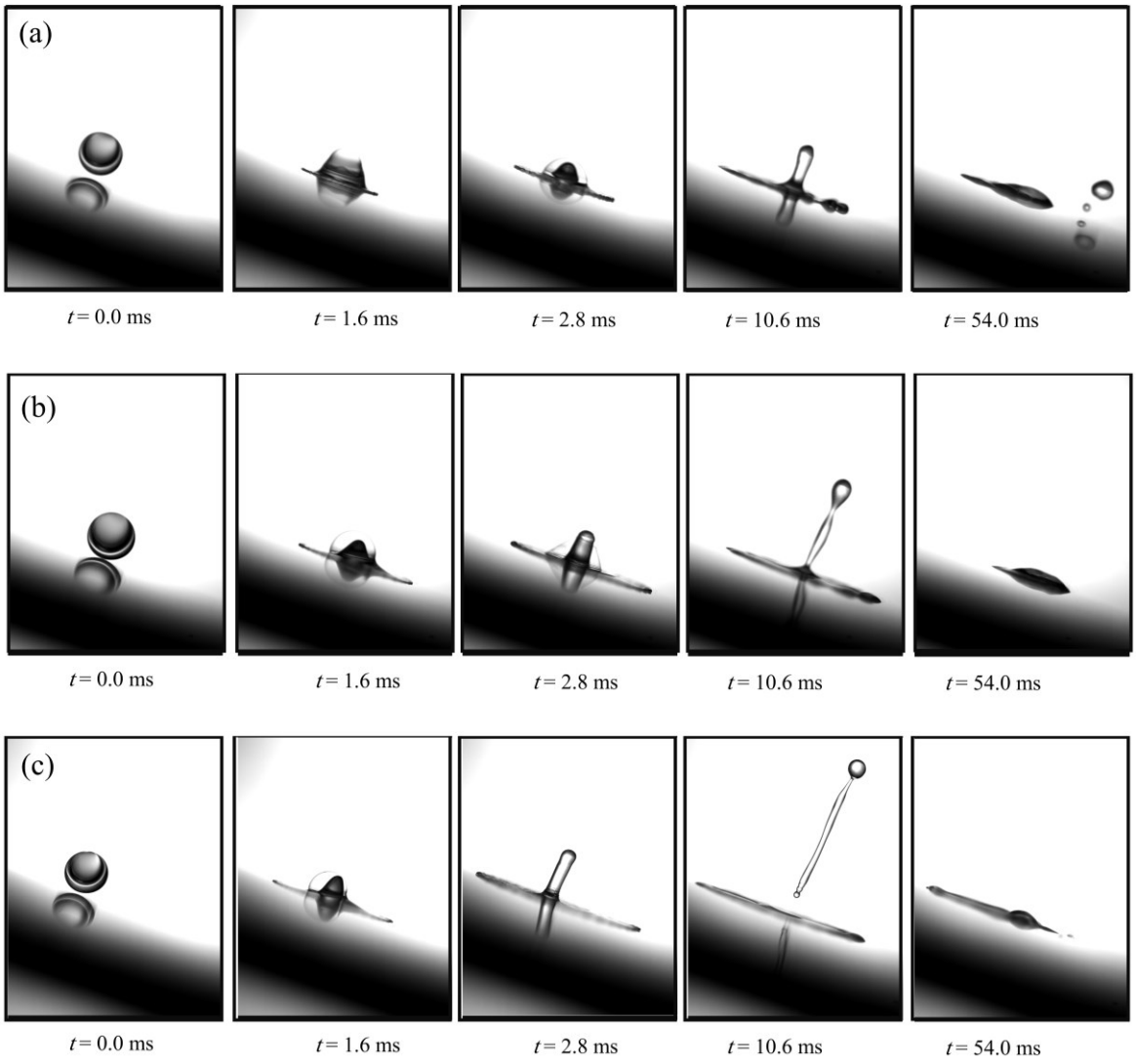

Figure 4-14. Selected snapshots show the side view of a hollow droplet impact on an aluminum surface held at 25 degrees at different velocities.
(a) $U_0 = 2.0\ m/s$ (b) $U_0 = 2.4\ m/s$ (c) $U_0 = 3.7\ m/s$.

5 Chapter Five: Modeling of liquid detachment and fragmentation during the impact of plasma spray particles on a cold substrate

The content of this chapter has been accepted as a paper in the International Journal of Heat and Mass Transfer, in February 2022.

5.1 Introduction

Droplet impact has several applications in various industries, including medicine [122], power generation, ink-jet printing [123], aerospace, and thermal spraying [14]. Therefore, several scholars have focused on the study of droplet flattening and its relative phenomena, for instance, droplet spreading and recoiling, droplet splashing [90], etc. Plasma spraying is a process that produces coated layers with a thickness that ranges from tens of micrometers to several millimeters. Thermal barrier coating (TBC) is one of the thermal spraying products in which a plasma torch melts the micrometer-sized particles and sprays them with high velocity toward a substrate [15, 124]. During this process, molten particles spread on the substrate surface, solidify, and produce layers with a thickness of several micrometers. The characteristics of the final coated layer depend on the spreading and solidification of these micrometer sized molten particles.

In fundamental studies on droplet impact and solidification, it has been shown that the flattening behavior of these molten particles is similar to what had been observed in millimeter-sized droplet impact. After droplet impact, it spreads smoothly on the substrate four times of its initial size, solidifies, and forms a uniform solidified layer [23, 46] (disk splat; Figure 5-1.a Cu particles sprayed onto AISI304 substrate held at 700 K, and Figure 5-1.b Ni20Cr powder sprayed on mirror-polished stainless steel substrates held at 700 K). The accumulation of these solidified layers on top of each other produces a coated layer. There are other conditions in which the flattening behavior of the droplet changes, for instance, "prompt splash" [110] or "corona splash" [125]. Both splash phenomena can be classified within the finger-splashing morphology. Splashing is a phenomenon of material projections from the lamella main body caused by the upward disturbance and instabilities developed around the spreading tip [27]. The velocity of impact, the drop size and shape, liquid surface tension, surface wettability and even, the compressibility of the surrounding gas [126] are the parameters that affect the mass and energy distribution of the ejected droplets leading to these splashes.

However, there are extreme conditions in which the shape of solidified splat is different from the previously observed disk splat. In these cases, the droplet spreads up to 10 times its initial size (overspreading) [23, 127-130]. In addition, in the end, only a small portion of the molten particle solidifies at the center with a different shape compared to the disk splat, while this core is surrounded by some debris [23, 28, 55, 57, 131, 132] (fragmented splat; Figure 5-1.c Cu particles sprayed onto AISI304 substrate held at room temperature, and Figure 5-1.d Ni20Cr powder sprayed on mirror-polished stainless steel substrates held at 700 K). The

droplet's overspreading and fragmented splat formation and parameters that affect them are different than what was reported for droplet splashing on dry surfaces [90].

It has been reported that fragmented splats become the dominant type of splats at specific substrate temperatures and pressures [23, 28, 55-61, 131]. Most droplet splats formed on substrates held at room temperature and atmospheric pressure are fragmented splats. The ratio of fragmented splats to disk splats decreases with substrate temperature increment and, at a specific temperature, disk splats become the central splat on the substrate [23, 28, 55-61, 63-66, 131]. This specific substrate temperature has been defined as the "transition temperature" (T_t) [55, 62]. Generally, fragmented splats are the dominant type of splats if the temperature of the substrate is held lower than the transition temperature while the pressure of the environment gas is close to the atmospheric pressure. For instance, the splats formed on the substrate held at room temperature and atmospheric pressure are mostly fragmented.

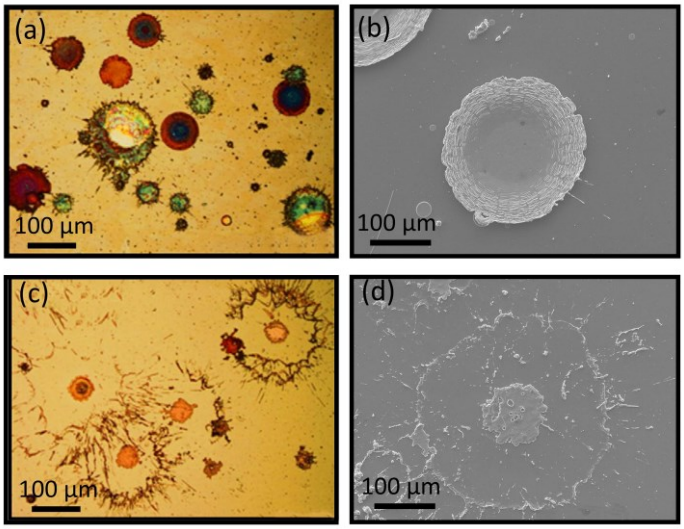

Figure 5-1. Splat formation of the surface during plasma spraying.
(a) disk splats [57] (b) single disk splat [63] (c) fragmented splats [57] (d) single fragmented splat [63].

The pressure of the surrounding gas is the other parameter that affects the type of splats. Yang et al. [55] observed that only 10% of the splats deposited at atmospheric pressure and room temperature are disk splats. The splat shape tends to change from the fragmented splat to the disk splat with a decrement in the surrounding gas pressure [55, 56, 69]. A transition pressure (P_t) has been proposed that defines the pressure at which the fraction of disk splats exceeds 50% of the total splats formed on the substrate surface held at room temperature [55].

Although substrate temperature and ambient pressure influence on the formation of the fragmented splats is well established, the reasons behind this phenomenon are not fully understood. Li et al. [70] studied the substrate surface adsorbents; they noted that water is the

main component at the surface. This water is adsorbed in several monolayers of the substrate surface and can have a thickness between 2 and 10 nm [65]. It has been proposed that the desorption of the water from the surface in the form of water vapor during droplet impact prevents the droplet from establishing good contact with the surface. This desorbed gas makes an isolation layer between the spreading liquid and the substrate surface, leading to overspreading of the droplet and the formation of the fragmented splat. In addition, this isolation layer increases thermal resistance between the droplet and the substrate [23, 28, 55-61, 63-66]. Furthermore, there is poor contact between the fragmented splat and substrate surface held at room temperature [28, 57].

Kinetics of adsorption and desorption are mainly controlled by the molecular jump frequency and activation energy, which are determined by species, surface characteristics, the volume of adsorption, temperature, and pressure. When a system at equilibrium adsorption-desorption is heated, the desorption will be dominant until equilibrium is achieved. When a system at equilibrium adsorption-desorption is cooled, the adsorption will be dominant until equilibrium is achieved. [133]. In general, the equilibrium volume of an adsorbate sharply decreases with an increase in temperature and a decrease in pressure. When the pressure of the system at adsorption/desorption equilibrium decreases, desorption will be dominant until equilibrium is restored [55].

Parallel to the experimental studies, numerical investigations have been performed on the droplet impingement and solidification [134, 135] to study the effect of compressible gas on droplet flattening and splat formation. For instance, during a droplet impact on a liquid pool, the compressible gas can be entrapped between the droplet and the pool and affect droplet flattening [87, 136], or the gas can affect the droplet flattening as a trapped bubble inside a droplet in the shape of a hollow droplet [50, 84, 92, 107]. Safaei et al. [17] investigated the impact of a YSZ hollow droplet on a surface in thermal-spray conditions with compressible fluid assumption. Although these studies provide beneficial information and methods to simulate droplet flattening and solidification, the numerical investigation of the formation of disintegrated splats is limited to the study of McDonald et al. [137]. They captured droplet fragmentation assuming a combination of slip and no-slip boundary conditions on the walls together with high thermal contact resistance between the droplet and the impact surface, based on the adsorption/desorption hypothesis [137].

In this paper, the effects of gas desorption on the formation of fragmented splats are investigated. To this end, numerical simulations are performed for droplets impacting on a

surface in thermal spraying conditions. To do so, the compressible Navier-Stokes equations are solved in a 2D axisymmetric domain. Volume of Fluid (VOF) method is used to capture the liquid and gas interface. In addition, the source base method is used to consider the effect of solidification in the momentum and energy equations. Finally, a simplified desorption model is defined to study the effect of the thickness of the adsorbate layer on the flattening and fragmentation of a yttria-stabilized zirconia particle impacting a substrate at room temperature. Three cases are simulated. The first case with the substrate held at $T = 700$ K (hot surface), the second case with the substrate held at room temperature $T = 300$ K without any gas desorption, and the third case with the substrate held at room temperature $T = 300$ K containing adsorbed gas film layer (cold surface). Other initial conditions are identical for all cases. First, numerical simulations are performed, ignoring gas desorption on substrates, to study only the effect of substrate temperature on the flattening of the droplet (first case and second case). With the knowledge of these results, numerical simulations are repeated considering the adsorption/desorption hypothesis (third case).

5.2 Numerical methodology

5.2.1 Governing equations

Compressible Navier—Stokes equations are the governing equations to simulate droplet flattening in plasma spraying conditions. However, the basic compressible Navier—Stokes equations are not capable of capturing solidification. Therefore, special parameters should be considered within these equations. The conservation of mass equation is as follows,

$$\frac{\partial \rho}{\partial t} + \vec{\nabla}.(\rho \vec{U}) = 0. \tag{5-1}$$

ρ and $\vec{U}$ are mixture density and velocity field.

The compressible momentum equation is [17],

$$\frac{\partial(\rho \vec{U})}{\partial t} + \nabla.(\rho \vec{U} \vec{U}) = -\vec{\nabla} p + \rho \vec{g} + \vec{\nabla}.\left\{\mu\left[\nabla \vec{U} + (\nabla \vec{U})^T\right]\right\} + \overrightarrow{F_{Vol}} - \overrightarrow{S_v}. \tag{5-2}$$

p is pressure, $\vec{g}$ is gravity, μ is viscosity and $\overrightarrow{S_v}$ is the solidification source term. Surface tension is considered as a source term ($\overrightarrow{F_{Vol}}$), and is calculated using the Brackbill method [72].

To solve the compressible momentum equations, the pressure equation must be calculated.

$$\left(\gamma\frac{\Psi_l}{\rho_l}+(1-\gamma)\frac{\Psi_g}{\rho_g}\right)\left[\frac{\partial p}{\partial t}+\vec{U}.\vec{\nabla}p\right]+\vec{\nabla}.\vec{U}=0. \tag{5-3}$$

Ψ_l, Ψ_g, ρ_l, and ρ_g are the liquid compressibility, the gas compressibility, and the liquid and gas density, respectively. Fluid compressibility is defined as $\Psi=\partial\rho/\partial P$. Considering the ideal gas equation of state, gas compressibility becomes,

$$\Psi_g=\frac{1}{zRT}, \tag{5-4}$$

z represents the compressibility factor, and T is the temperature. Assuming isothermal equation of state, the liquid compressibility is [17]:

$$\Psi_l=\frac{1}{a^2}, \tag{5-5}$$

Parameter a represents sound velocity in the liquid.

The VOF equation for compressible flow must be used to capture the interface of the liquid and the gas [71];

$$\frac{\partial(\gamma)}{\partial t}+\vec{\nabla}.\left(\gamma\,\vec{U}\right)=\frac{-\gamma\,\Psi_l}{\rho_l}\frac{Dp}{Dt}=\gamma(1-\gamma)\zeta+\gamma\vec{\nabla}.\left(\vec{U}\right), \tag{5-6}$$

$$\zeta=\left\{\frac{\Psi_l}{\rho_l}+\frac{\Psi_g}{\rho_g}\right\}\frac{Dp}{Dt}.$$

Solving equation (6), the value of liquid volume fraction (γ) is obtained for each computational cell. A unity value of γ indicates that the cell is occupied by the liquid, whereas a value of $\gamma=0$ represents a cell occupied by the gas. Any value between $0<\gamma<1$ indicates that the cell contains a liquid-gas interface (Figure 5-2).

The surface tension force is calculated as follows [72];

$$\overrightarrow{F_{Vol}}=\sigma\kappa(\nabla\gamma),\qquad \kappa=-\nabla.\left(\frac{\nabla\gamma}{|\nabla\gamma|}\right). \tag{5-7}$$

σ and κ represent the surface tension of the liquid and the surface curvature, respectively. $\nabla\gamma$ is a continuous function that is zero everywhere in the domain except for the transitional area at the interface. In addition, an indicator function (θ) is defined to represent the solid part of the droplet. The value of θ is set to one for areas in the domain entirely occupied by gas and

liquid while it has the value of zero in cells occupied by solid, and it has a value between zero and one in any cell located at the liquid-solid interface (Figure 5-2).

$$\theta = \begin{cases} 1 & fluid \\ 0 < \theta < 1 & interface \\ 0 & solid \end{cases} \qquad \gamma = \begin{cases} 1 & liquid \\ 0 < \gamma < 1 & interface \\ 0 & gas \end{cases} \tag{5-8}$$

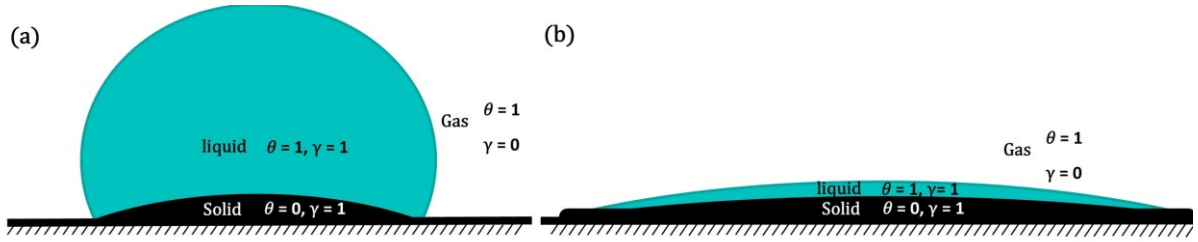

Figure 5-2. Schematic of gas-liquid-solid interfaces during droplet solidification.
(a) the droplet impact (b) the spalt formation.

θ function is calculated using Rösler and Brüggemann equation [77],

$$\theta = 0.5erf\left(\frac{4(T - T_m)}{(T_l - T_s)}\right) + 0.5, \tag{5-9}$$

T_l is the liquidus temperature, T_s is the solidus temperature, and T_m is the average of T_l and T_s ($T_m = {(T_s + T_l)}/{2}$).

Solidification source term $\overrightarrow{S_v}$ can be calculated from equation (5-10). Parameter A varies from zero to a significant value, as the local solid fraction,

$$\overrightarrow{S_v} = -A\,\vec{U}, \qquad A = \frac{-C\,(1-\theta)^2}{(\theta^3 + \varepsilon)}. \tag{5-10}$$

To model heat transfer and solidification effects, it is necessary to solve the energy equation. The energy equation for compressible flow has been derived as follows [73];

$$\frac{\partial(\rho H)}{\partial t} + \vec{\nabla}.(\rho\,\vec{U}H) = \nabla.(k_{eff}\nabla T) + \frac{\partial p}{\partial t} - \left(\frac{\partial \rho K_E}{\partial t} + \vec{\nabla}.(\rho\,\vec{U}K_E)\right). \tag{5-11}$$

where K_E and H are the kinetic energy of fluid and the total enthalpy, respectively.

Using the source-based method, the enthalpy has been expressed as a function of temperature. In this method, the enthalpy has been defined as a function of temperature.

$$H = h + \Delta H, h = h_{ref} + \int_{T_{ref}}^{T} C_{p_{eff}} dT. \tag{5-12}$$

ΔH is latent enthalpy and $C_{p_{eff}}$ is the effective specific heat capacity. Substituting calculated H into equation (5-12)

$$\frac{\partial\left(\rho C_{p_{eff}} T\right)}{\partial t} + \vec{\nabla}.\left(\rho\, \vec{U} C_{p_{eff}} T\right) = \nabla.\left(k_{eff}\nabla T\right) + \frac{\partial p}{\partial t} - \left(\frac{\partial \rho K_E}{\partial t} + \vec{\nabla}.\left(\rho\, \vec{U} K_E\right)\right) + S_h, \tag{5-13}$$

$$S_h = \left(\frac{\partial(\rho \Delta H)}{\partial t} + \nabla.\left(\rho \vec{U} \Delta H\right)\right).$$

where S_h, and k_{eff} are the solidification source term and the conduction heat transfer coefficient of the mixture, respectively. The latent heat is considered as a function of temperature to calculate the solidification source term ($\Delta H = f(T)$). To do so, it is assumed that the latent enthalpy (ΔH) is a fraction of the total latent heat of fusion (L) in the mushy zone,

$$\Delta H = \theta L, \tag{5-14}$$

θ is the fluid fraction inside the solidifying droplet and is calculated using equation (5-15),

$$\frac{\partial \theta}{\partial t} = \frac{4\left(e^{-\left(\frac{4(T-T_m)}{(T_l-T_s)}\right)^2}\right)}{(T_l - T_s)\sqrt{\pi}} \frac{\partial T}{\partial t}, \tag{5-15}$$

Finally, the energy source term becomes,

$$S_h = -\rho L \frac{4\left(e^{-\left(\frac{4(T-T_m)}{(T_l-T_s)}\right)^2}\right)}{(T_l - T_s)\sqrt{\pi}} . \left(\frac{\partial T}{\partial t} + \vec{U}.\vec{\nabla} T\right). \tag{5-16}$$

In the current formulation, the mean properties of phases are calculated as follows. g, l, and s indexes represent gas, liquid, and solid phases, respectively, and d indexed parameters consist of liquid and solid phases.

$$\rho = \gamma\, \rho_d + (1-\gamma)\rho_g, \qquad \rho_d = \theta\, \rho_l + (1-\theta)\rho_S,$$

$$k_{eff} = \gamma\, k_d + (1-\gamma)k_g, \quad k_d = \theta\, k_l + (1-\theta)k_S,$$

$$C_{p_{eff}} = \gamma\, C_{p_d} + (1-\gamma)C_{p_g}, \quad C_{p_d} = \theta\, C_{p_l} + (1-\theta)C_{p_s}, \tag{5-17}$$

$$\mu = \gamma\, \mu_d + (1 - \gamma)\mu_g.$$

It has to be mentioned that the reliability of the developed numerical code to simulate two-phase (liquid—gas) problems was previously validated for the flattening of mm-sized hollow droplets on a substrate [107] and underwater bubble implosion [35].

5.2.2 Numerical domain and boundary conditions

These equations are solved in a 2D axisymmetric domain. The size characteristics and boundary conditions of this domain are shown in Figure 5-3.

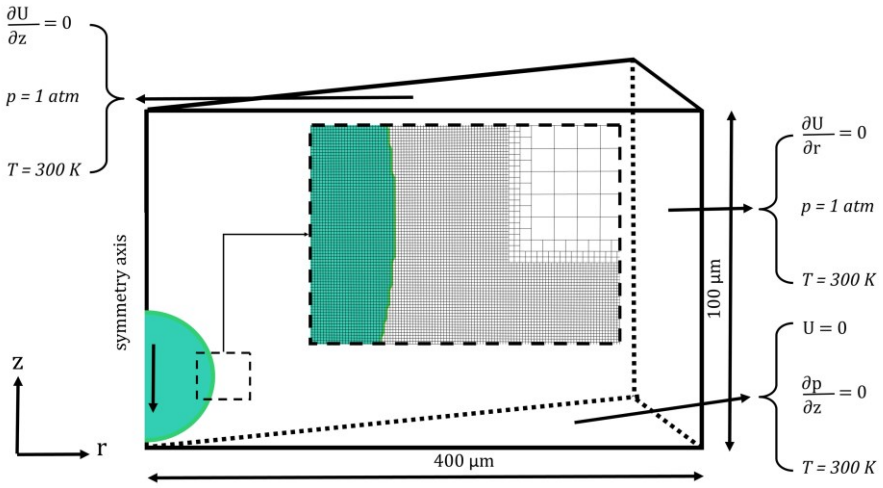

Figure 5-3. Schematic of the numerical domain.

The domain includes a total number of 2.0 million cells. Cells with different sizes are used at different locations inside the domain, and the size of the meshes are refined close to the areas that may contain liquid-gas interaction. The size of the mesh must be small enough to capture droplet overspreading. However, the mesh size is limited by the Knudson number criterion. Therefore, the smallest size of the mesh is chosen to be 120 nm which is large enough to satisfy the Knudson number criterion for continuum flow.

5.2.3 Desorption consideration

Three cases are simulated, the first case with the substrate at $T = 700$ K (hot surface), the second case with the substrate at room temperature $T = 300$ K without desorption, and the third case, with the substrate at room temperature $T = 300$ K with desorption. It is assumed that the solidification does not occur on the surface of the substrate till the total desorption of

the adsorbed gas. Other initial conditions of cases are identical. The temperature of the surrounding gas is assumed to be $T = 300$ K [17]; its pressure is atmospheric pressure, and the contact angle of the liquid and the wall is 90 degrees. To simulate the effects of gas desorption in the third case, the boundary condition representing the substrate surface is modified to release gas into the domain as the droplet impacts the surface.

It has been reported that gas desorption from a surface occurs when the substrate temperature rises above room temperature [23, 59-61, 63-66]. Humidity is adsorbed in several monolayers at the substrate surface at room temperature that can reach a thickness between 2 and 10 nm corresponding to mass density of $0.2 - 0.7\ \mu g/cm^2$ on metallic surface [65]. This adsorbed humidity layer can easily be heated by the impacting high-temperature droplet ($T = 3000\ K$), which leads to rapid desorption of the humidity in the form of gas from the surface.

Knowing this, the location of the rim of the molten droplet spreading on the substrate is used to trigger the gas desorption. In this study, it is assumed that when the droplet rim reaches a specific cell on the substrate, the cell's temperature increases high above the transient temperature and initiates the gas desorption. At this point, this cell ejects gas into the computation domain. To do so, it is assumed that when the droplet rim reaches a cell, the cell releases gas with the mass of $0.4\ \mu g/cm^2$ with a velocity of $U = 0.05\ m/s$ (gas desorption velocity) normal to the substrate surface for a time. After this point, the cell on the substrate reforms to a wall cell again with a contact angle of 90 degrees. In the current study, the amount of adsorbed gas layer is varied from $0.0125\ to\ 0.4\ \mu g/cm^2$.

It has been reported that water vapor is adsorbed on the substrate surface and desorbs when the temperature increases [55, 65]. However, to simplify the numerical modeling of the problem, it is assumed that the desorbed gas is in the form of environment gas which exists in the domain. Figure 5-4 represents a schematic of droplet rim tracking, which leads to the gas desorption from the surface at the periphery of the flattening droplet. The gas desorption starts from the first contact point of the droplet and substrate and moves as the droplet flattens on the surface. It should be mentioned that the width of the gas desorption zone which is shown in figure 4 is just a schematic of the numerical procedure. In the current study, the width of the gas desorption zone varies depending on the spreading velocity of the droplet, and the width of the gas desorption zone is determined by the velocity of the molten droplet rim spreading on the surface, considering the constant desorbed mass from each cell

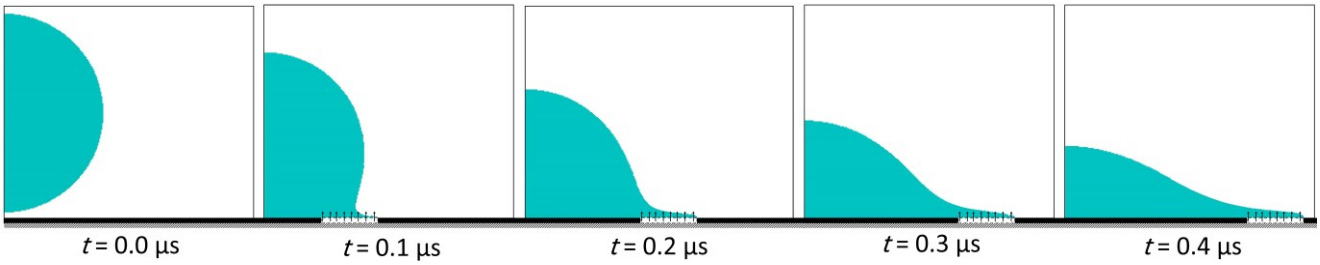

Figure 5-4. Schematic of the gas desorption during the droplet spreading.

The thermal contact resistance between the droplet and substrate is set to zero while the substrate surface is maintained at its initial temperature during the droplet flattening. In addition, it should be mentioned that the heat conduction inside the substrate is not considered in this simulation. These assumptions slightly overestimate the heat transfer rate to the substrate affecting the accuracy of the results for the solidification part. Nevertheless, its influence on the flow of the molten material at the periphery of the droplet is negligible.

A yttria-stabilized zirconia (YSZ) molten particle with the diameter of $D = 50\,\mu m$ is considered as the impacting droplet, and its properties are reported in Table 5-1. The velocity of the droplet before impact is $U = 100\,m/s$ and the temperature of the droplet is $T = 3000$ K.

Table 5-1 Material properties of YSZ and gas [17].

Properties	**Values**	**Properties**	**Values**
Solidus temperature (YSZ)	2949 K	Thermal conductivity (liquid YSZ)	$2\,W/(m.K)$
Liquidus temperature (YSZ)	2951 K	Latent heat of fusion (YSZ)	$7.07 * 10^5\,J/kg$
Density (liquid YSZ)	$5700\,kg/m^3$	Specific heat capacity (YSZ)	$713\,J/(kg.K)$
Density (solid YSZ)	$5890\,kg/m^3$	Thermal conductivity (gas)	$0.0242\,W/(m.K)$
Surface tension	$0.43\,N/m$	Viscosity (gas)	$1.78 * 10^{-5}\,kg/(m.s)$
Viscosity (YSZ)	$0.021\,kg/(m.s)$	Density (gas)	$5890\,kg/m^3$
Thermal conductivity (solid YSZ)	$2.32\,W/(m.K)$	Specific heat capacity (gas)	$1006.4\,J/(kg.K)$

5.3 Results and discussion

5.3.1 Effects of the substrate temperature without the gas desorption on the splat formation

Before considering the adsorption/desorption hypothesis, numerical simulations were performed to study the effect of the surface temperature on the flattening of the droplet (cases 1 and 2). Simulations were performed considering two surfaces, one held at $T = 700$ K and the other at $T = 300$ K without desorption. Figure 5-5 shows snapshots of droplet flattening on substrates with different temperatures without any gas desorption.

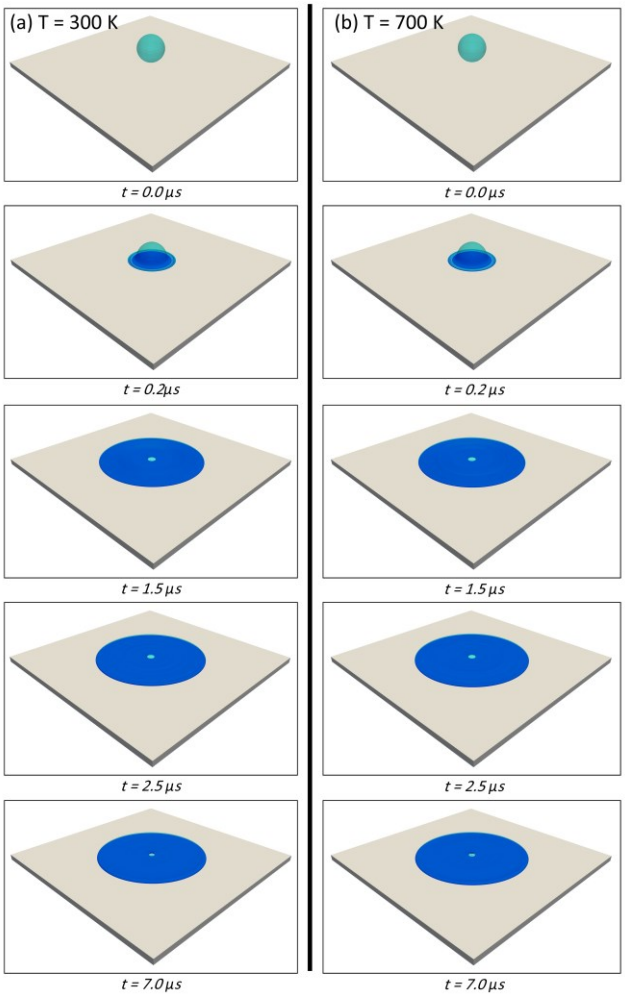

Figure 5-5. Snapshots of droplet flattening (grey) on a substrate.
(a) substrate at $T = 300$ K (No desorption) (b) substrate at $T = 700$ K. The turquoise color shows the droplet which has no contact with the surface while the blue color shows the area with a good connection between the droplet and the surface.

When a molten particle (turquoise) impacts a substrate, it spreads on the surface due to the high kinetic energy of the droplet. Although a small bubble entrapment is observed right beneath the impact location, the rest of the spreading droplet has good contact with the surface of the substrate at both temperatures, which is shown in Figure 5-5 in blue. When a droplet impacts a surface, a small portion of air entraps underneath the droplet that cannot be washed off by the liquid inertia due to the axisymmetric definition of the problem. This trapped air compresses as the liquid spreads on the surface until a point that the pressure of the liquid above this bubble decreases. At this point, the bubble expands and regarding the droplet impact velocity and droplet material, it can explode and make a hole inside the splat. The good contact area extends with the droplet flattening until the droplet reaches its maximum spreading diameter, which is about four times the initial droplet diameter. As a result, disk splats are formed on both surfaces. Based on Figure 5-5, the hydrodynamic behaviors of a molten particle during impact on surfaces with different temperatures are very similar. However, the formation of a disk splat on a substrate at room temperature contradicts the reported data of previous experimental studies [23, 28, 55, 57, 127-131].

Figure 5-6 shows snapshots of the cross-section of droplet flattening and solidification on substrates held at different temperatures without any gas desorption. The images in the inserts are stretched in the z-direction to provide a better resolution of the thin spreading film. The turquoise-colored area shows the molten portion of the droplet, while the black areas are the solidified ones. Compared to Figure 5-5, similar flattening behavior of the droplet can be observed in Figure 5-6. In addition, the solidification of the droplet on both surfaces shows that there is no significant difference between the solidification rates of these two cases. This means that the thermal contact resistance between the droplet and each surface is similar. Moreover, measurements of the final solidified splats of the numerical simulations show that the size of the solidified splat on the surface held at $T = 300$ K is almost equal to the size of the solidified splat on the surface held at $T = 700$ K. However, based on the reported experimental investigations, the thermal contact resistance between the droplet and the surface held at $T = 300$ K is significantly higher compared to that held at $T = 700$ K. Experiments on the formation of fragmented splats have shown that the size of the solidified core on the surface held at $T = 300$ K is almost half of the size of the solidified splat on the surface held at $T = 700$ K [23]. Therefore, the similar thermal contact resistance between the droplet and the surface and the similar solidified core observed for both cases in the numerical simulations violate the reported experimental data.

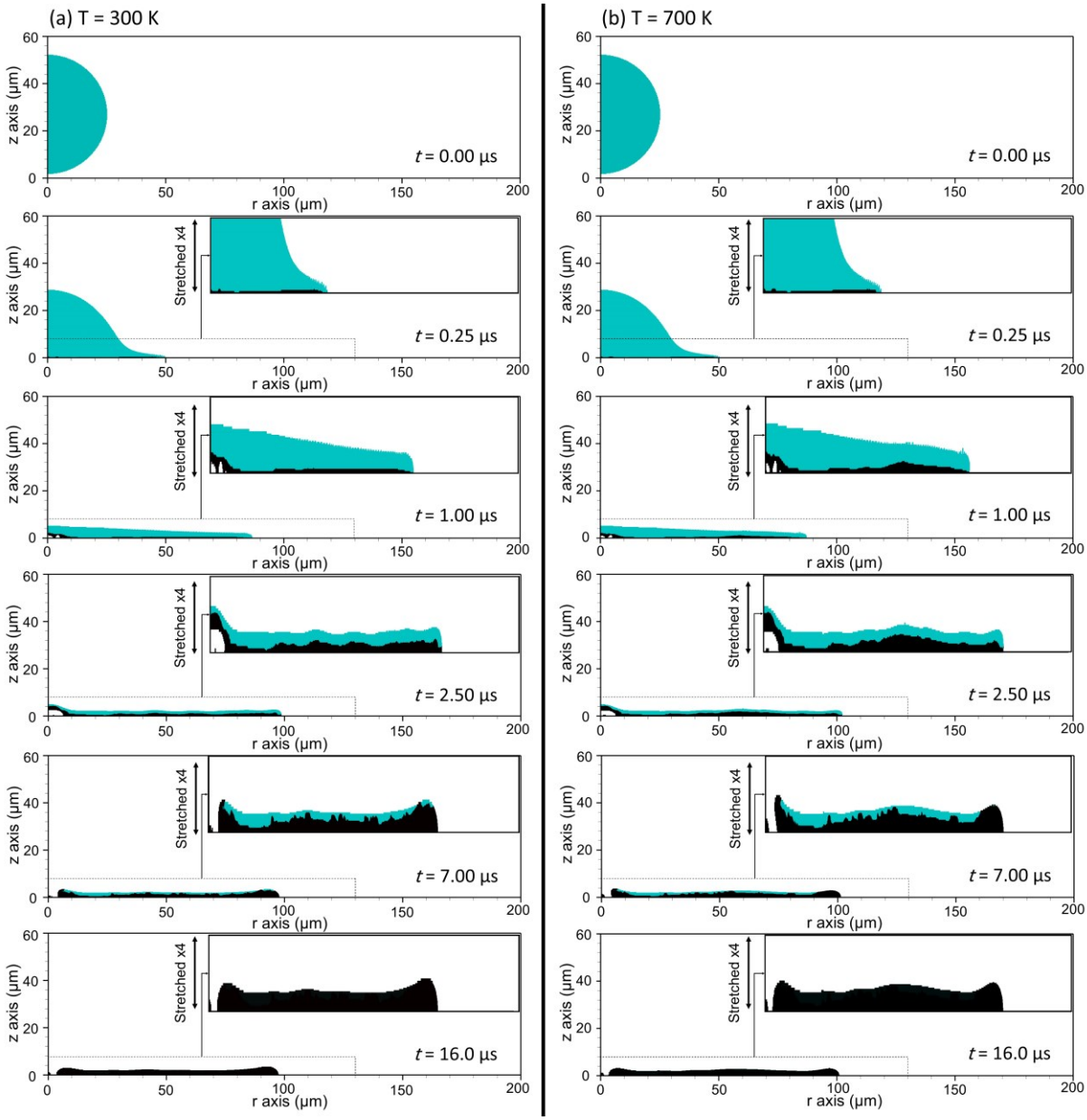

Figure 5-6. Snapshots of droplet flattening on the substrate at different temperatures.
(a) substrate at $T = 300$ K (No desorption) (b) substrate at $T = 700$ K. The contour shows solid-liquid volume fraction on the surface of the substrate. The turquoise color represents the liquid part, while black shows the solidified part. (Area close to the substrate is shown in a box on the top-right of each time step. This area is stretched four times in the z-direction)

The evolution of the spreading diameter of a molten particle on a hot and cold surface without gas desorption is shown in Figure 5-7.a. As the droplet impacts on a substrate, it flattens till it reaches its maximum spreading diameter. In the absence of solidification, the droplet recoils after reaching its maximum spreading diameter. In contrast, in the presence of solidification, the interface of the liquid and the surface solidifies and holds the spreading diameter of the droplet close to the maximum spreading diameter, as shown in Figure 5-7.a. Spreading

diameters of the droplet during impact show that the flattening of a droplet on both surfaces (with no desorption) is almost the same (Figure 5-7, $T = 700$ K [green symbols] and $T = 300$ K [black symbols]). No overspreading is observed during droplet flattening on either of the surfaces, which is against what was expected from the reported experimental data [23]. To study the numerical simulation mesh independence, droplet impact on a substrate held at $T = 300$ K is simulated with different numbers of cells (Figure 5-7.b), which shows that the spreading diameter deviation is negligible for simulations performed with different numbers of cells.

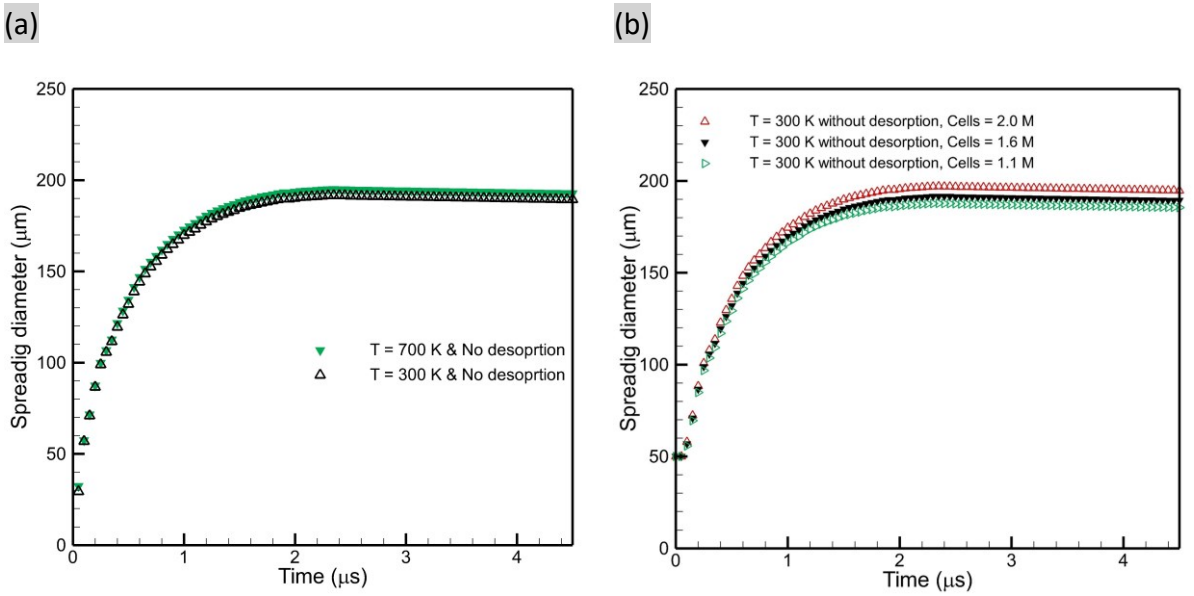

Figure 5-7. Spreading diameter of the droplet after impact on a surface.
(a) Substrate temperature held at $T = 700$ K (green) and $T = 300$ K with no desorption (black). (b) Surface held at $T = 300\ K$ with different number of domain cells.

To conclude this section, it should be noted that four differences are observed between the numerical simulations of droplet flattening and solidification on the cold substrate (no gas desorption involved) and the previously published experimental data. These differences are as follows: 1) absence of droplet overspreading, 2) good contact between the droplet and the surface, 3) low thermal contact resistance between the droplet and the surface, and 4) presence of the disk splat on the surface held at room temperature. These differences prove that the effect of substrate temperature alone cannot justify the fragmented splat phenomenon. Hence, in the next step, numerical simulations are performed to study the effects of gas desorption on the formation of splats (case 3). Considering the similarity between the numerical results of droplet impact on the surface with different temperatures (no gas desorption considered), the results of the numerical simulation for droplet impact on a surface held at $T = 300$ K (with gas

desorption) are compared with numerical results of droplet impact on a surface held at $T = 300$ K (without gas desorption).

5.3.2 Effects of the gas desorption on the splat formation

Figure 5-8 shows snapshots of droplet flattening on substrates at $T = 300$ K without gas desorption (Figure 5-8.a) and with gas desorption (Figure 5-8.b). As already discussed, during the droplet flattening on a surface without gas desorption, the droplet is in good contact with the surface, shown in blue in Figure 5-8.a. This good-contact area grows with the droplet flattening until the droplet reaches its maximum spreading. However, when the molten particle impacts a substrate with gas desorption (Figure 5-8.b), it behaves differently. As the droplet flattens on the surface with gas desorption, the good-contact area grows up to a diameter slightly larger than the initial droplet size. Beyond that point, the droplet continues to flatten, but the liquid is no more in contact with the substrate surface.

In the non-contact area, the dissipation of the spreading droplet momentum decreases as the velocity gradient normal to the substrate becomes negligible. Without detachment, the liquid velocity is zero at the substrate surface (non-slip assumption). Therefore, the spreading diameter of the droplet with gas desorption increases up to 8 times the initial droplet diameter (flattening ratio = 8). This means the spreading diameter with gas desorption is 2 to 3 times larger than that of the droplet on the surface without gas desorption. Furthermore, no liquid fragmentation is observed on the surface without gas desorption. In contrast, several fragmentation points are observed on the liquid sheet, moving above the substrate surface with gas description. The liquid sheet breakup prevents it from recoiling toward the center, and as a result, most of the liquid leaves the surface. Only a small portion remains on the surface, which eventually solidifies.

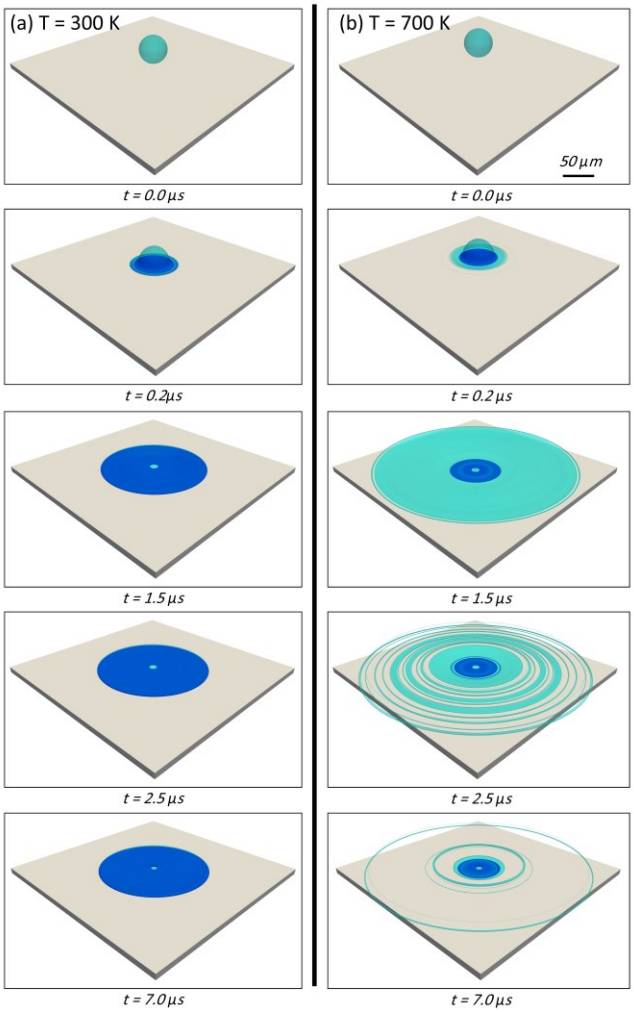

Figure 5-8. Snapshots of droplet flattening on a substrate.
(a) substrate at $T = 300$ K (No desorption) (b) substrate at $T = 300$ K (with a 0.4 $\mu g/cm^2$thick adsorbed gas layer). The turquoise color shows the droplet, which has no contact with the surface, while the blue color shows the area with a good connection between the droplet and the surface.

Figure 5-9 and Figure 5-10 present the snapshots of numerical simulations of the droplet impact on cold substrates with and without gas desorption. Figure 5-9 shows the cross section view of a flattening droplet, while Figure 5-10 shows the top view. As shown in Figure 5-9.a and Figure 5-10.a, following the droplet impact on the surface without gas desorption, the droplet spreads till it reaches a maximum extent and solidifies. No splat breakup or splashing is observed, which is typical of disk splats on hot surfaces. The diameter of the final solidified splat is almost equal to the maximum spreading of the droplet on the surface (Figure 5-9.a and Figure 5-10.a at $t > 10.0\ \mu s$) due to the high heat transfer rate of the flattened droplet and the surface. This represents good contact between the droplet and the surface. This high heat transfer rate

prevents the droplet from recoiling toward the center after reaching its maximum spreading diameter.

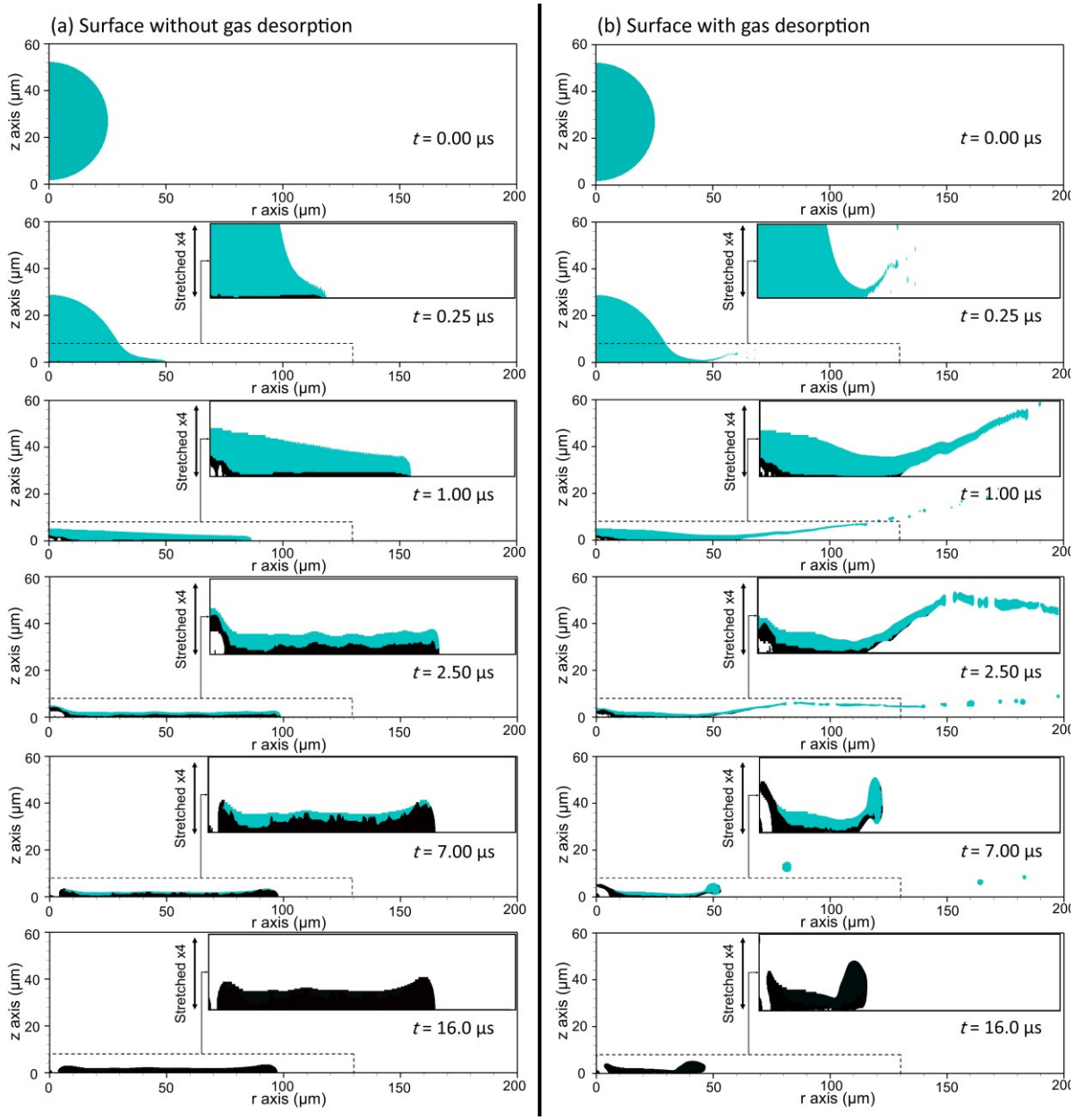

Figure 5-9. Snapshots of droplet flattening on the substrate at $T = 300$.
(a) No desorption (b) with 0.4 $\mu g/cm^2$ adsorbed gas layer. The turquoise color represents the liquid part, while black shows the solidified part. (The inserts offer a view stretched by a factor 4 in the z-direction)

On the other hand, in the case of the substrate with gas desorption (Figure 5-9.b and Figure 5-10.c), the detachment from the substrate of the spreading liquid is seen, and the spreading diameter of the droplet is much larger than that without gas desorption. Furthermore, as observed in Figure 5-10.c, the breakup on the liquid film is evident at $t = 2.7\ \mu s$ and results in the disintegration the overspreading droplet and disperse it far away from the location of impact. In the end, only a small solidified splat remains at the location of the droplet impact on

the substrate (Figure 5-9.b at $t = 16.0\ \mu s$ and Figure 5-10.b). These results are in agreement with the experimental data which were reported by McDonald et al. [23] for molten particle overspreading and fragmented splat formation (Figure 5-10.b, d).

In the case of droplet impact on a cold surface without desorption, the contact between the liquid and the substrate surface is good in all their interface. As a result, the rate of heat transfer is constant for this splat which is confirmed by the solidification progress in Figure 5-9.a (0.25-7.0 μs). However, in the case of gas desorption, two areas can be considered. One central area has contact with the surface and the area in which the liquid has no contact with the surface. The flying liquid area has no contact with the surface and the heat transfer only occurs between liquid and gas. As a result, the rate of heat transfer is low, and no solidification occurs. In the central core which has contact with the surface, the liquid solidifies. Nevertheless, solidification progress for cases with and without gas desorption shows that the rate of heat transfer in the case with gas desorption Figure 5-9.b (0.25-7.0 μs) is lower compared to the case without gas desorption Figure 5-9.a (0.25-7.0 μs). This means the gas desorption reduces the interfacial heat transfer between the droplet and the surface even at the area in which the liquid has contact with the substrate.

There are some differences in the breakup patterns of the liquid film observed numerically and experimentally as seen in Figure 5-10.c and Figure 5-10.d, respectively. Experimentally, the liquid film extends close to its maximum diameter before the liquid breaks initially close to the impact point (as indicated by the white arrow) and then in locations that appear randomly distributed on the liquid film as shown in images captured after 2.7 and 6.6 μs after impact. It is worth mentioning that the liquid film, detached from the substrate, is less than 0.5 μm thick when it starts to break [138] and holes are likely formed at locations where the film is randomly thinner or around some inclusions. As mentioned above, in the numerical results, the breaking of the liquid film occurs differently. Indeed, the film is already broken at $t = 2.7\ \mu s$ in several rims that continue expanding with time. This large number of rims results from instabilities that induce the film breaking as discussed below. Additionally, our model being 2D axisymmetric, cannot reproduce the breaking of the liquid in random locations as observed experimentally.

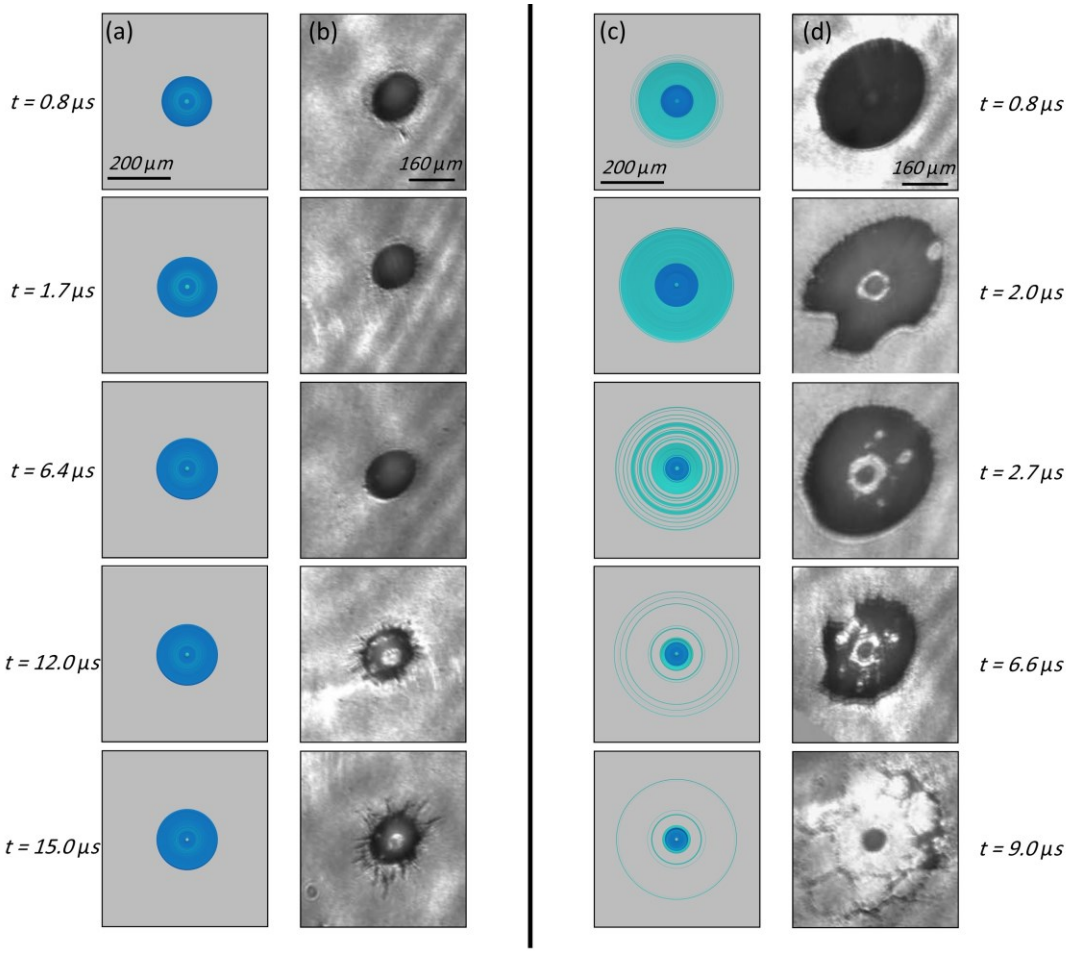

Figure 5-10. Top view of the droplet impact on a substrate.
(a) numerical simulation of surface without desorption, (b) experimental images of surface without desorption (the substrate temperature was maintained at 400°C) [23], (c) numerical simulation of the surface with desorption (containing $0.4\,\mu g/cm^2$ adsorbed gas film layer), (d) experimental images of surface with desorption [23]. The turquoise color represents the liquid part, while blue shows the area of the substrate which is in good contact with the liquid.

Furthermore, the comparison of the numerical results for both cases shows that the solidification of the splat on the surface without gas desorption (Figure 5-9.a at $t = 7.0\,\mu s$) occurs faster compared to that with gas desorption (Figure 5-9.b at $t = 7.0\,\mu s$). This shows lower heat transfer between the droplet and the substrate on the cold substrate with gas desorption. This lower heat transfer implies poor contact between the splat and the surface of the substrate, which has been reported previously [61].

The spreading diameter of a droplet after impact on the cold surface with and without desorption is presented in Figure 5-11.a. As a droplet impacts a surface without desorption, it flattens until it reaches its maximum spreading diameter. Without significant solidification, the droplet slightly recoils after reaching its maximum spreading diameter. In contrast, in the

presence of solidification, the interface of the liquid and the surface solidifies and holds the spreading diameter of the droplet close to the maximum spreading diameter. In the case of the droplet impact on the surface with gas desorption, the behavior of the droplet is similar to that of the droplet spreading on a surface without gas desorption only in the first 0.5 μs after impact in which the slope of the spreading diameter vs. time is the same.

Nevertheless, after 0.5 μs of the impact, the droplet behavior differs depending on the impact surface. Even though the droplet reaches its maximum spreading diameter on the surface without desorption at 1.0 μs, the spreading diameter of the droplet on the surface with gas desorption increases at the same rate. This is due to the droplet lift-off from the surface during spreading, leading to a liquid sheet formation above the surface. This spreading continues till the breakup of the liquid sheet.

To study the numerical simulation mesh independence, droplet impact on a substrate held at $T = 300$ K with gas desorption is simulated with different numbers of cells (Figure 5-11.b). It is observed that the spreading diameter of the droplet simulated by coarse mesh is smaller compared to the cases with fine meshes. However, the spreading diameter deviation for simulations using 2.0 M and 1.6 M cells is negligible.

(a) (b)

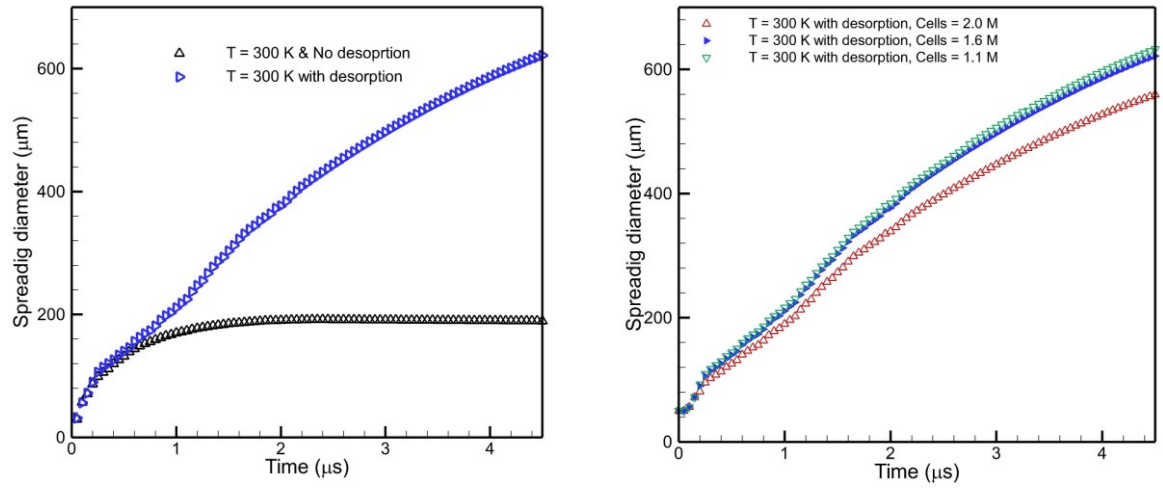

Figure 5-11. The spreading diameter of the droplet after impact.
(a) on a surface without desorption (black) and with desorption (blue). The amount of adsorbed gas film layer is 0.4 $\mu g/cm^2$. The spreading diameter for blue symbols is calculated based on the distance between the impact location and the tip of the spreading droplet times 2, including disintegrated liquid. (b) on a surface held at $T = 300\ K$ with different number of domain cells.

Figure 5-12 shows the initial timesteps of the impact of a droplet on the cold substrate. As the droplet flattens on the surface, it increases the substrate temperature and desorbs the adsorbed

gas. It is assumed that the gas is absorbed as a thin film layer with an amount of 0.4 $\mu g/cm^2$ on the substrate surface. When the molten particle impacts the surface, it flattens, and the velocity of the tip of the spreading liquid increases to around 200 m/s. Meanwhile, a pressure wave is formed in the ambient air. This wave accelerates the adjacent gas magnificently. This high velocity produces a high-vorticity region at the liquid and gas interface, leading to considerable shear stress tending to lift the liquid from the surface (Figure 5-12.c). In the meantime, the adsorbed gas is desorbed at the interface of the liquid and the surface. This desorbed gas is compressed by the high pressure of the droplet impact. At one point, the pressure of the compressed gas becomes higher than the pressure of the spreading liquid (Figure 5-12.b), which lifts the tip of the spreading droplet from the surface in the shape of a liquid film.

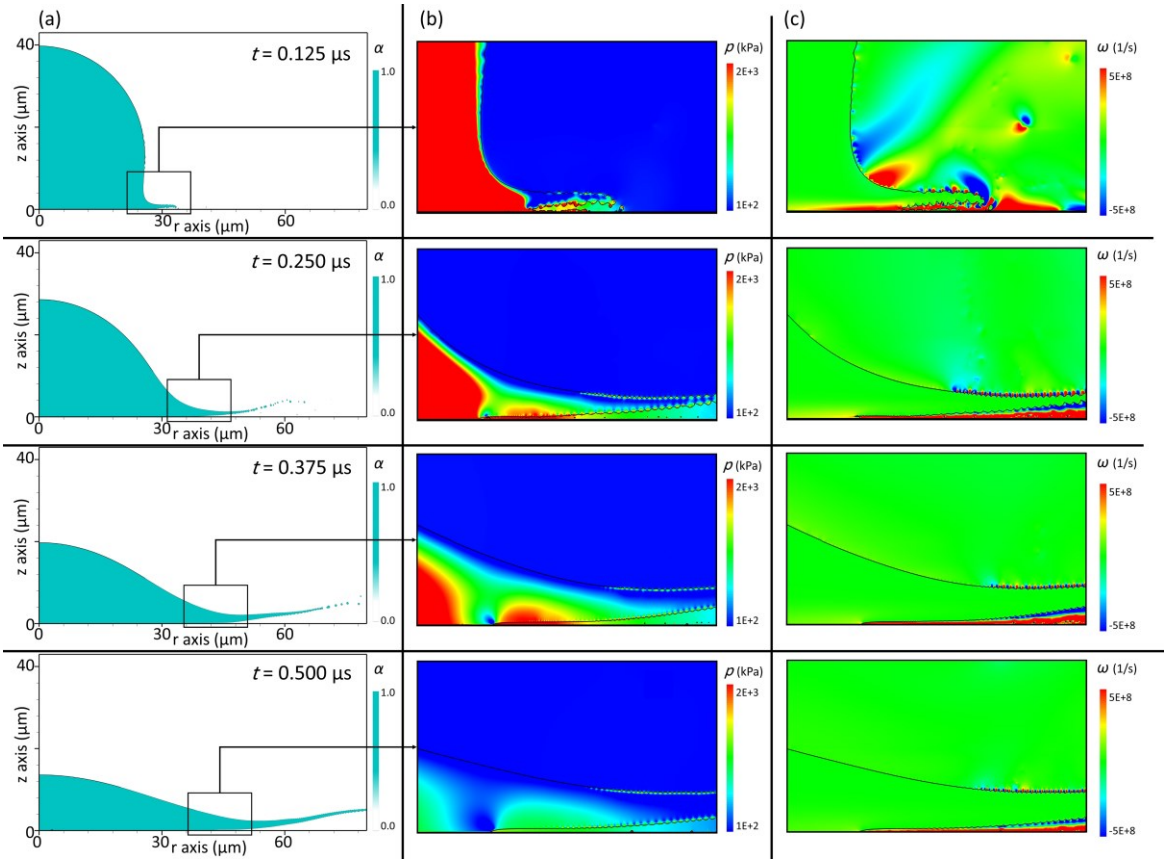

Figure 5-12. Snapshots of droplet cross-section during initial times after impact on the substrate at $T = 300$ K with an adsorbed gas film layer of 0.4 $\frac{\mu g}{cm^2}$.

(a) liquid-gas volume fraction contour (b) pressure contour with focus on the contact location of the liquid and the surface (c) vorticity contour with an emphasis on the contact location of the liquid and the surface.

In addition, this compressed gas produces a high-pressure layer between the liquid and the surface (Figure 5-12.b). As the droplet flattens, this layer extends and leads to the overspreading of the droplet in the shape of a flying liquid film. In addition, the presence of this layer acts

like an isolation layer which reduces heat transfer between the spreading droplet and the surface. This reduction in the heat transfer rate was reported in the previous studies on the droplet impact on the cold substrates [23] [138]. It should be mentioned that Kelvin—Helmholtz instabilities are observed on the interface of the flying film (Figure 5-12, Figure 5-13). These instabilities are a result of the velocity difference between the liquid and the gas during droplet impact and spreading. The amplitude of these instabilities grows as the liquid film flies over the surface.

The thin liquid film breaks up at a point and disperses around the impact location. Two types of breakups are captured by numerical simulations, including the breakup at the tip of the liquid film (Figure 5-13) and the disintegration of the liquid film from the center (Figure 5-14). During the droplet overspreading, the tip of the liquid film spreads with high velocity (Figure 5-13.c). Simultaneously, perturbations are imposed on the surface of the liquid film (Figure 5-13.b) due to the velocity difference between the liquid and the gas. These instabilities grow with the liquid film spreading. Similar to the breakup of the liquid jets [86, 139], the liquid film breaks up when the amplitude of these instabilities reaches the thickness of the liquid film (Figure 5-13.b, c). The breakup occurs at the tip of the detached liquid film and repeats till the total disintegration of the liquid film.

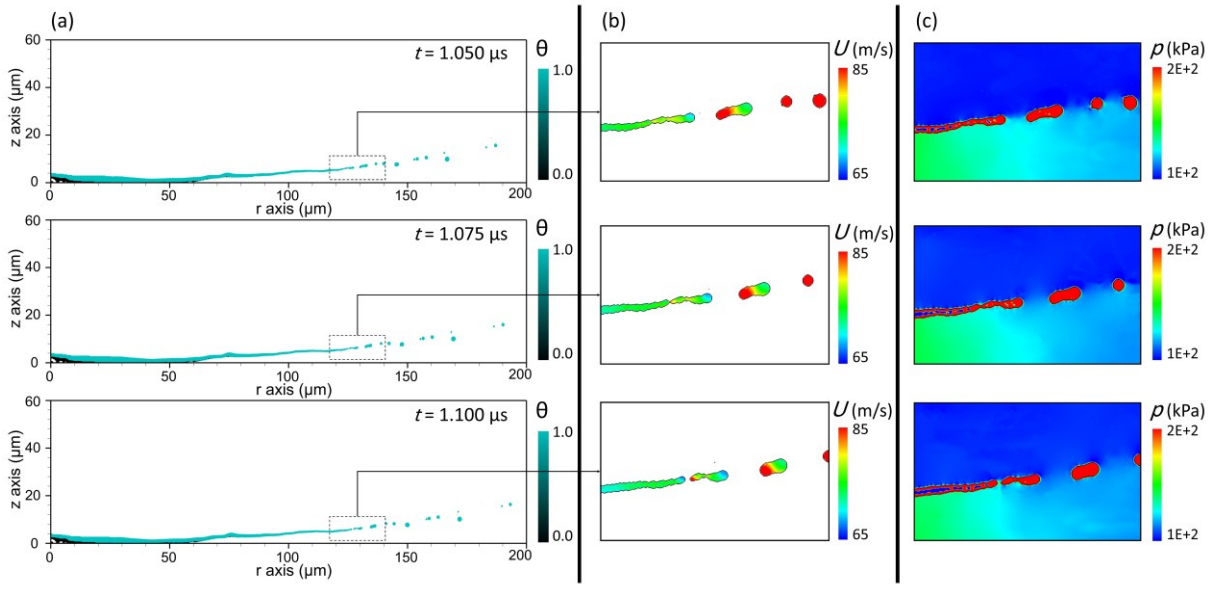

Figure 5-13. Snapshots of the cross-section of liquid film detachment and breakup after the droplet impact on a surface at $T = 300$ K, containing 0.4 $\mu g/cm^2$ adsorbed gas film layer.

(a) liquid-solid volume fraction contour (b) velocity contour of detached liquid with focus on the breakup point (c) pressure contour of detached liquid with focus on the breakup point.

The total disintegration of the liquid film is the other type of breakup captured (Figure 5-14). As the liquid film flies over the surface, it becomes thinner, and its velocity decreases. A velocity gradient is observed along with the liquid film (Figure 5-14.c), which causes the disintegration of the film from several points (Figure 5-14.b). After the film disintegration, a portion of the film, which is still connected to the central core, recoils toward the center, while the other disintegrated portions continue to move far away from the center. Regarding the velocity difference, each portion reaches a specific distance from the center, which produces splashing splats.

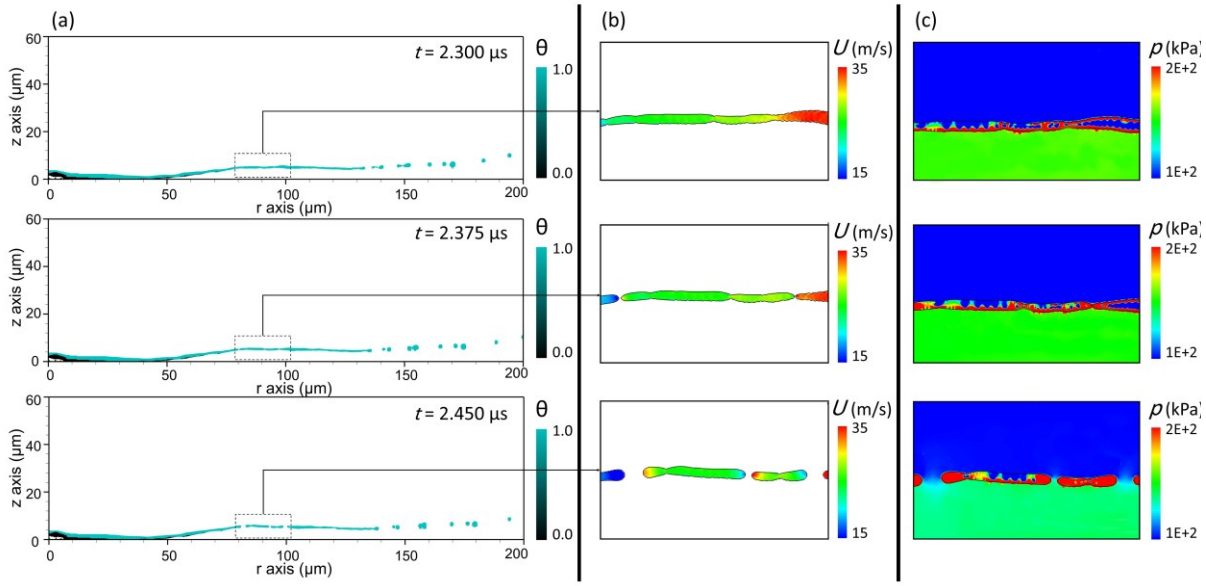

Figure 5-14. Snapshots of the cross-section of liquid film detachment and disintegration after the droplet impact on a surface at $T = 300$ K, containing 0.4 $\mu g/cm^2$ adsorbed gas film layer.
(a) liquid-solid volume fraction contour (b) velocity contour of detached liquid with focus on disintegration points (c) pressure contour of detached liquid with focus on disintegration points.

The effect of the amount of desorbed gas on the final spreading diameter of the remaining solidified splat is investigated in Figure 5-15. It is observed that the final splat is affected even when a small amount of the adsorbed gas ($0.0125\ \mu g/cm^2$) is considered. Actually, the splat diameter reduces from around 200 µm without desorption to 100 µm when the adsorbed gas layer reaches $0.1\ \mu g/cm^2$. For larger amount of adsorbed gas layer, the final diameter doesn't change anymore.

As mentioned, humidity is the main adsorbent on the surface of a substrate held at room temperature. When a hot particle impacts the surface, the humidity desorbs as gas, leading to the formation of fragmented splats. As it was observed, the minimum amount of desorbed gas

which is necessary to form the fragmented splat is $0.1\ \mu g/cm^2$. Considering an average distance between water molecule of 0.31 nm [140], the adsorption of only three monolayers of the water on the substrate surface can cause a full detachment of the liquid film form the substrate leading to splat fragmentation.

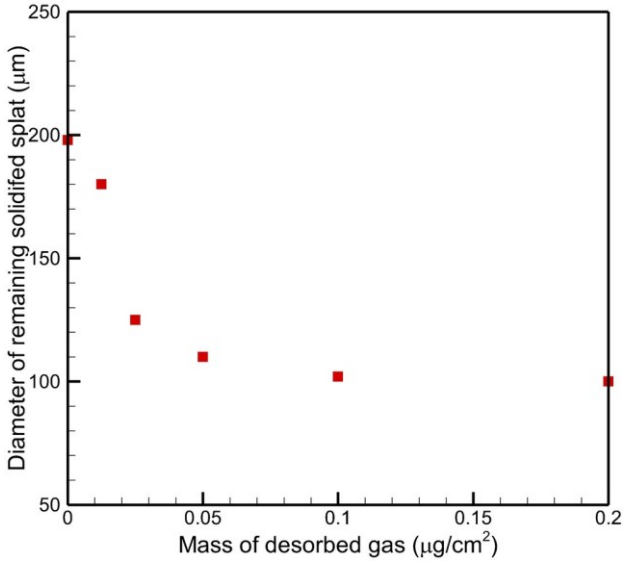

Figure 5-15. Diameter of remaining solidified splat after droplet impact on the surface held at $T = 300$ K with different mass of the adsorbed gas.

When a droplet impacts a surface, it flattens due to the droplet's high pressure at the impact location. The energies stored in a droplet before the impact on a surface are the droplet kinetic and surface energy. A portion of these energies dissipates through the viscosity of liquid and contact between the droplet and the surface, while the rest is stored in the droplet as the surface energy. The spreading diameter of the droplet depends on the ratio of the energy that disperses through viscosity to the spreading droplet surface energy. This ratio is the critical parameter to explain the overspreading of the droplet on a substrate.

When a molten particle impacts a hot surface without gas desorption, it makes good contact with the surface during the spreading process. Hence, a large portion of energy is dissipated through the work of viscosity. The remaining energy is actually stored as surface energy of the expanding droplet up to its maximum spreading diameter. After reaching this point, the droplet tends to minimize its surface energy by recoiling toward its center.

Nevertheless, in the presence of the solidification, this recoiling is confined due to the solidification of the droplet on the surface. Therefore, the final solidified disk splat has a diameter close to the maximum spreading diameter. However, the energy equivalence for a droplet impacting on a surface held at room temperature is different.

It is believed that no chemical modification of the surface occurs when the pressure decreases or the temperature of the substrate increases, and desorption is the only possible physical change taking place on the surface. It is known that water and other substances can be adsorbed on a clean solid surface; the most common condensate is water from moisture [55]. Condensed volatiles vaporize as the temperature of the substrate grows. As the molten particle spreads, the surface of a substrate held at room temperature increases the temperature of the substrate and desorbs the adsorbed humidity in the form of gas. This released gas is compressed by the high pressure of the droplet impact, but it cannot change the liquid flow direction due to the droplet's rigorous pressure. When the droplet flattens over the surface, its pressure gradually decreases until a point at which the pressure of the droplet becomes lower than the pressure of the compressed gas (Figure 5-12.c). From this point, the compressed gas lifts the spreading tip from the surface and makes a barrier between the liquid and the surface (Figure 5-12.a, b). which reduces dissipation of energies due to the viscosity. The absence of dissipation through the viscosity allows the liquid to spread more in the shape of a thin film till it reaches its equilibrium with the surface energy or disintegrates.

Two types of film breakup are observed during the droplet overspreading. First, the liquid film breaks up from the tip of the spreading liquid, and second, the liquid film disintegrates from the center. As the droplet spreads further, the thickness of the liquid film decreases. At the same time, perturbations appear on the surface of the liquid film, which grows as the liquid film flows in the gas. When the magnitude of these perturbations reaches a value higher than the thickness of the liquid film, it breaks up the liquid film from the spreading tip (Figure 5-13). As the integrated liquid film flies over the surface, it becomes thinner, and its velocity decreases to a point where the liquid film disintegrates from several locations (Figure 5-14). Following this, a portion of the film, which is still connected to the central core, recoils toward the center and exchanges heat with the surface till it creates a small solidified splat. The other disintegrated portions of the liquid flow through the gas as independent liquid volumes and moved far from the center. Moreover, the compressed gas acts as an isolation layer that decreases the heat transfer between the droplet and the surface.

5.4 Conclusion

In this paper, a volume of fluid (VOF) based model is developed to undertake the flattening of a YSZ molten particle at plasma spraying conditions. Numerical simulations are focused on the study of droplet spreading, solidification, and splat formation on substrates at high ($T =$

700 K) and low temperatures ($T = 300$ K). Results are in agreement with the reported experimental data. Generally, a droplet flattens, solidifies, and produces a uniform disk-shaped splat after impacting a hot surface. However, there are differences in the behavior of the droplet impacting a cold surface. It is shown that the desorption of the gas, adsorbed on the surface of a cold substrate, leads to the overspreading of the droplet. The desorbed gas lifts the spreading droplet from the surface and makes a barrier between the liquid and the surface by producing a high-pressure region underneath the droplet. This barrier reduces viscous dissipation of the liquid with the surface and increases the spreading diameter of the droplet up to 2 times compared to the droplet spreading on surfaces without desorption. The overspreading phenomenon is followed by the disintegration of the splat on the cold surface. The droplet overspreading leads to the formation of an unstable thin liquid film above the surface of the substrate. This thin liquid film disintegrates during the overspreading of the droplet and prevents the film from recoiling toward the center. The disintegrated liquid film moves far from the surface, and only a small solidified core remains on the surface of the substrate. The humidity is the main adsorbent on the surface of a substrate held at room temperature. Considering our observations regarding the minimum amount of desorbed gas which is necessary to form the fragmented splat ($0.1\ \mu g/cm^2$) together with the average distance between water molecules (0.31 nm), it is concluded that the adsorption of only three monolayers of water on the substrate surface is enough to cause splat fragmentation.

6 Chapter Six: Conclusion and future work

6.1 Conclusion

The flattening of hollow droplets has been investigated comprehensively in the current study. We studied the influence of different parameters that may affect the hollow droplet characteristics after impact using experimental measurements and numerical modeling. Comparison of simulated images with photographs shows that the numerical analysis accurately predicts droplet shape during deformation. The results confirm that the main difference between the hollow and dense droplets is the formation of a counter-jet after the hollow droplet impact. Impacting a solid surface, the entrapped bubble in the hollow droplet deforms and breaks the droplet internally. Then, a counter jet forms due to the pressure gap inside the hollow droplet due to an entrapped bubble. The counter jet will detach from the droplet and leave the surface if its energy overcomes the potential and dissipation energy. Consequently, the bubble rupture induces disturbances on the surface of the liquid sheet, leading it to spread and disintegrate. As a result of the recoil toward the center, the liquid adopts the form of a doughnut.

As expected, the spreading diameter increases with droplet impact velocity increment, resulting from the higher kinetic energy of the droplet before impact. In addition, droplet impact velocity directly affects the counter-jet length. The counter-jet height grows as the droplet impact velocity increases. However, the counter-jet height rate change is the same almost for all velocities. Furthermore, an analytical expression is developed to estimate the hollow droplet maximum spreading on a surface using the most influential parameters. Predictions from this model were shown to be in good agreement with the experimental measurements over an extensive range of *We* and *Re* numbers. It has been shown that the maximum spreading diameter of the hollow droplet is almost 90% of the maximum spreading of the dense droplet with the same mass and impact velocity. Furthermore, the splat thickness of the hollow droplet is nearly half of the splat thickness of the dense droplet.

When a droplet collides on an angled surface, it spreads asymmetrically. In both hollow and dense droplets, this behavior is predicted. Besides, the counter-jet forms on an inclined surface, comparable to the effect of a hollow droplet on a horizontal surface. However, the surface inclination affects the counter-jet length. The counter-jet length decreases with the hollow droplet impact with constant velocity as the surface inclination increases. In fact, the size of the counter-jet jet is controlled by the velocity component that is normal to the surface. In addition, the tangential component of the hollow droplet velocity vector before impact imposes a tangential velocity on the counter-jet. As a result, the counter-jet forms parallel to the surface

In the end, a numerical simulation was performed to study the effect of surface gas desorption on the flattening of a molten particle followed by splat fragmentation. To do so, a volume of fluid (VOF) based model is developed to undertake the flattening of a YSZ molten particle at plasma spraying conditions. Numerical simulations are focused on the study of droplet spreading, solidification, and splat formation on substrates at high ($T = 700$ K) and low temperatures ($T = 300$ K). Results are in agreement with the reported experimental data. Generally, a droplet flattens, solidifies, and produces a uniform disk-shaped splat after impacting a hot surface. However, there are important differences in the behavior of the droplet impacting a cold surface. It is shown that the desorption of the gas, adsorbed on the surface of a cold substrate, leads to the overspreading of the droplet. The desorbed gas lifts the spreading droplet from the surface and makes a barrier between the liquid and the surface by producing a high-pressure region underneath the droplet. This barrier reduces viscous dissipation of the liquid with the surface and increases the spreading diameter of the droplet up to 2 times compared to the droplet spreading on surfaces without desorption. The overspreading phenomenon is followed by the disintegration of the splat on the cold surface. The droplet overspreading leads to the formation of an unstable thin liquid film above the surface of the substrate. This thin liquid film disintegrates during the overspreading of the droplet and prevents the film from recoiling toward the center. The disintegrated liquid film moves far from the surface, and only a small solidified core remains on the surface of the substrate. The humidity is the main adsorbent on the surface of a substrate held at room temperature. Considering our observations regarding the minimum amount of desorbed gas which is necessary to form the fragmented splat ($0.1\ \mu g/cm^2$) together with the average distance between water molecules (0.31 nm), it is concluded that the adsorption of only three monolayers of water on the substrate surface is enough to cause splat fragmentation. To our knowledge, this is the first time a numerical model is able to capture the influence of gas desorption on splat formation at room temperature. The numerical results are in agreement with the already published experimental observations.

6.2 Future works

Experimental and numerical study of millimeter-sized droplets has provided useful information for better understanding hollow droplet flattening on different surfaces. Nevertheless, more experiments are needed to investigate splat formation after the micrometer-sized hollow droplet impact. To do so, an ultra-high-speed camera is needed to capture micrometer-sized hollow

powder flattening and solidification regarding the short time of molten particle flattening and solidification. In addition, a relatively complex experimental setup is required to isolate and capture individual particle impact and flattening of on a virgin substrate surface.

Considering the numerical results for both millimeter and micrometer-sized droplets at room condition or thermal spray condition, it is shown that the developed numerical code can simulate droplet flattening and simulation, even in thermal spraying conditions with the presence of adsorbates. Nevertheless, more studies need to be done to modify the numerical code even more. In particular, a more detailed and precise model of gas desorption is required to enhance the precision of the numerical results.

The numerical simulations are primarily done in a 2D axisymmetric domain, while some of the phenomena in droplet flattening can only be seen in a 3D simulation. This was not possible due to the high computational cost of 3D simulations, especially for numerical simulation of surface gas desorption. In addition, conjugate heat transfer was ignored during the simulation of splat fragmentation which needs to be added to the code. Considering the surface gas desorption hypothesis, the gas desorption is due to substrate temperature evolution. However, in the numerical simulation, the gas desorption was simulated based on the moving rim of the droplet.

7 References

[1] A. M. Worthington, "XXVIII. On the forms assumed by drops of liquids falling vertically on a horizontal plate," *Proceedings of the royal society of London,* vol. 25, pp. 261-272, 1877.

[2] Y. Liu, M. Andrew, J. Li, J. M. Yeomans, and Z. Wang, "Symmetry breaking in drop bouncing on curved surfaces," *Nature communications,* vol. 6, p. 10034, 2015.

[3] C. Mundo, M. Sommerfeld, and C. Tropea, "Droplet-wall collisions: experimental studies of the deformation and breakup process," *International journal of multiphase flow,* vol. 21, pp. 151-173, 1995.

[4] C. D. Modak, A. Kumar, A. Tripathy, and P. Sen, "Drop impact printing," *Nature communications,* vol. 11, pp. 1-11, 2020.

[5] L. Wang, J. Feng, T. Dang, and X. Peng, "Dynamics of oil droplet impacting and wetting on the inclined surfaces with different roughness," *International Journal of Multiphase Flow,* vol. 135, p. 103501.

[6] M. Qin, C. Tang, S. Tong, P. Zhang, and Z. Huang, "On the role of liquid viscosity in affecting droplet spreading on a smooth solid surface," *International Journal of Multiphase Flow,* vol. 117, pp. 53-63, 2019.

[7] D. A. Burzynski and S. E. Bansmer, "Droplet splashing on thin moving films at high Weber numbers," *International Journal of Multiphase Flow,* vol. 101, pp. 202-211, 2018.

[8] S. Chandra and C. Avedisian, "On the collision of a droplet with a solid surface," *Proceedings of the Royal Society of London. Series A: Mathematical and Physical Sciences,* vol. 432, pp. 13-41, 1991.

[9] M. Pasandideh-Fard, Y. Qiao, S. Chandra, and J. Mostaghimi, "Capillary effects during droplet impact on a solid surface," *Physics of fluids,* vol. 8, pp. 650-659, 1996.

[10] M. Safavi and S. Nourazar, "Experimental, analytical, and numerical study of droplet impact on a horizontal fiber," *International Journal of Multiphase Flow,* vol. 113, pp. 316-324, 2019.

[11] R. Attarzadeh and A. Dolatabadi, "Numerical study of the effect of surface wettability on performance of the spray cooling process," *International Journal of Computational Methods and Experimental Measurements,* vol. 4, pp. 615-624, 2016.

[12] C. Shinan, D. Liang, S. Mengjie, and L. Mengyao, "Numerical investigation on impingement dynamics and freezing performance of micrometer-sized water droplet on dry flat surface in supercooled environment," *International Journal of Multiphase Flow,* vol. 118, pp. 150-164, 2019.

[13] E. Gelissen, C. van der Geld, M. Baltussen, and J. Kuerten, "Modeling of droplet impact on a heated solid surface with a diffuse interface model," *International Journal of Multiphase Flow,* vol. 123, p. 103173, 2020.

[14] R. A. Miller, "Thermal barrier coatings for aircraft engines: history and directions," *Journal of thermal spray technology,* vol. 6, p. 35, 1997.

[15] J. R. Davis, *Handbook of thermal spray technology*: ASM international, 2004.

[16] M. Friis, C. Persson, and J. Wigren, "Influence of particle in-flight characteristics on the microstructure of atmospheric plasma sprayed yttria stabilized ZrO2," *Surface and coatings technology,* vol. 141, pp. 115-127, 2001.

[17] H. Safaei, M. D. Emami, H. S. Jazi, and J. Mostaghimi, "Application of Compressible Volume of Fluid Model in Simulating the Impact and Solidification of Hollow Spherical ZrO 2 Droplet on a Surface," *Journal of Thermal Spray Technology,* vol. 26, pp. 1959-1981, 2017.

[18] F. N. Longo, N. F. Bader III, and M. R. Dorfman, "Hollow sphere ceramic particles for abradable coatings," ed: Google Patents, 1984.

[19] O. Solonenko, I. Gulyaev, and A. Smirnov, "Plasma processing and deposition of powdered metal oxides consisting of hollow spherical particles," *Technical Physics Letters,* vol. 34, pp. 1050-1052, 2008.

[20] P.-H. Gao, Y.-G. Li, C.-J. Li, G.-J. Yang, and C.-X. Li, "Influence of powder porous structure on the deposition behavior of cold-sprayed WC-12Co coatings," *Journal of Thermal Spray Technology,* vol. 17, pp. 742-749, 2008.

[21] O. P. Solonenko, A. V. Smirnov, and I. P. Gulyaev, "Spreading and solidification of hollow molten droplet under its impact onto substrate: computer simulation and experiment," in *AIP Conference Proceedings*, 2008, pp. 561-568.

[22] K. Shinoda and H. Murakami, "Splat morphology of yttria-stabilized zirconia droplet deposited via hybrid plasma spraying," *Journal of thermal spray technology,* vol. 19, pp. 602-610, 2010.

[23] A. McDonald, M. Lamontagne, C. Moreau, and S. Chandra, "Impact of plasma-sprayed metal particles on hot and cold glass surfaces," *Thin Solid Films,* vol. 514, pp. 212-222, 2006.

[24] J. Liu, H. Vu, S. S. Yoon, R. A. Jepsen, and G. Aguilar, "Splashing phenomena during liquid droplet impact," *Atomization and Sprays,* vol. 20, 2010.

[25] B. Derby, "Inkjet printing of functional and structural materials: fluid property requirements, feature stability, and resolution," *Annual Review of Materials Research,* vol. 40, pp. 395-414, 2010.

[26] M. Marengo, C. Antonini, I. V. Roisman, and C. Tropea, "Drop collisions with simple and complex surfaces," *Current Opinion in Colloid & Interface Science,* vol. 16, pp. 292-302, 2011.

[27] Y. Zhang, "Understanding the Formation Mechanism of Plasma-sprayed Ni and Ni20Cr Splats through Experimental and Numerical Study," ResearchSpace@ Auckland, 2018.

[28] A. Tran, M. Hyland, K. Shinoda, and S. Sampath, "Influence of substrate surface conditions on the deposition and spreading of molten droplets," *Thin Solid Films,* vol. 519, pp. 2445-2456, 2011.

[29] M. Fukumoto, K. Yang, K. Tanaka, T. Usami, T. Yasui, and M. Yamada, "Effect of substrate temperature and ambient pressure on heat transfer at interface between molten droplet and substrate surface," *Journal of thermal spray technology,* vol. 20, pp. 48-58, 2011.

[30] C. W. Visser, P. E. Frommhold, S. Wildeman, R. Mettin, D. Lohse, and C. Sun, "Dynamics of high-speed micro-drop impact: numerical simulations and experiments at frame-to-frame times below 100 ns," *Soft matter,* vol. 11, pp. 1708-1722, 2015.

[31] S. D. Aziz and S. Chandra, "Impact, recoil and splashing of molten metal droplets," *International journal of heat and mass transfer,* vol. 43, pp. 2841-2857, 2000.

[32] M. K. Tripathi, K. C. Sahu, and R. Govindarajan, "Dynamics of an initially spherical bubble rising in quiescent liquid," *Nature communications,* vol. 6, pp. 1-9, 2015.

[33] E. Villermaux and B. Bossa, "Single-drop fragmentation determines size distribution of raindrops," *Nature Physics,* vol. 5, pp. 697-702, 2009.

[34] J. Feng, M. Roché, D. Vigolo, L. N. Arnaudov, S. D. Stoyanov, T. D. Gurkov*, et al.*, "Nanoemulsions obtained via bubble-bursting at a compound interface," *Nature Physics,* vol. 10, pp. 606-612, 2014.

[35] H. Moezzi-Rafie and M. M. Nasiri, "An investigation on the flow physics of bubble implosion using numerical techniques," *Ocean Engineering,* vol. 153, pp. 185-192, 2018.

[36] J. T. Pham, M. Paven, S. Wooh, T. Kajiya, H.-J. Butt, and D. Vollmer, "Spontaneous jumping, bouncing and trampolining of hydrogel drops on a heated plate," *Nature communications,* vol. 8, pp. 1-9, 2017.

[37] S. Poulain and L. Bourouiba, "Biosurfactants change the thinning of contaminated bubbles at bacteria-laden water interfaces," *Physical Review Letters,* vol. 121, p. 204502, 2018.

[38] W. Chi, S. Sampath, and H. Wang, "Microstructure–Thermal Conductivity Relationships for Plasma-Sprayed Yttria-Stabilized Zirconia Coatings," *Journal of the American Ceramic Society,* vol. 91, pp. 2636-2645, 2008.

[39] C. W. Visser, D. N. Amato, J. Mueller, and J. A. Lewis, "Architected polymer foams via direct bubble writing," *Advanced materials,* vol. 31, p. 1904668, 2019.

[40] M. P. Stewart, R. Langer, and K. F. Jensen, "Intracellular delivery by membrane disruption: mechanisms, strategies, and concepts," *Chemical reviews,* vol. 118, pp. 7409-7531, 2018.

[41] P. A. Mountford, A. N. Thomas, and M. A. Borden, "Thermal activation of superheated lipid-coated perfluorocarbon drops," *Langmuir,* vol. 31, pp. 4627-4634, 2015.

[42] N. Rapoport, "Drug-loaded perfluorocarbon nanodroplets for ultrasound-mediated drug delivery," in *Therapeutic Ultrasound*, ed: Springer, 2016, pp. 221-241.

[43] P. S. Sheeran, Y. Daghighi, K. Yoo, R. Williams, E. Cherin, F. S. Foster*, et al.*, "Image-guided ultrasound characterization of volatile sub-micron phase-shift droplets in the 20–40 MHz frequency range," *Ultrasound in medicine & biology,* vol. 42, pp. 795-807, 2016.

[44] O. Solonenko, H. Nishiyama, A. Smirnov, H. Takana, and J. Jang, "Visualization of arc and plasma flow patterns for advanced material processing," *Journal of Visualization,* vol. 18, pp. 1-15, 2015.

[45] M. Bussmann, S. Chandra, and J. Mostaghimi, "Modeling the splash of a droplet impacting a solid surface," *Physics of fluids,* vol. 12, pp. 3121-3132, 2000.

[46] M. Pasandideh-Fard, S. Chandra, and J. Mostaghimi, "A three-dimensional model of droplet impact and solidification," *International Journal of Heat and Mass Transfer,* vol. 45, pp. 2229-2242, 2002.

[47] I. Gulyaev and O. Solonenko, "Hollow droplets impacting onto a solid surface," *Experiments in fluids,* vol. 54, p. 1432, 2013.

[48] I. Gulyaev, O. Solonenko, P. Y. Gulyaev, and A. Smirnov, "Hydrodynamic features of the impact of a hollow spherical drop on a flat surface," *Technical Physics Letters,* vol. 35, pp. 885-888, 2009.

[49] A. Kumar and S. Gu, "Modelling impingement of hollow metal droplets onto a flat surface," *International Journal of Heat and Fluid Flow,* vol. 37, pp. 189-195, 2012.

[50] A. Kumar, S. Gu, H. Tabbara, and S. Kamnis, "Study of impingement of hollow ZrO2 droplets onto a substrate," *Surface and Coatings Technology,* vol. 220, pp. 164-169, 2013.

[51] A. Kumar, S. Gu, and S. Kamnis, "Simulation of impact of a hollow droplet on a flat surface," *Applied Physics A,* vol. 109, pp. 101-109, 2012.

[52] Y. Wei and M.-J. Thoraval, "Maximum spreading of an impacting air-in-liquid compound drop," *Physics of Fluids,* vol. 33, p. 061703, 2021.

[53] X. Liu, Y. Wang, Z. Wang, H. Sun, and Y. Luan, "Numerical investigation of two hollow cylindrical droplets vertically impacting on dry flat surface simultaneously," *Physics of Fluids,* vol. 32, p. 113305, 2020.

[54] X. Liu, Y. Qu, Y. Wang, M. Wang, Z. Wang, and H. Sun, "Numerical analysis of two hollow drops simultaneously impacting a wet surface," *Physics of Fluids,* vol. 33, p. 043312, 2021.

[55] K. Yang, K. Tomita, M. Fukumoto, M. Yamada, and T. Yasui, "Effect of ambient pressure on flattening behavior of thermal sprayed particles," *Journal of thermal spray technology,* vol. 18, p. 510, 2009.

[56] M. Fukumoto, T. Yamaguchi, M. Yamada, and T. Yasui, "Splash splat to disk splat transition behavior in plasma-sprayed metallic materials," *Journal of Thermal Spray Technology,* vol. 16, pp. 905-912, 2007.

[57] K. Yang, M. Fukumoto, T. Yasui, and M. Yamada, "Role of substrate temperature on microstructure formation in plasma-sprayed splats," *Surface and Coatings Technology,* vol. 214, pp. 138-143, 2013.

[58] M. Qu and A. Gouldstone, "On the role of bubbles in metallic splat nanopores and adhesion," *Journal of thermal spray technology,* vol. 17, pp. 486-494, 2008.

[59] L. Bianchi, A. Leger, M. Vardelle, A. Vardelle, and P. Fauchais, "Splat formation and cooling of plasma-sprayed zirconia," *Thin Solid Films,* vol. 305, pp. 35-47, 1997.

[60] L. Bianchi, A. Denoirjean, F. Blein, and P. Fauchais, "Microstructural investigation of plasma-sprayed ceramic splats," *Thin solid films,* vol. 299, pp. 125-135, 1997.

[61] M. Fukumoto, Yang, K., Tanaka, K., Usami, T., Yasui, T., & Yamada, M. (). .,, "Effect of substrate temperature and ambient pressure on heat transfer at interface between molten droplet and substrate surface," *Journal of thermal spray technology,* vol. 20, pp. 48-58, 2011.

[62] K. Yang, M. Liu, K. Zhou, and C. Deng, "Recent developments in the research of splat formation process in thermal spraying," *Journal of Materials,* vol. 2013, 2012.

[63] Y. Zhang, M. Hyland, A. T. Tran, and S. Matthews, "Effect of substrates temperatures on the spreading behavior of plasma-sprayed Ni and Ni-20 wt.% Cr splats," *Journal of Thermal Spray Technology,* vol. 25, pp. 71-81, 2016.

[64] K. Yang, M. Fukumoto, T. Yasui, and M. Yamada., "Study of substrate preheating on flattening behavior of thermal-sprayed copper particles," *Journal of thermal spray technology,* vol. 19(6), 2010.

[65] S. Brossard, P. Munroe, A. Tran, and M. Hyland, "Study of the splat formation for plasma sprayed NiCr on aluminum substrate as a function of substrate condition," *Surface and Coatings Technology,* vol. 204, pp. 2647-2656, 2010.

[66] A. T. T. Tran, Hyland, M.M., Qiu, T., Withy, B. and James, B.J., , "Effects of surface chemistry on splat formation during plasma spraying," *Journal of Thermal Spray Technology,* vol. 17, pp. pp.637-645, 2008.

[67] R. Dhiman, McDonald, A. G., & Chandra, S. , "Predicting splat morphology in a thermal spray process," *Surface and Coatings Technology,* vol. 201, pp. 7789-7801, 2007.

[68] C. Moreau, P. Gougeon, and M. Lamontagne, "Influence of substrate preparation on the flattening and cooling of plasma-sprayed particles," *Journal of Thermal Spray Technology,* vol. 4, pp. 25-33, 1995.

[69] S. Sampath and H. Herman, "Rapid solidification and microstructure development during plasma spray deposition," *Journal of thermal spray technology,* vol. 5, pp. 445-456, 1996.

[70] C. J. Li, & Li, J. L. , "Evaporated-gas-induced splashing model for splat formation during plasma spraying," *Surface and Coatings Technology,* vol. 184, pp. 13-23, 2004.

[71] S. Miller, H. Jasak, D. Boger, E. Paterson, and A. Nedungadi, "A pressure-based, compressible, two-phase flow finite volume method for underwater explosions," *Computers & Fluids,* vol. 87, pp. 132-143, 2013.

[72] J. U. Brackbill, D. B. Kothe, and C. Zemach, "A continuum method for modeling surface tension," *Journal of computational physics,* vol. 100, pp. 335-354, 1992.

[73] J. D. Anderson and J. Wendt, *Computational fluid dynamics* vol. 206: Springer, 1995.

[74] H. Hashemi and C. Sliepcevich, "A numerical method for solving two-dimensional problems of heat conduction with change of phase," in *Chem. Eng. Prog. Symp. Series*, 1967, pp. 34-41.

[75] V. Voller and M. Cross, "An explicit numerical method to," *International Journal of Heat and Mass Transfer,* vol. 26, pp. 147-150, 1983.

[76] V. Voller, N. Markatos, and M. Cross, "TECHNIQUES FOR ACCOUNTING FOR THE MOVING INTERFACE IN CONVECTION/DIFFUSION PHASE CHANGE," in *Unknown Host Publication Title*, ed: Pineridge Press, 1985.

[77] F. Rösler and D. Brüggemann, "Shell-and-tube type latent heat thermal energy storage: numerical analysis and comparison with experiments," *Heat and mass transfer,* vol. 47, p. 1027, 2011.

[78] V. Voller, "Implicit finite—difference solutions of the enthalpy formulation of Stefan problems," *IMA journal of numerical analysis,* vol. 5, pp. 201-214, 1985.

[79] H. Liu, E. J. Lavernia, and R. H. Rangel, "Numerical simulation of substrate impact and freezing of droplets in plasma spray processes," *Journal of Physics D: Applied Physics,* vol. 26, p. 1900, 1993.

[80] M. Raessi, M. Thiele, and B. Amirzadeh, "Computational Simulation of the Impact and Freezing of Micron-Size Water Droplets on Super-Hydrophobic Surfaces," in *ASME 2013 Heat Transfer Summer Conference collocated with the ASME 2013 7th International Conference on Energy Sustainability and the ASME 2013 11th International Conference on Fuel Cell Science, Engineering and Technology*, 2013, pp. V002T07A032-V002T07A032.

[81] S. Alavi and M. Passandideh-Fard, "Numerical Simulation of Droplet Impact and Solidification Including Thermal Shrinkage in a Thermal Spray Process," in *2010 14th International Heat Transfer Conference*, 2010, pp. 731-739.

[82] V. R. Voller, M. Cross, and N. Markatos, "An enthalpy method for convection/diffusion phase change," *International journal for numerical methods in engineering,* vol. 24, pp. 271-284, 1987.

[83] M. Balla, M. K. Tripathi, and K. C. Sahu, "A numerical study of a hollow water droplet falling in air," *Theoretical and Computational Fluid Dynamics,* pp. 1-12, 2020.

[84] D. Li, D. Zhang, and Z. Zheng, "Numerical analysis of hollow droplet impacts on a dry flat surface," *International Journal of Heat and Mass Transfer,* vol. 129, pp. 753-763, 2019.

[85] S. Zhu, A. Kherbeche, Y. Feng, and M.-J. Thoraval, "Impact of an air-in-liquid compound drop onto a liquid surface," *Physics of Fluids,* vol. 32, p. 041705, 2020.

[86] M. R. Morad, M. Nasiri, and G. Amini, "Axis-switching and breakup of rectangular liquid jets," *International Journal of Multiphase Flow,* vol. 126, p. 103242, 2020.

[87] F. Yeganehdoust, R. Attarzadeh, I. Karimfazli, and A. Dolatabadi, "A numerical analysis of air entrapment during droplet impact on an immiscible liquid film," *International Journal of Multiphase Flow,* vol. 124, p. 103175, 2020.

[88] D. Richard, C. Clanet, and D. Quéré, "Surface phenomena: Contact time of a bouncing drop," *Nature,* vol. 417, p. 811, 2002.

[89] Y. Liu, L. Moevius, X. Xu, T. Qian, J. M. Yeomans, and Z. Wang, "Pancake bouncing on superhydrophobic surfaces," *Nature physics,* vol. 10, p. 515, 2014.

[90] T. Ma, L. Feng, H. Wang, H. Liu, and M. Yao, "A numerical study of spray/wall impingement based on droplet impact phenomenon," *International Journal of Heat and Mass Transfer,* vol. 112, pp. 401-412, 2017.

[91] M. A. Quetzeri-Santiago, K. Yokoi, A. A. Castrejón-Pita, and J. R. Castrejón-Pita, "Role of the dynamic contact angle on splashing," *Physical review letters,* vol. 122, p. 228001, 2019.

[92] D. Li, X. Duan, Z. Zheng, and Y. Liu, "Dynamics and heat transfer of a hollow droplet impact on a wetted solid surface," *International Journal of Heat and Mass Transfer,* vol. 122, pp. 1014-1023, 2018.

[93] P. B. Weisensee, J. Tian, N. Miljkovic, and W. P. King, "Water droplet impact on elastic superhydrophobic surfaces," *Scientific reports,* vol. 6, p. 30328, 2016.

[94] C. Hao, J. Li, Y. Liu, X. Zhou, Y. Liu, R. Liu*, et al.*, "Superhydrophobic-like tunable droplet bouncing on slippery liquid interfaces," *Nature communications,* vol. 6, p. 7986, 2015.

[95] S. Adera, R. Raj, R. Enright, and E. N. Wang, "Non-wetting droplets on hot superhydrophilic surfaces," *Nature communications,* vol. 4, p. 2518, 2013.

[96] P. García-Geijo, G. Riboux, and J. M. Gordillo, "Inclined impact of drops," *Journal of Fluid Mechanics,* vol. 897, 2020.

[97] E. S. Quintero, G. Riboux, and J. M. Gordillo, "Splashing of droplets impacting superhydrophobic substrates," *Journal of Fluid Mechanics,* vol. 870, pp. 175-188, 2019.

[98] J. M. Gordillo, G. Riboux, and E. S. Quintero, "A theory on the spreading of impacting droplets," *Journal of Fluid Mechanics,* vol. 866, pp. 298-315, 2019.

[99] M. Pegg, R. Purvis, and A. Korobkin, "Droplet impact onto an elastic plate: a new mechanism for splashing," *Journal of Fluid Mechanics,* vol. 839, pp. 561-593, 2018.

[100] D. Li, D. Zhang, Z. Zheng, and X. Tian, "Numerical analysis on air entrapment during a droplet impacts on a dry flat surface," *International Journal of Heat and Mass Transfer,* vol. 115, pp. 186-193, 2017.

[101] P. D. Hicks and R. Purvis, "Air cushioning and bubble entrapment in three-dimensional droplet impacts," *J Fluid Mech,* vol. 649, pp. 135-163, 2010.

[102] M. Tembely and A. Dolatabadi, "A comprehensive model for predicting droplet freezing features on a cold substrate," *Journal of Fluid Mechanics,* vol. 859, pp. 566-585, 2019.

[103] C.-H. Wang, S.-T. Kang, Y.-H. Lee, Y.-L. Luo, Y.-F. Huang, and C.-K. Yeh, "Aptamer-conjugated and drug-loaded acoustic droplets for ultrasound theranosis," *Biomaterials,* vol. 33, pp. 1939-1947, 2012.

[104] A. Jamaluddin, G. Ball, C. Turangan, and T. Leighton, "The collapse of single bubbles and approximation of the far-field acoustic emissions for cavitation induced by shock wave lithotripsy," *Journal of Fluid Mechanics,* vol. 677, pp. 305-341, 2011.

[105] T. Tran, H. de Maleprade, C. Sun, and D. Lohse, "Air entrainment during impact of droplets on liquid surfaces," *Journal of Fluid Mechanics,* vol. 726, 2013.

[106] S.-C. Zhao, R. de Jong, and D. van der Meer, "Formation of a hidden cavity below droplets impacting on a granular substrate," *Journal of fluid mechanics,* vol. 880, pp. 59-72, 2019.

[107] M. Nasiri, G. Amini, C. Moreau, and A. Dolatabadi, "Hollow droplet impact on a solid surface," *International Journal of Multiphase Flow,* p. 103740, 2021.

[108] M. M. Nasiri, A. Dolatabadi, and C. Moreau, "Modeling of liquid detachment and fragmentation during the impact of plasma spray particles on a cold substrate," *International Journal of Heat and Mass Transfer,* vol. 189, p. 122718, 2022.

[109] G. Amini, "A NONLINEAR MODEL FOR OSCILLATIONS OF A DROPLET IMPACTING A SOLID SURFACE," *Atomization and Sprays,* vol. 30, 2020.

[110] C. Josserand and S. T. Thoroddsen, "Drop impact on a solid surface," *Annual review of fluid mechanics,* vol. 48, pp. 365-391, 2016.

[111] S. T. Thoroddsen, T. G. Etoh, and K. Takehara, "High-speed imaging of drops and bubbles," *Annu. Rev. Fluid Mech.,* vol. 40, pp. 257-285, 2008.

[112] G. Liang and I. Mudawar, "Review of mass and momentum interactions during drop impact on a liquid film," *International Journal of Heat and Mass Transfer,* vol. 101, pp. 577-599, 2016.

[113] N. Zheng, B. Tong, G. Zhang, X. Hu, H. Liang, W. Wang*, et al.*, "Heat transfer characteristics of successive oil droplet impingement under minimum quantity lubrication," *Physics of Fluids,* vol. 33, p. 033318, 2021.

[114] T. Gilet and J. W. Bush, "Droplets bouncing on a wet, inclined surface," *Physics of Fluids,* vol. 24, p. 122103, 2012.

[115] J. Guo, S. Zou, S. Lin, B. Zhao, X. Deng, and L. Chen, "Oblique droplet impact on superhydrophobic surfaces: Jets and bubbles," *Physics of Fluids,* vol. 32, p. 122112, 2020.

[116] Y. Guan, J. Fu, S. Wu, X. Chen, and C. Zhou, "The post-impact dynamics of drop rebound on inclined hydrophobic surfaces of various wettabilities," *Physics of Fluids,* vol. 33, p. 072108, 2021.

[117] V. Bertola and M. Marengo, "Single drop impacts of complex fluids: a review," *Drops and Bubbles in Contact with Solid Surfaces,* pp. 267-298, 2012.

[118] B. Prunet-Foch, F. Legay, M. Vignes-Adler, and C. Delmotte, "Impacting emulsion drop on a steel plate: Influence of the solid substrate," *Journal of colloid and interface science,* vol. 199, pp. 151-168, 1998.

[119] J. López-Herrera, S. Popinet, and A. Castrejón-Pita, "An adaptive solver for viscoelastic incompressible two-phase problems applied to the study of the splashing of weakly viscoelastic droplets," *Journal of Non-Newtonian Fluid Mechanics,* vol. 264, pp. 144-158, 2019.

[120] C. W. Visser, T. Kamperman, L. P. Karbaat, D. Lohse, and M. Karperien, "In-air microfluidics enables rapid fabrication of emulsions, suspensions, and 3D modular (bio) materials," *Science advances,* vol. 4, p. eaao1175, 2018.

[121] M. R. Morad, M. Nasiri, and G. Amini, "Numerical Modeling of Instability and Breakup of Elliptical Liquid Jets," *AIAA Journal,* vol. 58, pp. 2442-2449, 2020.

[122] N. Laan, K. G. de Bruin, D. Bartolo, C. Josserand, and D. Bonn, "Maximum diameter of impacting liquid droplets," *Physical Review Applied,* vol. 2, p. 044018, 2014.

[123] Y. Huang, L. Jiang, B. Li, P. Premaratne, S. Jiang, and H. Qin, "Study effects of particle size in metal nanoink for electrohydrodynamic inkjet printing through analysis of droplet impact behaviors," *Journal of Manufacturing Processes,* vol. 56, pp. 1270-1276, 2020.

[124] S. Mohammadkhani, V. Jalilvand, B. Davis, F. B. Ettouil, A. Dolatabadi, L. Roue*, et al.*, "Suspension plasma spray deposition of CoxNi1-xO coatings," *Surface and Coatings Technology,* vol. 399, p. 126168, 2020.

[125] S. Mandre and M. P. Brenner, "The mechanism of a splash on a dry solid surface," *Journal of Fluid Mechanics,* vol. 690, pp. 148-172, 2012.

[126] L. Xu, W. W. Zhang, and S. R. Nagel, "Drop splashing on a dry smooth surface," *Physical review letters,* vol. 94, p. 184505, 2005.

[127] A. McDonald, C. Moreau, and S. Chandra, "Thermal contact resistance between plasma-sprayed particles and flat surfaces," *International Journal of Heat and Mass Transfer,* vol. 50, pp. 1737-1749, 2007.

[128] K. Shinoda, H. Murakami, S. Kuroda, S. Oki, K. Takehara, and T. G. Etoh, "High-speed thermal imaging of yttria-stabilized zirconia droplet impinging on substrate in plasma spraying," *Applied physics letters,* vol. 90, p. 194103, 2007.

[129] K. Shinoda, H. Murakami, S. Kuroda, K. Takehara, and S. Oki, "In situ visualization of impacting phenomena of plasma-sprayed zirconia: from single splat to coating formation," *Journal of thermal spray technology,* vol. 17, pp. 623-630, 2008.

[130] A. McDonald, C. Moreau, and S. Chandra, "Use of thermal emission signals to characterize the impact of fully and partially molten plasma-sprayed zirconia particles on glass surfaces," *Surface and Coatings Technology,* vol. 204, pp. 2323-2330, 2010.

[131] K. Yang, M. Fukumoto, T. Yasui, and M. Yamada, "Study of substrate preheating on flattening behavior of thermal-sprayed copper particles," *Journal of thermal spray technology,* vol. 19, pp. 1195-1205, 2010.

[132] H. Zhang, X. Wang, L. Zheng, and X. Jiang, "Studies of splat morphology and rapid solidification during thermal spraying," *International Journal of heat and mass transfer,* vol. 44, pp. 4579-4592, 2001.

[133] C. M. Van Atta, *Vacuum Science and Engineering: Properties of Gases at Low Pressure, Vacuum Measurements, Design and Operating Features of Vacuum Pumps and Systems*: McGraw-Hill, 1965.

[134] P. Xu, S. Xu, Y. Gao, and P. Liu, "A multicomponent multiphase enthalpy-based lattice Boltzmann method for droplet solidification on cold surface with different wettability," *International Journal of Heat and Mass Transfer,* vol. 127, pp. 136-140, 2018.

[135] M. Shen, B. Q. Li, and Y. Bai, "Numerical modeling of YSZ droplet impact/spreading with solidification microstructure formation in plasma spraying," *International Journal of Heat and Mass Transfer,* vol. 150, p. 119267, 2020.

[136] W. Xiong and P. Cheng, "Numerical investigation of air entrapment in a molten droplet impacting and solidifying on a cold smooth substrate by 3D lattice Boltzmann method," *International Journal of Heat and Mass Transfer,* vol. 124, pp. 1262-1274, 2018.

[137] A. McDonald, M. Xue, S. Chandra, J. Mostaghimi, and C. Moreau, "Modeling fragmentation of plasma-sprayed particles impacting on a solid surface at room temperature," *Comptes Rendus Mecanique,* vol. 335, pp. 351-356, 2007.

[138] P. Gougeon and C. Moreau, "Simultaneous independent measurement of splat diameter and cooling time during impact on a substrate of plasma-sprayed molybdenum particles," *Journal of thermal spray technology,* vol. 10, pp. 76-82, 2001.

[139] M. R. Morad, M. Nasiri, and G. Amini, "Numerical Modeling of Instability and Breakup of Elliptical Liquid Jets," *AIAA Journal,* pp. 1-8, 2020.

[140] S. J. Perkins, "Protein volumes and hydration effects: the calculations of partial specific volumes, neutron scattering matchpoints and 280-nm absorption coefficients for proteins and glycoproteins from amino acid sequences," *European Journal of Biochemistry,* vol. 157, pp. 169-180, 1986.